University of Potsdam – Institute for Physics and Astronomy

The Wolf-Rayet stars of the carbon sequence in the Andromeda Galaxy

Masterthesis

For the acquirement of the scientific degree
Master of Science (M.Sc.)
in the discipline Astrophysics

handed in by
David Gruner
Student number: 325344

University of Potsdam

Potsdam, December 4, 2018

Supervisor & first referee: Prof. Dr. Wolf-Rainer Hamann
Second referee: Prof. Dr. Stefan Geier

»Space is big. Really big. You won't believe how hugely mindboggling big it really is.«

– Douglas Adams

Acknowledgments

This publication makes use of data products from the Two Micron All Sky Survey, which is a joint project of the University of Massachusetts and the Infrared Processing and Analysis Center/California Institute of Technology, funded by the National Aeronautics and Space Administration and the National Science Foundation.

Based on observations made with NASA/ESA Hubble Space Telescope, obtained from the Mikulsky Archive at Space Telescope Science Institute, operated by the Association of Universities for Research in Astronomy, Inc., under NASA contract NAS 5-26555.

This research has made use of the NASA/ IPAC Infrared Science Archive, which is operated by the Jet Propulsion Laboratory, California Institute of Technology, under contract with the National Aeronautics and Space Administration.

The project has made use of public databases hosted by SIMBAD, maintained by CDS, Strasbourg, France.

This research has made use of the VizieR catalogue access tool, CDS, Strasbourg, France. The original description of the VizieR service was published in A&AS 143, 23

Based on observations made with the NASA/ESA Hubble Space Telescope, and obtained from the Hubble Legacy Archive, which is a collaboration between the Space Telescope Science Institute (STScI/NASA), the Space Telescope European Coordinating Facility (ST-ECF/ESA) and the Canadian Astronomy Data Centre (CADC/NRC/CSA).

This paper uses data products produced by the OIR Telescope Data Center, supported by the Smithsonian Astrophysical Observatory.

The plots and graphics created for this work made use of the Python3 libraries *matplotlib* (v 2.1.1), and *astropy* (v 3.0.3). Calculations, interpolations and linear regressions were done with the Python3 libraries *numpy* (v 1.13.3), and *scipy* (v 0.19.1). Spectral plots used in this work were created with WRPlot.

Abstract

Context Wolf-Rayet stars are among the most outstanding examples for extreme stellar physics. With their strong stellar winds they shape galaxies, their nucleosynthesis produce the heavy elements all life is made of, and at the end of their life, they create another example for extreme physics: a neutron star or a black hole. In this thesis, we shed light on a subgroup of those exciting stars: the WR stars of the carbon sequence, also denoted as WC stars.

Motivation Little is understood of the evolution of those key objects in galaxies. The quantification of their mass-loss rate and the interplay and dependency with other stellar parameter is of great interest for the fields of stellar physics and evolution, galaxy evolution and gravitational wave astronomy.

Aims In this work, we perform a spectroscopic analysis on the sample of WC stars in the Andromeda Galaxy (M 31). The advantage of stars not located in our own Galaxy is that distance uncertainties can be widely eliminated. Furthermore, M 31 is a galaxy with similar metalicity to the Milky Way. This fact makes it ideal for a comparison to the Galactic sample of WC stars.

Methods The spectroscopic analysis is performed utilizing the Potsdam Wolf-Rayet model atmosphere code (PoWR). We calculate model atmospheres and synthetic spectra which are then compared to optical spectra and photometry of the M 31 WC stars. The model parameter are adjusted in order to obtain the best spectral fit.

Results Stellar parameter are derived for 23 stars whose spectra do not show a sign of contamination by other sources. A detailed analysis was carried out for each star accounting for temperature, mass-loss rate, luminosity, abundances, terminal velocity and clumping.

Conclusions We find that the spectral classification of WC stars into subtypes solely based on the standard line characteristics is not meaningful. We show that a combination of temperature and abundance effects is required for spectral classification. Furthermore, we find signs of fast rotation in the majority of stars analyzed here. The analyzed stars populate the same parameter regime that is also found for Galactic WC stars.

Contents

1 Preface

»We are all in the gutter, but some of us are looking at the stars.«

– Oscar Wilde

»A long time ago in a galaxy far, far away...« there were some stars, outstanding among their kin. Those stars are Wolf-Rayet (WR) stars. WR stars are the late evolutionary phase in the life of massive stars. With their peculiar spectra and enormous impact on their surroundings, those stars are of significant importance despite their low number. WR stars have stellar winds, orders of magnitudes stronger compared to solar like stars. Those winds deposit an enormous amount of mechanical energy in the surrounding interstellar gas, additionally to the high amount of ionizing photons emitted by those hot and luminous stars. Furthermore, the winds carry the processed material of the stars – enriched material – and drive the chemical evolution of galaxies. WR stars might end their life as a supernova that also provide strong mechanical feedback, the enrichment with *r*- and *s*-process elements, and can shut down or trigger star formation. All those facts underline the importance of those stars for the evolution of galaxies on intermediate scales. The understanding of WR stars, their evolution, and the quantification of the stellar feedback are of high interest.

The introductory sentence is not entirely true. Those stars do also exist in our own Milky Way (MW), and in other galaxies. Furthermore, they do exist right now too. But the stars we want to focus in this work on, are located in the Andromeda Galaxy (M 31). At a distances of almost 0.8 Mpc, M 31 is the most distant object in the night sky regularly visible to the naked eye. Also, WR stars do have a very short life time. It is estimated to be on the order of 10^5 yr, of which they spend about 10^4 yr in the WC phase. If one now considers the light travel time from M 31 to us ($\approx 2.4 \cdot 10^6$ yr), the stars we receive the light from are long gone there. So the introductory sentence is true for the selection of stars we focus on here.

In this work we are going to have a look on a sample of those stars. To be more precise, we take a subsample – the stars in the second phase of being a WR – the Wolf-Rayet stars of the carbon sequence, or for short: the WC stars. The stars in M 31 are interesting for us since we can determine stellar brightnesses without being biased by unknown or highly uncertain distances as all the stars have approximately the same distance to us.

Stars above a certain threshold in mass are assumed to undergo the WR phase as last part of their life, before they explode as a supernova or collapse directly into a black hole (BH). The mass threshold is vaguely known at best, as well the impact of the metalicity. Also if the stars are able to enter the WR stage on their own, or the interactions in a binary system are required is debated. This present work is meant to shed some light upon those problems, with providing stellar parameters for the sample stars. Those parameter will be compared to evolutionary models and investigated for correlations between stellar and wind parameter.

After a short introduction about what is known in the field of WR stars (Sect. 2), we examine the properties of M 31 and their impact for our work in Sect. 3. The observations are discussed next (Sect. 4), where we will have a look on all available observational data, to get a comprehensive picture of the stars. But there are issues with the data. At the distance of M 31, light contamination by nearby sources in the spectra is a large problem. We will investigate the data for traces of contamination and remove stars from our list that show such signatures (Sect. 5). The stellar spectra are compared to synthetic spectra calculated from model atmospheres. A basic introduction to the modeling process and the calculation of the spectra is given in Sect. 6. The analysis process of the spectra itself, and the challenges occurring are discussed in Sect. 7. The obtained stellar parameter are then summarized for the sample in Sect. 8, and the implications of the results are discussed in Sect. 9. After drawing final conclusions in Sect. 10, we show the sample star spectral fits and give additional remarks on the individual stars in Appendix B. The spectra of the suspect and multiple systems are shown in Appendix C.

2 Wolf-Rayet stars

»The wonder is, not that the field of stars is so vast, but that man has measured it.«

– Anatole France

There are hundreds of billions of stars in a galaxy and all of them contribute to its shape. But the contribution of some stars is significantly higher then others. Among those stars are Wolf-Rayet (WR) stars; discovered by Wolf & Rayet (1867) and eventually named after them. From the original three stars in the constellation of Cygnus, their number has risen ever since, counting now 657 Galactic WR stars of the various subtypes (Crowthers Galactic Wolf-Rayet Star Catalog[1]). The total number of them in the Milky Way is estimated to be 1000 – 6000. A very low number compared to the 10^{11} stars in the Milky Way, but we will see, WR stars are of significantly higher importance for their host galaxy as a million of common low mass stars.

WR stars stood out of the normal stellar spectra due to their strong emission lines. In fact, a WR spectrum does not only show emission lines, but it is dominated by them[2]. With the discovery of more such stars, a classification system was established according to the appearance and ratios of certain emission lines.

2.1 Phenomenology of WR stars

Following their discovery, WR stars are defined spectroscopically. If an optical spectrum of a star only shows a certain set of emission lines, this star is a WR star. In this section, we want to give an overview about the different subtypes and their spectral characteristics. Common to all WR stars are helium emission lines. Notable here are the lines of the Pickering series, which denotes the transitions to the state with principle quantum number 4 in singly ionized helium (He II). Due to this ionization, He II can be seen as hydrogen-like and the lines coincide with the Balmer series of hydrogen (transition to the state $n = 2$). Every second line of helium coincides with a hydrogen line (e.g. He II $6-4 \sim$ H I $3-2$). The wavelengths of those transitions do not match perfectly – the helium lines are always slightly bluer – due to the different mass of the atomic nucleus. Furthermore, there are the transitions to the third ionized state (n=3) and the most prominent line here denotes the reddest transition in this series, He II λ4686. WR spectra might also show lines of neutral helium (He I), but those are usually weaker then the He II lines. As last point to mention are carbon lines which are visible in all WR types but their line strength differs significantly among the various subtypes. Any other spectral appearances are more or less unique for the individual WR types.

2.1.1 WN – The nitrogen sequence

The WR stars of the nitrogen sequence, shortly noted as WN stars, are the most abundant kind of WR star. They are assumed to form the first evolutionary state a star encounters when reaching the WR phases. As the name suggests, those stars are characterized by strong nitrogen emission lines. The spectrum is dominated by helium, mostly in the first ionized state. The nitrogen lines originate from high ions like N III and N IV. Figure 1 shows an example spectrum for a WN star with the typical emission lines.

As for the *normal* spectral types (MK classes), there is a similar subtype classification for WR stars. For WN stars, those subtypes cover the range 2 – 11 and as for normal stars, the naming as *early* and *late* types has established, referred to as WNE and WNL. As the only type among the WR stars, WN stars might still show traces of hydrogen in their spectra, and if that's the case, it is indicated by adding an *h* to the spectral class. The very late types (WN 10 – 11) mark the transition to Luminous Blue Variables (LBV)[3] and there are also transition types to earlier evolutionary stages, such as OB stars, usually referred to as so-called *slash* (/) stars and are denoted like WN 6 / O3 I. The subtypes WN 2 – 9 are assigned according to the appearance and strength of lines from the various nitrogen ions, usually N II – V.

Stars of the WN subtype are the most abundant among the WR stars. From the 657 entries in Paul Crowthers *Galactic Wolf-Rayet Catalog* 381 (58%) are classified as WN or *slash* stars. In the Andromeda Galaxy (M31), there are 154 WR stars known and 92 (60%) are WN (Neugent et al. 2012).

2.1.2 WC – The carbon sequence

The WR stars of the carbon sequence (WC stars) are the main focus of this work. Again, the name refers to the spectral appearance of the star, but for a WC much more then for a WN. The dominating carbon

[1] http://pacrowther.staff.shef.ac.uk/WRcat/index.php

[2] This might change in low metalicity environments like the Small Magellanic Cloud

[3] And are not WR stars in the classical sense, i.e. they do not show a steady stellar wind and are hydrogen burning. Their strong wind lines originate in irregular eruptions.

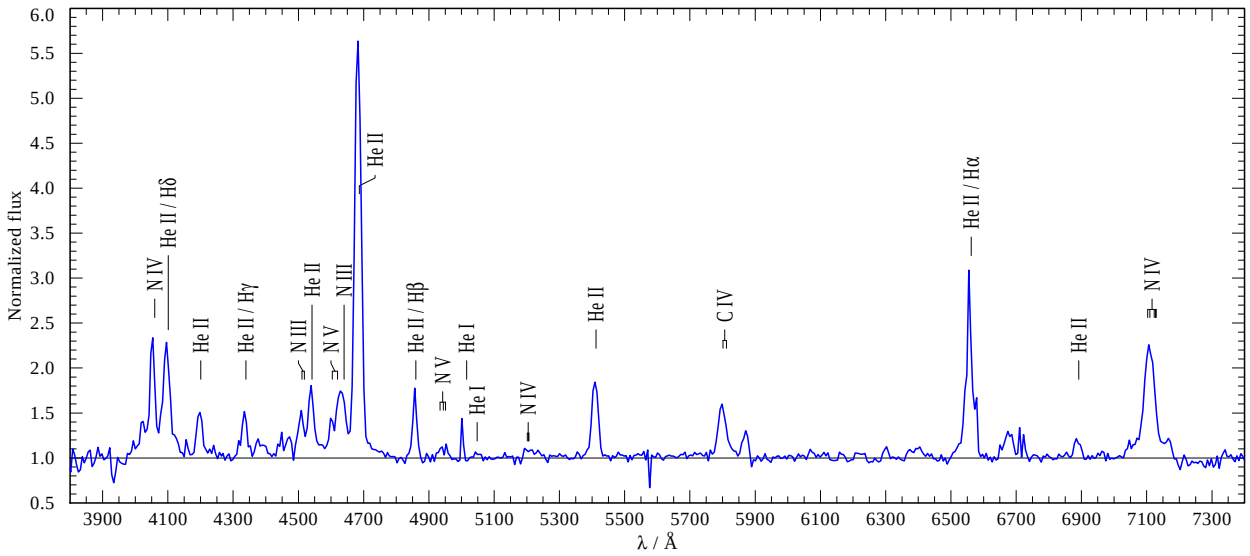

Figure 1: *Example for an optical spectrum for a WN6 star, here M31 WR 90*

lines C IV $\lambda\lambda 5802, 5810$; a blend of C III $\lambda\lambda 4647 - 4651$, He II $\lambda 4686$, and C IV $\lambda\lambda 4646 - 4665$, as well as C III $\lambda 5696$ characterize the spectrum of this subtype. The emission lines of a WC are much stronger than those in a WN. In Fig. 2, an example spectrum of a WC star is shown. Nitrogen lines are not visible in a WC spectrum.

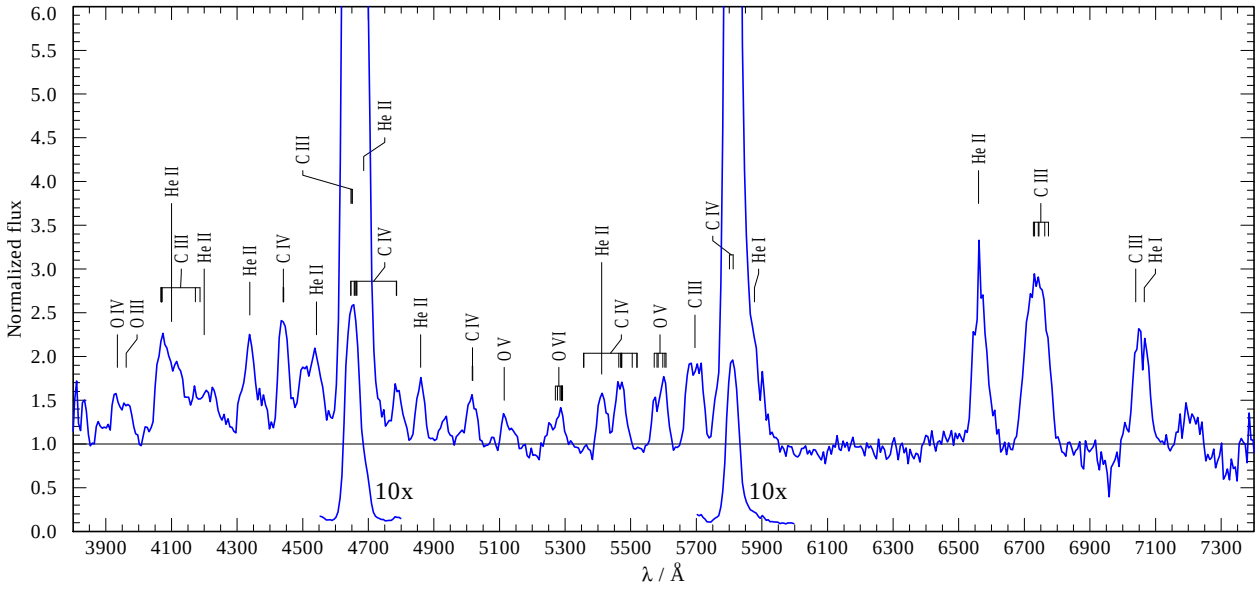

Figure 2: *Example for an optical spectrum for a WC6 star, here M31 WR 2*

Again we have a subtype classification system for WC stars. In difference to normal MK or WN stars, the scheme reaches from 4 – 9. This time, it's the prominent carbon lines determining the subtype. The classification criteria were introduced by Smith (1968) and extended to earlier types by van der Hucht (2001). The current list of criteria is given in Table 1. In some references, one also finds a separation into early and late WCs (WCL and WCE, respectively). Note that the criteria are partly very subtle, making it difficult to assign certain stars to a subtype. A classification covering two neighboring classes is not unusual, written as, e.g. WC 5 – 6. To include stars like this into our evaluation later on, we will treat them with the arithmetic mean, i.e. for the previous example as WC 5.5. A more quantitative scheme was presented by Crowther et al. (1998), who used the equivalent widths W_λ of the prominent lines as criteria, usually given in $\log W_\lambda$. An overview for the suggested criteria is given in Table 2.

WC stars are not as common as WN stars. The fraction WN/WC is of great interest especially in terms of stellar evolution. In Paul Crowthers catalog, 278 (42% of 657) of the listed stars are classified as WC. The M31 sample contains 62 WCs (40% of 154).

Table 1: *WC star classification system following Smith (1968) and van der Hucht (2001)*

Subtype	primary criteria	secondary criteria
WC 4	C IV strong, C III weak or nonexistent	intermediate O V
WC 5	C III $\ll$ C IV	C III $<$ O V
WC 6	C III $\ll$ C IV	C III $>$ O V
WC 7	C III $<$ C IV	C III $\gg$ O V
WC 8	C III $>$ C IV	no C II, no or weak O V
WC 9	C III $>$ C IV	existing C II, no or weak O V

Table 2: *WC star classification system following Crowther et al. (1998)*

Subtype	$\log W_\lambda \left(\frac{\text{C IV}\lambda5808}{\text{C III}\lambda5696}\right)$	$\log W_\lambda \left(\frac{\text{C III}\lambda5696}{\text{O V}\lambda5590}\right)$	$\log W_\lambda \left(\frac{\text{C IV}\lambda5808}{\text{C II}\lambda4267}\right)$
WC 4	$\geqslant$ 1.5	$\leqslant$ -0.4	
WC 5	1.1 – 1.5	-0.4 – 0.5	
WC 6	0.6 – 1.1	0.0 – 0.7	
WC 7	0.1 – 0.6	$\geqslant$ 0.1	
WC 8	-0.3 – 0.1		$\geqslant$ 1.0
WC 9	-0.7 – -0.3		-0.2 – 1.0

2.1.3 WO – The oxygen sequence

The WO type is the rarest among the WR stars. The Galactic catalog lists only 4, and in M31 not even one WO star is known. Those stars show strong oxygen lines, not as significant as the carbon lines in WC but more dominant as nitrogen in WN. Additionally to that, they also show very high oxygen ions, up to O VI. For WO stars, only the subtypes 1 –4 exist. The sub classification mainly bases on the ratio and appearance of oxygen lines and a few carbon lines. An example spectrum is displayed in Fig. 3.

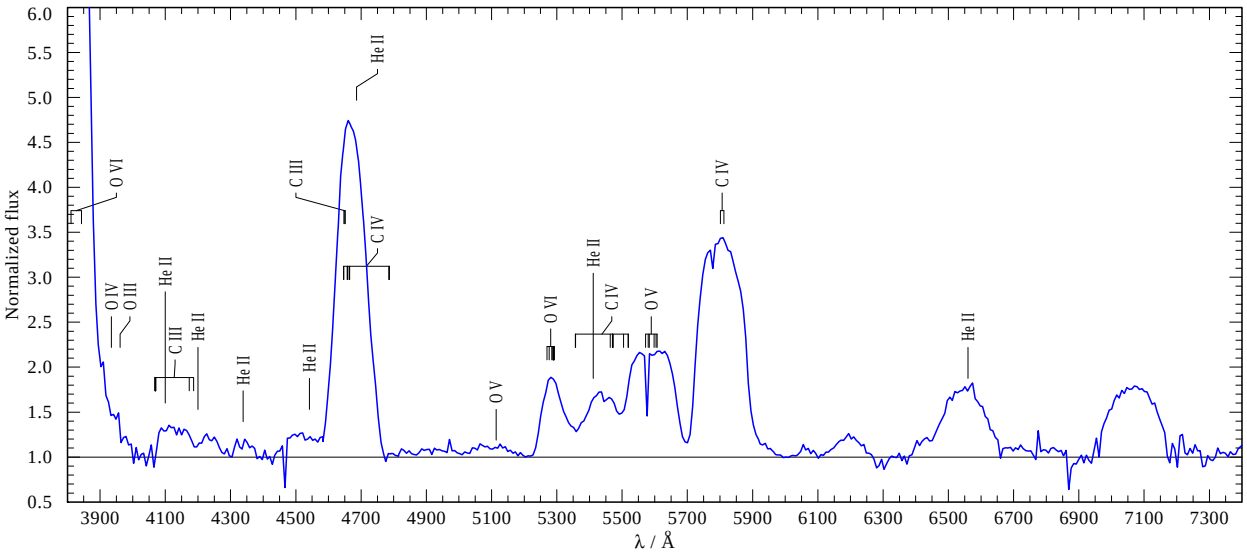

Figure 3: *Optical example spectrum for a WO2 star, here WR 142*

2.1.4 Between the chairs – the transition types

The three WR subtypes (WN, WC, and WO) are assumed to represent an evolutionary sequence. The duration of the transition from one subtype to another depends on the strength of mixing processes which transport the processed material to the surface. The basic idea is that the outer layers which caused the appearance as one spectral type are removed by the stellar wind and deeper layers with different composition become visible. The shallower the chemical gradient in the star is, i.e. the stronger the mixing, the longer a phase can be observed in which the stars shows signs of both subtypes. Those are the transition types. Their number will be small as the transition time can be assumed to be small compared to the lifetime of a subtype. But those stars are found. According to the spectral features they show, their classification will include both types. A WC star that still shows some nitrogen in its spectrum might be classified as

WC/WN, while WN/WC would denote a WN star with strong carbon lines. The existence of a WC/WO or a WO/WC subtype is speculative.

2.1.5 A similar appearance – Central Stars of Planetary Nebula

The classical WR stars, whose nature we will describe in the following section, are not the only stars that show an emission line spectrum like this. There are also the Central Stars of Planetary Nebula (CSPN). Those are hydrogen deficient stellar cores that drive a strong stellar wind and will become later on White Dwarfs (WD). The difference to a normal WR star is first of all its brightness, CSPNs are fainter by a factor of 10^2-10^3. CSPN's also show strong nebula emission lines like [O III]. Those stars, when identified accordingly are classified in the same way as WR stars, but in brackets to denote the different nature of the object, i.e. [WC4] or [WC8]. The existence of [WN] stars is debated. Note that it is generally impossible to separate a WC from [WC] without knowing the star's luminosity. For the present data, we can be sure that all stars are actual WC stars and no foreground CSPN. CSPNs are fainter by about two orders of magnitude compared to a WC. A foreground CSPN that appears at the observed luminosity of a M 31 WC star, the CSPN has to be at 1/10 of the distance, placing it at 77 kpc and therefore outside of any known structure in the Local Group.

2.2 WR stars as evolved massive stars

We introduced the spectral appearance of WR stars. Now we want to have a look on what they actually are and why they look as they do. A lot regarding WR stars is still unknown and highly debated. This is what is known:

- Wolf-Rayet stars are the late and final stages in the evolution of a massive star.

Massive stars develop significantly different to lower mass stars. Massive stars on the main sequence are hot and bright. Due to this brightness and the concomitant radiation pressure, the outer layers of the star are not bound to the star. There is an imbalance of the governing forces gravity, radiation pressure, and gas pressure. This matter outflow is called the stellar wind (Abbott 1977; Cassinelli 1979). All stars have a wind, even solar like stars, but the strength and underlying physics are widely different. For our sun, the wind is formed of particles from the hot solar corona. The particles' velocities are maxwellian distributed and the fastest of them exceed the escape velocity of the sun and form the solar wind. On that way the sun loses about $10^{-14}\,M_\odot$ per year. The wind of a massive star is much stronger. The mass loss rates $\dot{M}$ can reach up to $10^{-5}\,M_\odot$ per year. This means, a star can lose ten solar masses in a million years. This has a strong impact on the stellar evolution. The strength of this wind is caused by two facts:

1. Massive stars have a high luminosity, up to $10^5 - 10^6\,L_\odot$. Radiative pressure is caused by absorption of photons in the outer layers of the star. Those photons carry a momentum and this momentum is directed radially outwards. The absorbing atom takes this momentum and starts to move radially. The re-emission of the energy is isotropic. When observing an ensemble of atoms, no net momentum is caused by the emission. What is left is the directed absorption and therefore an acceleration outwards.

2. Since those stars are hot, the maximum of their radiation is in the far UV. This means, those stars emit much more UV radiation compared to a sun like star. The amount of momentum transferred from the stellar light to the outer layers is given by the following points:

   (a) The momentum carried by the photon. The higher the photon energy $E = h\nu$, the shorter its wavelength λ, the more momentum $p = m \cdot c = h/\lambda$ is carried.

   (b) The ability of the envelope to absorb the photons. The energy of the photons has to match the transitions in the atom. Also the amount of possible transitions is important. The more electrons and the more transitions are possible, the higher the number of photons that can be absorbed. Important here are the heavier elements, especially the iron group elements. Due to their high number of levels ($>10^5$) and transitions ($>10^7$), those are usually the main contributors for the acceleration of the wind. Other elements can become important too, like CNO and the noble gases. Due to their atomic structure, various iron group ions have transition in the UV. In fact when observing a massive star in the UV, a large part of the spectrum is dominated by iron lines, the so-called iron line forest.

   (c) An accelerated ion sees the light from the star red shifted. This means it can absorb bluer stellar light in the same transition that it accelerated it in the first place. This absorption causes a further acceleration that shifts the absorption wavelength even further to the blue. On that way, one atom can absorb multiple times in the same transition over large wavelength ranges.

Taking both points together, the high luminosity and the high temperature, both contribute to the strong stellar winds observed in hot and massive stars. At a certain point, the optical thickness of the wind reaches a point, where the hydrostatic part of the stellar atmosphere becomes invisible and only the wind can be seen in the spectrum. A WR star is *born*.

This scenario, where a massive star develops enough mass loss to reach the WR phase on its own is called the *Conti scenario* (Conti & De Loore 1979; Maeder 1996). A WR star develops from a very massive (O) star, passes through the Of phases, which denotes O stars with significant emission lines, and enters the WR state as WNL. As an O star, the hydrogen burning was done with the CNO cycle, which led to an enrichment in nitrogen and a depletion in carbon and oxygen. Therefore, the first stage of a WR star is the WN with strong nitrogen lines. At this point, the star has reached the helium burning[4] and the remaining hydrogen in the envelop is slowly removed by the wind. With all hydrogen gone, the star reached the WNE phase[5]. The helium burning is done with the triple alpha process, which leads to an enrichment with carbon. The processed nitrogen from the WN phases is removed by the stellar wind. With the carbon lines starting to dominate the spectrum, the star has reached the WC phase. A side branch of the triple alpha process creates oxygen which can result in the strong oxygen lines that are characteristic for a WO. Whether the WO and WC phase are successively reached by a star, or the WO phase is just an extension of the WC class to hotter temperatures, and if there is an evolution from WCL to WCE, is still unclear. Also the masses – initial as well as current – required to enter the individual stages are debated. Furthermore, it is also unclear if the stars become a Luminous Blue Variable (LBV) before entering the WR phase. The Conti scenario can be summarized as

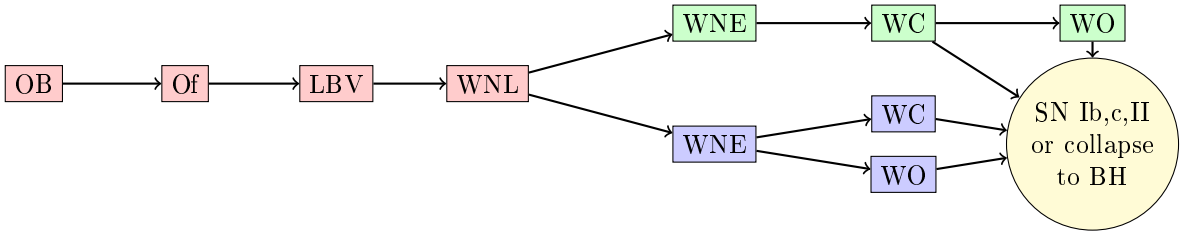

A crucial parameter for this evolution is the mass loss rate $\dot{M}$ whose estimation still suffers from large uncertainties.

Stars that are less massive might pass the red supergiant (RSG) phase. The mass loss on the main sequence is too low to lose the envelop but if the star reaches the red supergiant phase, this changes. An OB star would develop from the main sequence into a blue super giant (BSG) and then into a RSG. At this point the helium burning ignites, the mass loss increases, and the star goes back to higher temperatures and eventually enters the WR phase. The evolution from there on is similar to the Conti scenario:

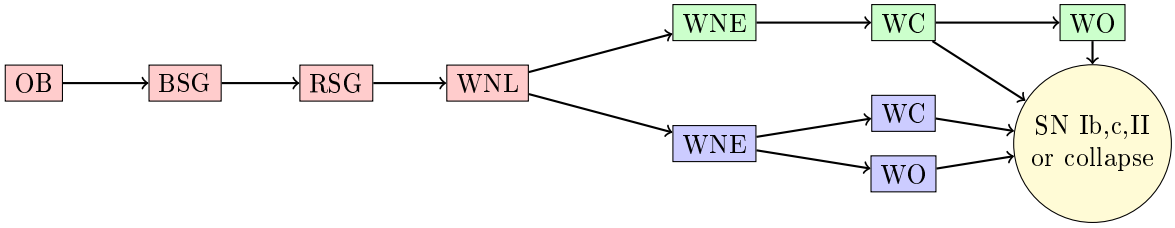

Before the Conti scenario was established, it was believed that all WRs have developed as a binary system (Paczyński 1966). In this scenario, a binary star composed of two massive stars enables Roche Lobe overflow between the stars. The more massive star develops first into a giant star and loses mass towards its companion. It will then appear as WR star. The star then might eventually collapse into a compact object, a black hole (BH) or neutron star (NS), and the rejuvenated companion star might become a WR star itself, either by following the Conti scenario or again by Roche Lobe overflow. If the system stays bound, a High Mass X-ray Binary (HMXB) has formed. It provides the progenitor for other interesting objects like the merger that produce gravitational wave (GW) events. If the system is not bound anymore the secondary star might be observed as a high velocity star (HVS) (Brown 2015). This processes can be summarized as

[4] Note that the most massive stars might still burn hydrogen at this point
[5] Note that there are also WNE stars with hydrogen and WNL without

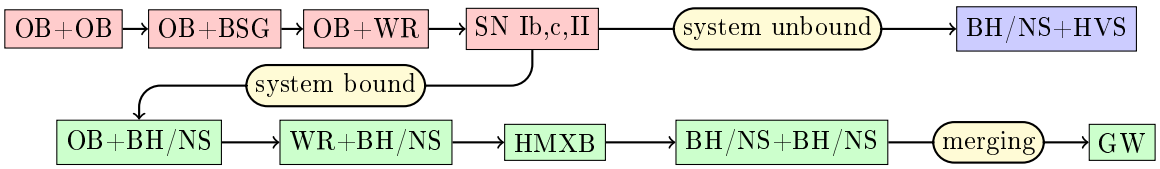

As one can see, a lot of unsolved riddles overcast the field of massive star evolution. And the field of binary evolution is just developing. The analysis presented in this thesis can provide constraints to the theoretical background of stellar evolution. The derived stellar parameters will give inside into the evolutionary state of the individual star. Especially a quantitative study of the mass loss in comparison to the other stellar parameter is of interest.

2.3 Shaping galaxies – the feedback of a WR star

Introducing them, we mentioned the strong influence of WR stars on the development of their host galaxy. In fact there are three contributions of a WR star, that make those stars interesting not only for stellar physicists:

Mechanical feedback: The stellar wind is first of all a matter outflow from the star into the inter stellar medium (ISM). Mass and velocity of the wind define the kinetic energy the stars *blow* into their environment. And this energy is significant. Early O stars as well as WR stars can blow bubbles (e.g. Arthur 2007; Ramachandran et al. 2018) into the ISM. A nice example is the bubble blown by WR 6, a WN4 star (see Fig. 4).

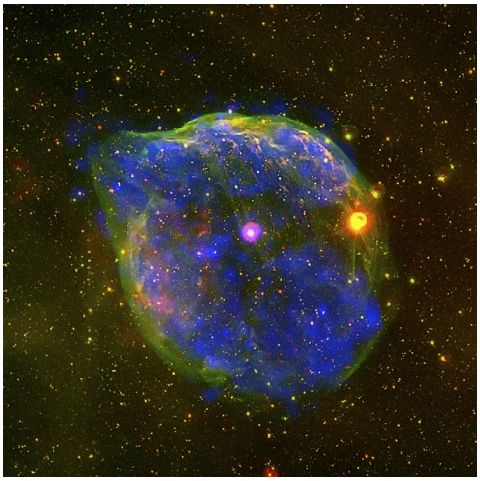

Figure 4: *The wind blown bubble around WR 6. Shown is a composition of X-ray emission (blue) and infrared emission (green and red). The WR star is the central pinkish dot. Such bubbles can reach sizes of several parsecs. Credit: ESA, J. Toala & M. Guerrero*

This enormous feedback can shape the local structure of a galaxy, influencing its star formation and gas motions. Especially if there is a cluster of WR and OB stars, their bubbles might merge into a super bubble (Castor et al. 1975a). Below, we will give the mechanical feedback $L_{\rm mech}$ of a star as kinetic energy per year blown into the surrounding ISM:

$$L_{\rm mech} = \frac{1}{2}\dot{M}v_\infty^2 \tag{1}$$

with $\dot{M}$ denoting the mass loss rate, usually given in $M_\odot$/yr, and v_∞ being the terminal wind velocity. It can be shown that the accumulated feedback of massive star winds can even top the feedback from supernovae (Fierlinger et al. 2016).

Ionizing radiation: WR stars are hot and luminous, but only a small fraction of the energy is used to power the stellar wind. In fact, the majority of the radiation can escape the star. This radiation is highly energetic and capable of ionizing hydrogen, helium, and heavier elements. This creates H II or even He III regions around such a star (Spitzer 1978). Below, we will describe the ionizing flux from a star with the number of photons Q emitted by the star per second bluer then the wavelength of the ionization edge

$$Q = n_{\rm photons}/{\rm s}. \tag{2}$$

H II regions can then be used as a tracer for star formation in remote galaxies (Peters et al. 2010) and to investigate the cosmic star formation history (Madau & Dickinson 2014).

Chemical enrichment: The stellar wind consist of the material from the outer layers of a star. For WR stars, this means the already processed elements that are mixed in the outer layers are ejected into the ISM by the stellar wind. As we have seen already, this outflow mostly consists of hydrogen at the beginning when the star is still an OB star. But for a WR star, the wind consists mostly of helium, CNO, and even heavier elements (Maeder 1992; Nomoto et al. 2013). When the WR star at the end of its life does not collapse directly into a BH, but explodes as a SN, even heavier elements then iron will be created and mixed into the ISM. Figure 5 gives an overview over the nucleosynthesis that created the elements we know. Note that most of the processed material inside the star is generally not mixed into the ISM. For a high mass star those elements are destroyed in the collapse before a supernova (photodesintegration and neutronization) and trapped inside the NS or BH. The chemical enrichment provided by the star is not easy to quantify, but in principle one can say as we only see the stellar wind, and thus the matter outflow, the chemical abundances derived from the wind gives the enrichment. Theoretically one can just take the mass fraction of the individual elements n_{element} together with the mass loss rate $\dot{M}_{\odot}$ and calculate the current amount of this element M_{element} mixed into the ISM, like for carbon

$$\dot{M}_{\text{C}} = X_{\text{C}} \cdot \dot{M}_{\odot}. \tag{3}$$

The abundances and the mass loss rate change over time.

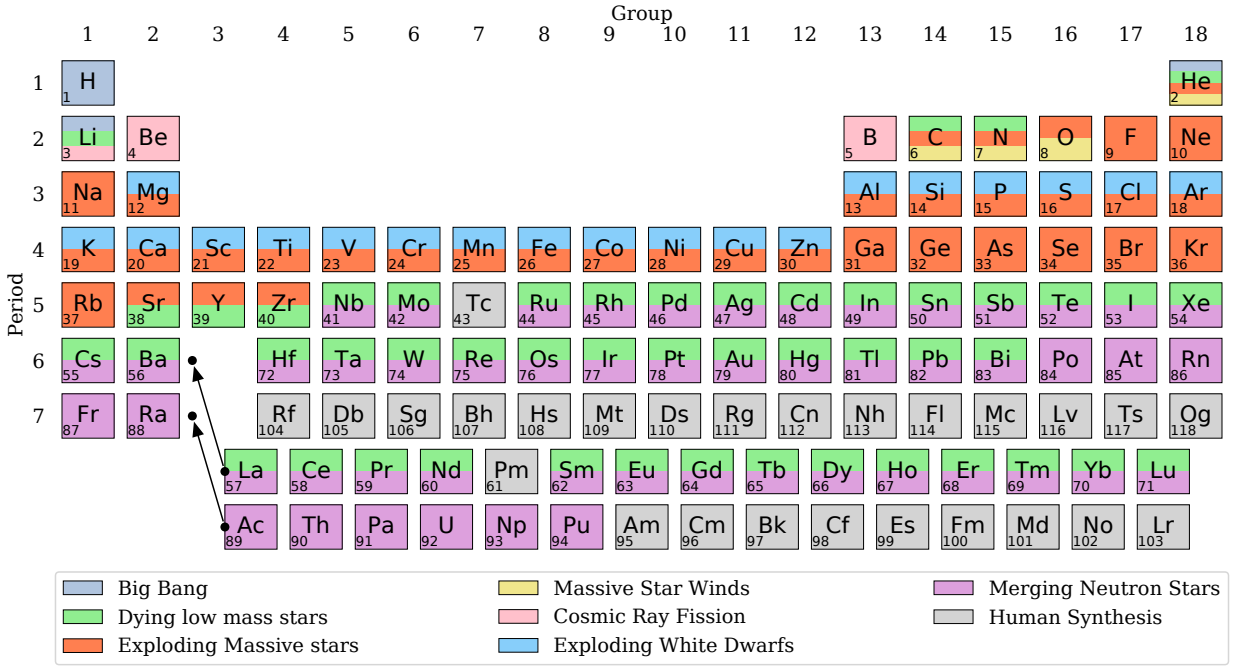

Figure 5: *Periodic table with an overview which processes created which elements. Note that the colored fraction of the fields for the individual elements does not represents the contribution of this process. Assumed values are highly speculative and therefore are not accounted for here. The contribution of massive stars is mainly by winds, SN (r- and s-processes) and eventually as NS mergers (Cowperthwaite et al. 2017).*

Understanding those three feedback mechanisms quantitatively not only provides constraints on massive star evolution, but also gives insights to galaxy evolution and star formation (Krumholz & Matzner 2009).

2.4 Studying WC stars

WR stars are known now for about 150 yr, but the knowledge of their real nature is fairly young (Underhill 1973). After the first discovery, various follow up observations revealed similar stars (e.g., Pickering 1881; Copeland 1884). While the concept that WR objects are in fact stars was accepted early, the origin of the emission stayed rather unclear. Also the separation of the WR population into WC and WN was seen early. Beals (1940) and others brought WR stars into context with other early type stars and attributed the strong and broad emission lines to atoms ejected at high velocity from the star. Zanstra (1931) argued for the emission line to be a result of recombination after ionization. Suggested for nebula emission, this can also be adopted for WR stars. For some time, it was referred to as the Wolf-Rayet Phenomena (Gebbie & Thomas 1968). As mentioned above, a WR stars is identified spectroscopically, and Gebbie & Thomas (1968) summed up the criteria that have to be fulfilled as:

1. *The spectrum consists of emission lines on a continuous spectrum which has an energy distribution rather like that of an O or B star.*

2. *A few absorption lines may occur as shortward displaced satellites on the edges of some of the emission lines. There is no general absorption line spectrum as known for normal spectral types. If such a spectrum is seen, it is attributed to a companion star.*

3. *The emission lines seen in any one object represent a wide range of excitation and ionization, excitation of the line spectrum generally being much higher then*[sic] *estimated from the shape of the continuous spectrum.*

4. *Most of the emission lines are broad with widths corresponding to hundreds to thousands of* $km\,s^{-1}$. *The widths are not the same for all lines in any one stellar spectrum.*

5. *Most of the spectra fall into two groups: (1) the WC stars in which the lines from C and O dominate, and (2) the WN stars in which the lines from ions of N dominate. Both groups show strong lines of* He II.

Not much has changed in our picture of WR stars since those words were written.

The detailed studies of WR stars turned out be difficult. The same strategy with calculating a stellar atmosphere model and from that a synthetic spectrum is the used method, but the models itself have to look different compared to stars without a strong stellar wind. For those, static and plane parallel atmosphere models were used which are not appropriate for WR stars. Hillier (1990) summarized the requirements for a stellar atmosphere calculated for WR stars, OB stars and LBVs as follows

1. *Solution of the statistical equilibrium equations (i.e., non-LTE)*

2. *Solution of the energy balance equation (radiative equilibrium if mechanical heating is absent)*

3. *Line blanketing*

4. *Coupling the wind dynamics with the radiation field.*

Fundamental efforts to realize the calculations were done by Scharmer (1981, 1984) based on work by Rybicki (1972), Mihalas et al. (1975), and Mihalas et al. (1976). Further development by Hamann (1985, 1986) brought the first success to the studies of WR atmospheres. Other work in this regard, developing different methods of solving the coupled equations, was done by, e.g. Olson et al. (1986), Olson & Kunasz (1987), and Puls & Herrero (1988).

The first calculations were mostly pure helium stars, to reproduce the emission lines (Hamann & Schmutz 1987) and the first systematic analysis were carried out by Schmutz et al. (1989). For WC stars, it became obvious that carbon needs to be included in the models as well. Due to the high abundance in a WC, carbon is required not only to reproduce the spectral lines, but also the spectral energy distribution (Hillier 1989). The inclusion of other elements, mainly hydrogen (Hamann et al. 1991) and nitrogen (Hillier 1988; Hamann et al. 1994) led to detailed analyses of the chemical composition of WR stars. Also attempts for hydrodynamically consistent models were made (Gräfener & Hamann 2005; Sander et al. 2017).

Extensive studies for Galactic WC stars were carried out by Hillier (1989), followed by Koesterke & Hamann (1995), Barniske et al. (2006), and Sander et al. (2012). Also low-metalicity environments were included in the studies, e.g. Grafener et al. (1998) for LMC WCs. the present study is an extension to all of this work, studying WC stars in M31.

3 The Andromeda Galaxy

»The distances in the universe are not only huge, they are grotesque.«

– Jostein Gaarder

The WR stars which we will speak about in this work do all belong to the Andromeda Galaxy. The Andromeda Galaxy, Messier 31 (M31), is the Milky Way's (MW) slightly larger sister. Both galaxies are spiral galaxies and the dominating structures in the Local Group. In this section, we want to discuss the important points about M31 for this particular work here.

3.1 Milky Way's sister

M 31 is a spiral galaxy just like the MW. It is assumed to be slightly more massive then our home galaxy (Partridge et al. 2013). We see M 31 close to edge on, and on a visual image there are no spiral arms visible. However, some structures are visible, given by regions dominated by dust or H II regions. If we look into the infrared, to identify the large gas structure, much more is visible (see Fig. 6). Next to the central region of the galaxy, an outer ring appears prominently. This so-called *ring of fire* (RF) is a region of increased density and star formation (van den Bergh 1964; Morrison et al. 2008). Block et al. (2006) suggested that this ring is caused by a collision and M 31 currently undergoing a transition to a Cartwheel galaxy. A major fraction of the identified WR stars in M31 are located along this ring. To the north-eastern and south-western part, the ring display substructures. This is probably caused by interactions of M31 with other galaxies, as we can also see a certain warped shape of the disk (Guhathakurta et al. 2000). Galaxies that might caused this distortion are M 32 or M 110, small companions of M 31.

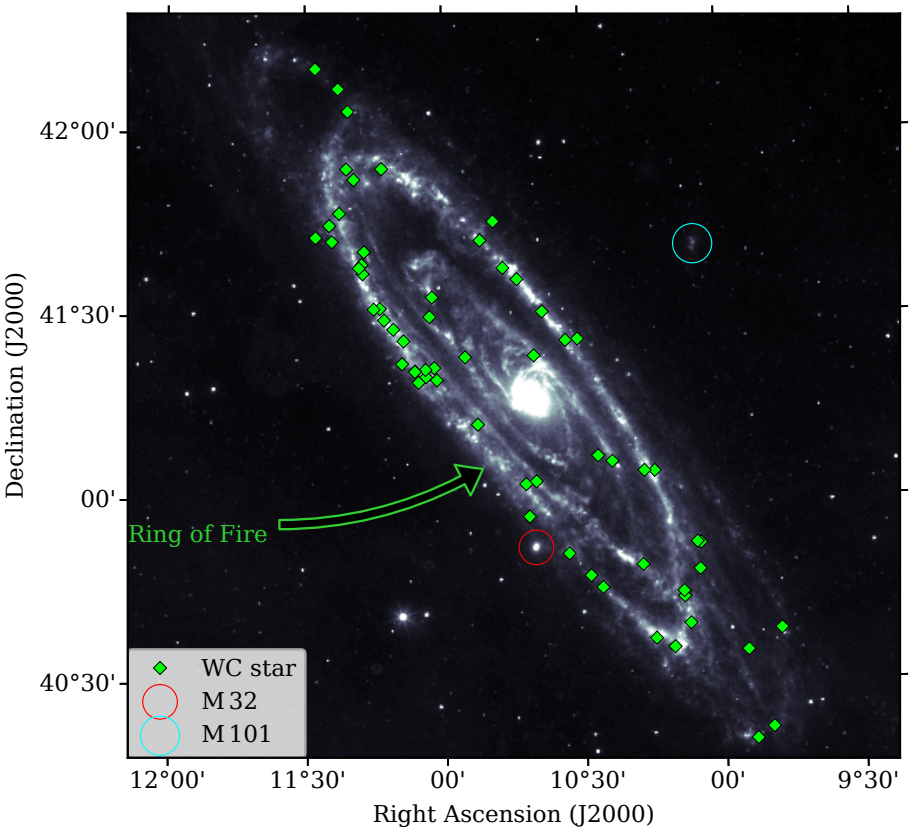

Figure 6: *Infrared image of M 31, the green symbols indicate the WC stars known in M31, the red and blue circles indicated M 32 and M 110, the two largest companions of M31, respectively. Background image: WISE All Sky survey (W3) mosaic*

An important fact for this work is that the metalicity of M 31 is comparable to the MW (McConnachie et al. 2005). For the inner region, the metalicity super solar, while for the outer region solar abundances are found. A more detailed look on the metalicity reveals a decrease of the metalicity outwards (Zaritsky et al. 1994) with the most recent result for a slope of $-0.017 \pm 0.02\,\mathrm{dex/kpc^{-1}}$ (Sanders et al. 2012). The gradient is disputable, as the data is not so clear (see figures 2, 8, and 9 of Sanders et al. 2012).

3.2 The distance to the stars in M31

The big advantage of analyzing stars in M 31 is their known distance. Therefore, the geometrical dilution of the light due to the distance is known, and we can determine the absolute magnitude of the individual stars. If the extension of the galaxy itself is negligible compared to its distance, we can assume the same distance for all stars, which is equal to the distance to the galaxy. For M 31, various measurements were made, as it is the closest spiral galaxy and therefore a first benchmark for distance measurements relying on individual stars. This is mostly done with the period luminosity relation derived for Cepheids, but also the Tip of the Red Giant Branch (TRGB), Red clump stars (RC), planetary nebula (PN), globular cluster (GC), and blue super giants (BSG) were used. Furthermore, other methods that are usually for more distant galaxies are extrapolated backwards, like the Tully-Fischer relation (TFR) and Surface Brightness fluctuations (SBF). Table 3 gives an overview for the most recent distance determinations and the used methods.

Table 3: *Distance measurements for M 31. The methods are: period-luminosity relation of variable stars (Cepheids), Tip of the Red Giant Branch (TRGB), Tully-Fischer relation (TFR), Surface Brightness Fluctuations (SBF), and cosmological redshift. Note that where no error is given here, no error estimate is given in the reference*

Distance [kpc]	Method(s) used	Reference
731^{+30}_{-30}	Cepheids	Wagner-Kaiser et al. (2015)
797^{+29}_{-29}	Cepheids	Wagner-Kaiser et al. (2015)
770^{+60}_{-60}	Cepheids, TFR, TRGB, SBF	Tully et al. (2013)
752^{+27}_{-27}	Cepheids	Riess et al. (2012)
779^{+19}_{-18}	TRGB	Conn et al. (2012)
700	redshift	Cappellari et al. (2011)
780	Cepheids	Tully et al. (2008)
800^{+100}_{-100}	TFR	Tully et al. (2008)
780	Cepheids, TFR, TRGB, SBF	Gil de Paz et al. (2007)

New observation indicate that maser emission from M 31 might also work for future distance estimations (Riess et al. 2016). From the mentioned results, we adopt $s_{\mathrm{And}} = 770\,\mathrm{kpc}$ from Tully et al. (2013) which appears to be the most reliable source, as various methods were used to confirm the distance. Furthermore, $s_{\mathrm{And}} = 770\,\mathrm{kpc}$ is covered by almost all error margins given and close to the mean value of the derived results of 763 kpc. A distance of 770 kpc corresponds to a distance modulus of

$$\mu = 5\log_{10}\left(\frac{s_{\mathrm{And}}}{[1\mathrm{pc}]}\right) - 5 = 24.4\,\mathrm{mag}. \tag{4}$$

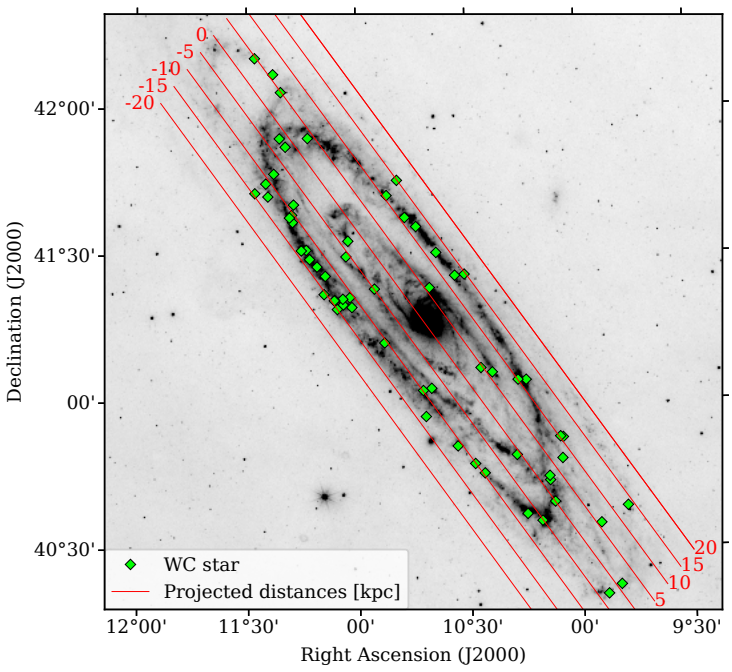

Figure 7: *Infrared map of M 31, the blue circles indicate the WC stars known in M 31. The red lines indicate lines of equal distance from the central axis with the according distance labeled (Numbers in kpc). The distances labeled assume a central distance of M 31 $s_{\mathrm{And}} = 770\,\mathrm{kpc}$ and inclination of $i_{\mathrm{And}} = 77°$. Background image: WISE All Sky survey (W3) mosaic*

The projected size of Andromeda on the sky is $186.2' \times 61.7'$, which makes it one the largest objects on the sky. At the distance of $s_{\mathrm{And}} = 770\,\mathrm{kpc}$, this extend corresponds to disk diameter of $d_{\mathrm{And}} = 45.7\,\mathrm{kpc}$. The inclination i_{And} is estimated to be between 75° and 78°, most likely at $i_{\mathrm{And}} = 77°$ (Schmidt 1957; Tully & Fisher 1988; Kent 1989; Tremaine 1995), meaning that we see M 31 almost edge on. If we assume a perfectly circular disk, this means the projected depth of M31 is

$$l_{\mathrm{And}} = d_{\mathrm{And}} \cos i_{\mathrm{And}} = 44.5\,\mathrm{kpc}$$

with the extend along the line of sight of M 31 d_{And}. If we want to compare the stars to each other a projection effect might be relevant. To evaluate, the projected distances in M 31 are displayed in Fig. 7.

The largest distance deviations for the sample stars is $\pm 15\,\mathrm{kpc}$. At a total distance of 770 kpc, this gives a relative error of 2 %. For the luminosity this is an error margin that is negligible, since the error in luminosity is dominated by other effects, such as the uncertainty of s_{And}, photometric uncertainties and the fitting process. Figure 7 also shows that M 31 is not circular as the projected depth d_{And} is about 30 kpc.

3.3 The motion of M31

M 31 is moving with its own system velocity. At a distance of 770 kpc, the tangential component of that motion is hard to measure. With high precision HST imaging, Courteau & van den Bergh (1999) was able to determine the transversal system velocity of M31 to be $17\,\mathrm{km\,s^{-1}}$.

Depending on the strength of the radial component of the velocity, we will see a Doppler shift in the spectral lines additionally to the intrinsic motion of the individual stars in M 31. Andromeda is approaching us. A system velocity of $-300\,\mathrm{km\,s^{-1}}$can be measured with respect to the solar system. Even for the broad lines of a WC, this motion is visible. The major contribution of this velocity does not come from the relative motion of M 31, but it is the solar system's orbital motion in the MW. A detailed study of Local Group galaxies found the relative velocity of M 31 and the MW to be -114 $\mathrm{km\,s^{-1}}$(Loeb & Narayan 2008). Those velocities indicate a future collision of the MW and M 31, but this is debated.

The radial velocity causes a Doppler shift of $\Delta\lambda = \frac{300\,\mathrm{km\,s^{-1}}}{c}\lambda = \lambda \cdot 10^{-3}$. All radial velocities given later in this work for the individual stars refer to the intrinsic velocity in the system of M 31 which is observable as additional proper shift.

4 Observations

»Nothing has such power to broaden the mind as the ability to investigate systematically and truly all that comes under thy observation in life.«

– Marcus Aurelius

To achieve the most coherent picture of the WC stars in M 31, we gather all available data, spectroscopic and photometric. The tricky part by using observations of stars in a different galaxy is to avoid or minimize light contamination by neighboring sources. At the distance of M 31, a moderate seeing of 1″ corresponds to 3.7 pc, and typical open cluster densities give much lower mean separations between the stars (Portegies Zwart et al. 2010). We will see below, how many stars of our sample actually suffer from spectral contamination. But first of all, one needs to find and identify the WC stars in M 31.

4.1 Finding WC stars in M 31

How to find WR stars? The significant features of a WR star are its strong emission lines. Therefore, those stars are easy to find. They can be found the same way planetary nebula are found in other galaxies: on a photometric way. For planetary nebula, the narrow [O III] and [S II] emission lines are searched for. For WC stars the emission line blend of C III $\lambda\lambda 4647-4651$, He II $\lambda 4686$, and C IV $\lambda\lambda 4646-4665$ is used. Meyssonnier et al. (1993) surveyed M 31 with an objective-prism and identified more than 1300 emission line objects.

A more sophisticated approach is to take on-off band imaging. One image is taken with a narrow band filter that only covers a spectral range where no emission lines are visible in the spectrum of a WR star, and one that is centered on a prominent emission line. While for planetary nebula those filter are very narrow, for WR stars they are broader. A subtraction of those images from each other reveals the location of a star/object of interest.

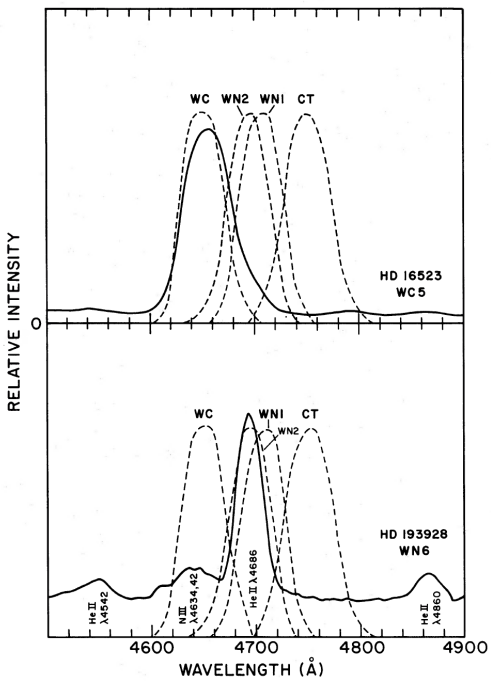

Figure 8: *Filter system to identify Wolf-Rayet stars using on-off imaging. The solid lines indicates a typical WR spectrum.*
Upper panel: *a WC star spectrum (solid black line) showing the blend of* C III $\lambda\lambda 4647-4651$, He II $\lambda 4686$, *and* C IV $\lambda\lambda 4646-4665$ *compared to the adopted filter curves for the imaging.*
Lower panel: *a WN star spectrum (solid black line) showing the emission line of* He II $\lambda 4686$ *compared to the same set of filters. The single filter curves (black dashed lines) are labeled according to the type of star which should be identified with it.* CT *denotes the continuum. Note that the WN filter will also identify the WC stars as both contain* He II $\lambda 4686$. *A comparison to the WC filter will reveal the difference. Figure taken from Armandroff & Massey (1985).*

Neugent et al. (2012) observed M 31 and M 33 with a filter system developed by Armandroff & Massey (1985). The filter curves and comparison spectra for WR stars are displayed in Fig. 8. Three filters, one that covers the range of a WC emission, one for a WN emission, and one to measure the continuum are used. According to the observed fluxes in these filters, the stars are either preliminary classified as WC, WN, or as other types of objects. Neugent et al. (2012) identified 216 WR star candidates. They removed 28 objects from their sample which show a much redder color ($B-V>0.6$) than a WR star would do. It turns out that late type stars might appear as WR star with this method as they show an absorption band in the continuum filter (Neugent & Massey 2011).

The final sample which was then scheduled for a spectroscopic follow-up observation contained 190 stars. 188 of those are the identified candidates from above. Massey & Johnson (1998) already found 48 WR stars

and confirmed their nature spectroscopically. 46 stars of those were also part of the Neugent & Massey (2011) sample and the remaining two stars were added.

4.2 Spectroscopic data

The spectroscopic observation were also carried out by Neugent et al. (2012) as a follow-up to the aforementioned photometric survey. From the 190 WR candidates, the spectra revealed 154 to be actual WR stars and 62 of them are of type WC.

The spectra were taken with *Hectospec*, a multi-object fiber-fed spectrograph at the Magnum Mirror Telescope (MMT) (Fabricant et al. 2005) and reduced with the standard reduction pipeline (Mink et al. 2007). The resulting spectral coverage from 3700–9150 Å was reached with a resolution of 6 Å. A problem of the used setup is that the red part of the spectrum (>7000 Å) is contaminated by second order blue light.

Neugent et al. (2012) classified the observed stars according to the criteria from Smith (1968) with the extension from van der Hucht (2001) (see Sect. 2.1.2). The optical spectra employed in the present work are taken from their survey, as well the spectral classification. If we investigate the spatial distribution of the stars of the individual spectral types, we would expect two different possibilities. (1) Either there is no structure in it. The stars are spread more or less randomly all across M 31 independently of spectral type. (2) Or we find a structure. Reasonable are two distributions. The stars are more or less allocated around the *ring of fire*, or we see a clear difference between inner and outer region due to the metalicity gradient found for M 31. A closer look, cf. Fig. 9, reveals that both expectations are not fulfilled entirely. The stars appear randomly distributed with a slight accumulation around the *ring*. We do not see any correlation between the individual distance to the *ring* and the spectral type, but we do see a gradient in spectral type across the entire galaxy. The earlier subtypes seem to accumulate in the southern half while the norther half is dominated by the later types.

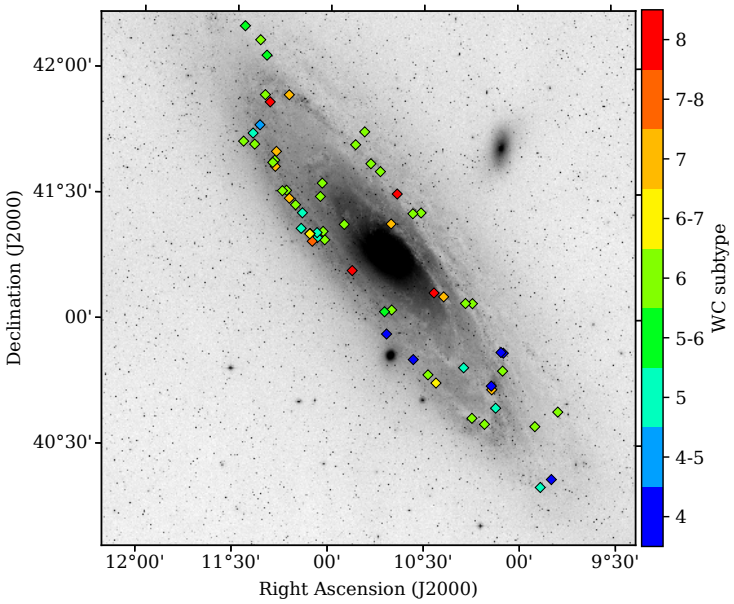

Figure 9: *Spatial distribution of the WC subtypes in M 31. Each dot represents a WC star found by Neugent et al. (2012), and the color coding gives the spectral type. Classification also by Neugent et al. (2012).*

We prefer to normalize the spectra before usage. For some of the spectra, Phil Massey already provided data in normalized form, others were normalized in an earlier effort to analyze the data. This gives a potpourri of spectra with normalization of different quality and without. To achieve the most reliable result, all normalizations were redone for the individual stars before plotting them against the normalized synthetic spectrum. The normalization is done with the help of a low order polynomial that is fitted to the continuum. See details in this regard in Sect. 7.2.2.

4.3 Photometry

The big advantage of using stars in M 31 is their known distance. But to make this usable, we need flux calibrated measurements. Massey et al. (2006) carried out photometry on our WC sample as part of the Local Group Galaxy Survey (LGGS), providing *UBVRI* magnitudes for more then 370 000 sources. All WC stars identified by Neugent et al. (2012) have a counterpart in this survey, with the exception of two stars (see for their treatment below). Therefore, all of them are already assigned with *LGGS* and an identifier

based on their celestial coordinates (J2000), e.g.

$$\text{LGGS J003911.04} + 403817.5 \text{ refers to a star at}$$
$$\alpha_{\text{J2000}} = 00^{\text{h}}39^{\text{m}}11\overset{\text{s}}{.}04,\ \delta_{\text{J2000}} = +40^{\circ}38'17\overset{''}{.}5.$$

To not address the stars always with this unhandy number[6], a different naming scheme has established for the stars. Like for the MW, the stars are denoted as M 31 WR #, where # is a running number based on the star's coordinate, with increasing right ascension.

All stars except of two are covered by the survey of Massey et al. (2006), but not for all of those a complete sample of *UBVRI* photometry exists. For some of the stars, the bluest or reddest bands are missing. Fortunately, the WC sample is widely complete in this regard, only for one star *I* is missing (see Table 14).

To determine the brightness of the star, we can use the optical photometry. But the optical range alone is not sufficient to determine the reddening precisely. To put more constraints on the reddening, we also investigate further sources for photometric measurements. As the WCs in question are extragalactic stars, the amount of surveys covering them are limited. The limiting factors are the brightness and the required spatial resolution. All ground based All Sky surveys (e.g. DSS, SDSS, or PANSTARRS) are therefore not sufficient to provide photometry. Also space mission surveys do not always fulfilled the requirements. WISE and Herschel covered all of M 31, but their spatial resolution is too low.

The best spatial resolution is of course given with Hubble Space Telescope (HST) imaging. Fortunately, almost 50% of M 31[7] is covered by extensive HST observation in various bands. However, the images taken are not always in the same bands. Most of them were taken as part of the HST legacy project *A Panchromatic Hubble Andromeda Treasury* (PHAT) (Dalcanton et al. 2012). Further coverage for the large OB associations in M 31 was carried out by Bianchi et al. (2012), and for a small part of the outer region by Williams et al. (2014). The two larger surveys provide catalogs with the extracted photometry in various HST filters. However, a cross correlation between our WC stars and those catalogs revealed few to no matches. Only a handful stars appear to have a counterpart but even for those the spatial offset is between 0.1″ and 0.7″. When we check the HST data to extract photometry manually from the Hubble Legacy Archive (HLA), it becomes clear where this problem has its origin. The pointing of the HST images is not as reliable as expected. Significant coordinate offsets can be found. Therefore, only a small fraction of stars in our sample seems to have a counterpart in the HST images. This also undermines the attempt to automatically extract the photometry from HLA data ourself as the real counterpart of the stars in question is uncertain. However, it is possible to extract photometry from the HST images. We will address this process below.

Another instrument providing good spatial resolution is Spitzer. A survey was carried out to obtain photometry of stars in local group galaxies (Khan 2017). A cross correlation reveals many more matches between our sample the catalog, about 50% of the stars are covered, but only if we assume an offset as 4.0″ as limitation. In fact, only one star has a separation between its coordinates and the closest Spitzer catalog entry below 1.0″.

All of this denies us the attempt of extending the available photometry to UV and IR from available catalogs.

4.4 Imaging

We mentioned already the extensive coverage of M 31 with HST imaging. Those image are obtained from the Mikulski Archive for Space Telescopes (MAST[8]). If available, those will allow us to do two things:

Investigation of the stellar neighborhood: The comparison of the image of the region around the stars in question to the fiber aperture of Hectospec will give indication if a spectrum is likely to be contaminated. Of course, at the distance of M 31, even HST cannot resolve close systems. But the impact of stars in the neighborhood, like stars of the same cluster, can be estimated. The images are available in different filters, depending on the individual star and the survey it was covered with. The contamination by neighboring stars is largest by other luminous stars, mostly supergiants. Cool stars do not emit much radiation in the blue and show absorption lines. Their impact will be obvious in the spectra and photometry. More problematic is the impact of OB stars. Their spectral energy distribution is comparable to those of WR stars and the absorption lines are weak. It is therefore much easier to *hide* an OB star in our spectra. The individual criteria on which we identify spectral contamination are

[6] Note that the two stars without counterpart are named with an X instead of a J

[7] The south-eastern half is not. Due to the way the WR stars are enumerated, stars with lower numbers are more likely to not be covered by an observation.

[8] mast.stsci.edu

discussed in Sect. 5. The images will show how isolated a star is located or if it may be in the middle of an open cluster. To identify early type stars that might contaminate the spectrum, we investigate preferably the images taken with UV or blue band filters.

Extraction of HST photometry: The Hubble Legacy Archive[9] (HLA) provides HST data in enhanced quality and with further processing. One of these processes is the extraction of photometric measurements from the HST images. There are two source lists: DAOPHOT (Stetson 1987), which is optimized for point-like objects, and SEXTRACTOR (Bertin & Arnouts 1996), which is optimized for extended objects. We will adopt the photometry directly from those catalogs. As we already mentioned, it is not always clear which object in the image is in fact the WR in question and there is, even in the HLA data, an astrometric offset between the images. Therefore, for each star the neighborhood would need an investigation by eye to decided which star most likely is the WR, and to extract the photometry for this very object from the available images. This is an extensive task and beyond the time frame for this work. Therefore, we limit this effort to a subset of stars, where the analysis indicates that the HST photometry might provide additional insights.

4.5 Investigation of the stellar neighborhood

Next to investigation of possible contamination by near-by sources (cf. Sect. 5), the stars might be part of larger associations and the cause for the above mentioned bubbles. A search for H II regions connected to the WR stars in M 31 was already carried out by Bransford et al. (1999). As the main focus of this work is on spectroscopic data, we will not investigate this further. Only for illustration purposes, some of the findings are shown here to support the mentioned importance for the small scale evolution of galaxies of massive stars in general and WR stars in particular. The right panel in Fig. 10 shows a gigantic open cluster with numerous bright stars. Most likely, WR 121 is also a part of this cluster, sitting in the outer regions. Interestingly, even as WR 121 is a comparably bright WR star, it is by far not the brightest blue star in this association. It can be seen in various images, that a the majority of WC stars analyzed here, are part of a larger association. But on the other hand, some of them appear to be widely isolated.

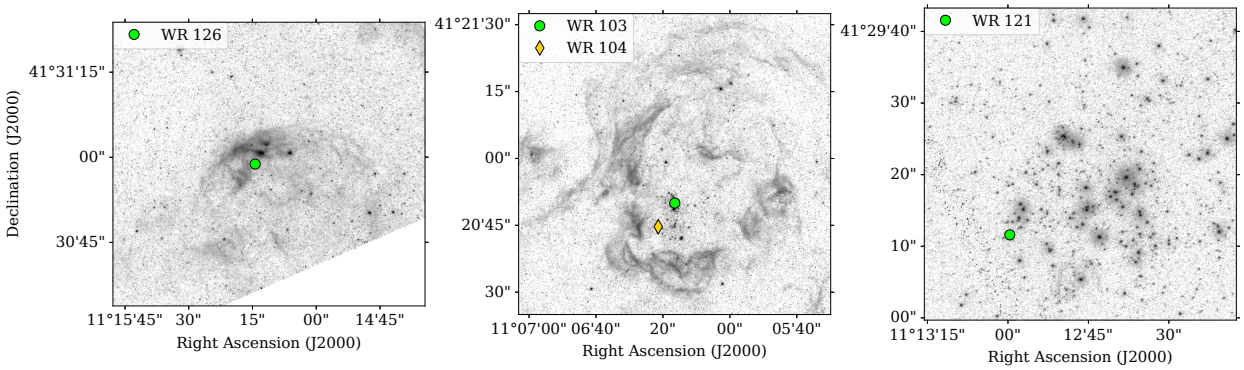

Figure 10: *Large structures around the sample stars in M 31. The locations of the stars are indicated.*
Left panel: *Region around WR 126 observed in Hα. The crescent shaped emission region is* H II *2886 (Azimlu et al. 2011) and appears in the form of a bow shock. Image ID: hst_14072_10_acs_wfc_f658n*
Middle panel: *Region around WR 103 and 104 observed in Hα. The large structure is identified as super bubble around the stellar association B-011 (Magnier et al. 1995). Unfortunately, There is no archived spectrum for WR 103 while spectrum of WR 104 highly contaminated as it is located in the center of the association. Image ID: hst_14072_07_acs_wfc_f658n*
Right panel: *Region around WR 121 observed with the cluster. Image ID: hst_12075_04_wfc3_uvis_total*

It gets more interesting if we have a look at images, taken with narrow-band filters. Filters like F656N, F657N, and F658N or F502N map nebula emissions. In those filters, we can identify large gaseous structures around the stars to find the above mentioned bubbles and H II regions. Figure 10 shows examples of those structures. The middle panel shows the OB association B-011 with its members WR 103 and 104 with the Hα emission regions indicate the size of wind blown super bubble. The left panel shows a crescent like structure in the vicinity of WR 126.

[9] hla.stsci.edu

5 The sample

»The good ones go into the pot, the bad ones go into your crop.«

– Cinderella

The data have to be inspected. The final goal of this work is a spectral analysis of the individual stars. This requires the spectrum of the WR star, not of a binary or multiple system. Multiple star analysis are possible but they need better and more extensive data as we have here. The first task is now to see, which of the spectra are not contaminated.

How do we decide if a star is single or multiple? At the distance of M 31 the probability is high that the area covered by the spectrographs aperture contains various stars. Therefore, we can assume that all spectra contain light from more than one source. The question is, how problematic is the influence? The advantage of WR stars is their brightness. Those stars outshine most other types of stars. Even a dozen of late type main sequence stars do not significantly impact the observed spectra, they are just too faint. This changes if we consider evolved stars, like red supergiants, and early type stars, like OB stars. Their luminosity is in the same order of magnitude and in the optical they can even be brighter than WR stars. But those stars can be easily identified in the spectrum. The spectral significance of a WR star are the strong emission lines. No other type of star shows something similar. For WC stars, those are mostly C IV and C III lines, which are unique. Early OB supergiants may also show emission lines, but they are not only weaker and much narrower. Furthermore, these lines are from H I or He II, or N II and N III. Next to the emission lines, those OB stars also exhibit absorption lines. If we can see those in one of our spectra, it is clearly contaminated. An example for the appearance of such a spectrum is given in Fig. 11, showing M 31 WR 35.

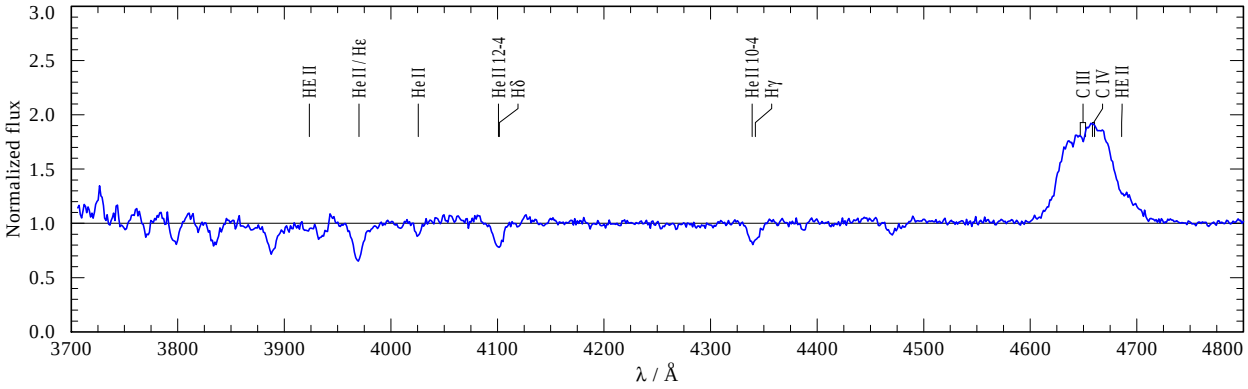

Figure 11: *Blue part of the normalized spectrum of WR 35. The absorption lines are due to contamination by an OB type star.*

Some of the available spectra show a low signal-to-noise ratio (S/N) and absorption lines might not be visible there. How can we still identify contaminated spectra? It becomes more obvious, if we compare WR 35's spectrum and one from an uncontaminated WC star of same spectral type (see Fig. 12 with WR 150). The difference is striking. In addition to the absence of any kind of absorption in WR 150, the strength of the emission lines is of a completely different magnitude. Especially the outstanding emission around 4650 Å shows this difference. The reason for this is simply the dilution of WR 35's spectrum by the continuum flux of the contaminating star(s). The emission lines in a normalized spectrum get weaker compared to the continuum by adding more continuum flux.

Now we have a second way to find out whether a spectrum is contaminated or not. However, two issues remain. We can not identify a blend of two WC stars that way. Also we need to determine at which point we consider a spectrum as contaminated. We decide for a rigorous policy in this regard, every star that appears only slightly suspicious to be multiple is taken out from the final sample. But, to not lose too many stars, we divide the stars into three sub categories: *single*, *multiple*, and *suspect*.

With this in mind, we go through the data and the first point we noticed is, that not all the stars identified as WC stars have an archived spectrum. Three (5%) of the 62 WRs are without a spectrum available in Vizier[10]. Neugent et al. (2012) mentioned that not all WR stars were covered in the spectroscopic follow up observations. Previously known stars was given a lower priority. As we intend to make out sample as extensive and complete as possible we investigate the missing three stars further. For M 31 WR 91 (LGGS J004406.39+411921.0) we find an archived spectrum in the Hectospec CFA archive[11] also taken by

[10] vizier.u-strasbg.fr/viz-bin/VizieRJ/, catalog ID: ApJ/759/11
[11] oirsa.cfa.harvard.edu/

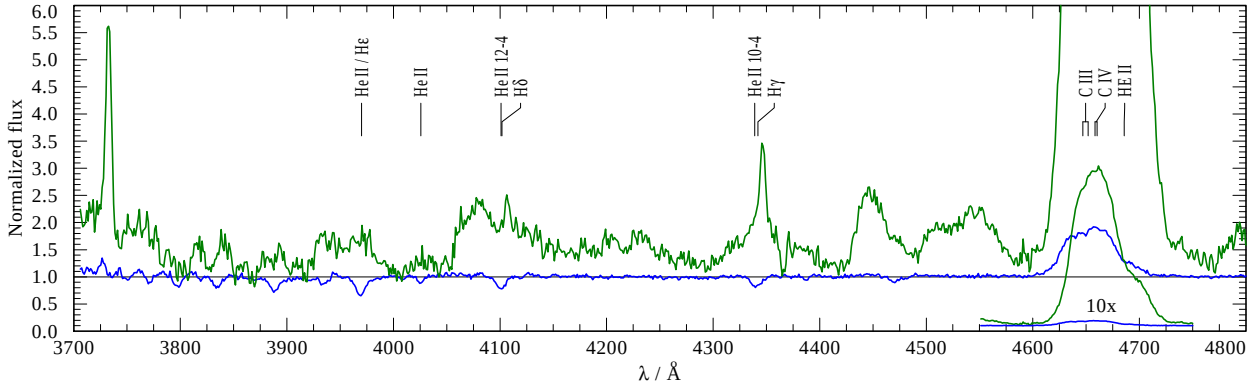

Figure 12: *Blue part of the spectrum of WR 35 (blue) and WR 150 (green); Both spectra are normalized*

Neugent et al. (2012). The stars was probably just missed when uploading the data to Vizier. As all spectral observations were reduced with the standard pipeline, we can take the spectrum from the archive and proceed like for all other spectra we have[12]. For the remaining two stars, no spectra could be found in the archives (Table 4).

Table 4: *M 31 WC star without an archived spectrum*

WR #	LGGS	Spectral type
104	J004425.43+412044.7	WC6-7
133	J004513.68+413742.5	WC+abs

The remaining sample of 60 stars is now investigated further to identify *multiples*[13]. This was repeated several times, reflecting the learning curve in evaluating the WC spectra by the humble author of these lines.

As expected for stars at the distance in M 31, a large fraction of spectra shows contamination by other sources. In total 24 (38%) spectra were identified as clearly contaminated and taken out. The excluded stars are listed in Table 5. This almost halves the original sample.

Table 5: *M 31 WC stars identified as contaminated spectrum; the classification of the contamination source if given was done by Neugent et al. (2012)*

WR #	LGGS	Spectral type	WR #	LGGS	Spectral type
3	J003919.53+402211.6	WC4	98	J004415.77+411952.5	WC5
22	J004034.17+404340.4	WC7+fgd	99	J004416.20+412103.5	WC+B0I?
29	J004058.49+410414.8	WC6	103	J004425.10+412050.0	WC6+B0I
30	J004059.13+403652.0	WC6	111	J004435.15+412545.2	WC5
35	J004109.59+404856.2	WC5+B	116	J004444.00+412739.9	WC6
47	J004144.47+404517.1	WC6-7	126	J004500.96+413058.8	WC6
52	J004203.94+412554.5	WC6	129	J004509.18+414021.4	WC7
61	J004247.12+405657.1	WC4	130	J004510.39+413646.6	WC7+BI
64	X004256.05+413543.7	WC6	136	J004517.89+415209.5	WC8
73	J004316.44+414512.4	WC6	140	J004530.61+414639.2	WC4-5
77	J004327.92+414207.3	WC6	143	J004537.10+414201.4	WC6
91	J004406.39+411921.0	WC6	146	J004539.35+414439.8	WC5

All of the stars already marked as binaries by Neugent et al. (2012) were identified as such by us too. No effort was taken to identify the source of the contamination. Only a minor fraction of stars shows actual absorption lines, and those were all already identified. But for most spectra, only the dilution could be used as binarity indicator. It is basically impossible to tell, what kind of star caused the dilution. However, some of the stars were assigned to known OB associations in M 31. Others are part of large H II regions.

[12] Note that for almost all WC stars in the Hectospec CFA archive more than one spectrum from the survey is available. The spectra were obtained in multiple runs, see Neugent et al. (2012). The spectrum adopted by us is the average of all spectra for the individual star after those were normalized.

[13] Whenever in this text we speak about binaries, multiples or contaminated spectra, there is always meant the same: The spectrum shows clear signs of contamination by a different source. Whether the system is an actual physically bound binary or multiple system or just stars located along the same line of sight does not matter here.

As an additional consistency check, we investigate HST images of the identified stars from above, if such images are available. We mentioned already a certain offset between the archived HST images and in turns that out the difference occur when comparing images from different cameras (ACS-WFC, WFPC2 & WFC3)[14]. But this astrometric error is not of significant importance for us now. The idea is to see if the region around the star is crowded by bright stars or the WR star sits isolated. In Fig. 13 we show images in two filters for two different stars each. M 31 WR 99 was identified as contaminated and M 31 WR 150 as single star. The difference is striking. Especially in the blue image, WR 150 outshines all objects around it. But for WR 99 it is obvious that multiple, at least equally bright sources contribute light to the obtained spectra. This method is limited in its results as we cannot identify close binary systems.

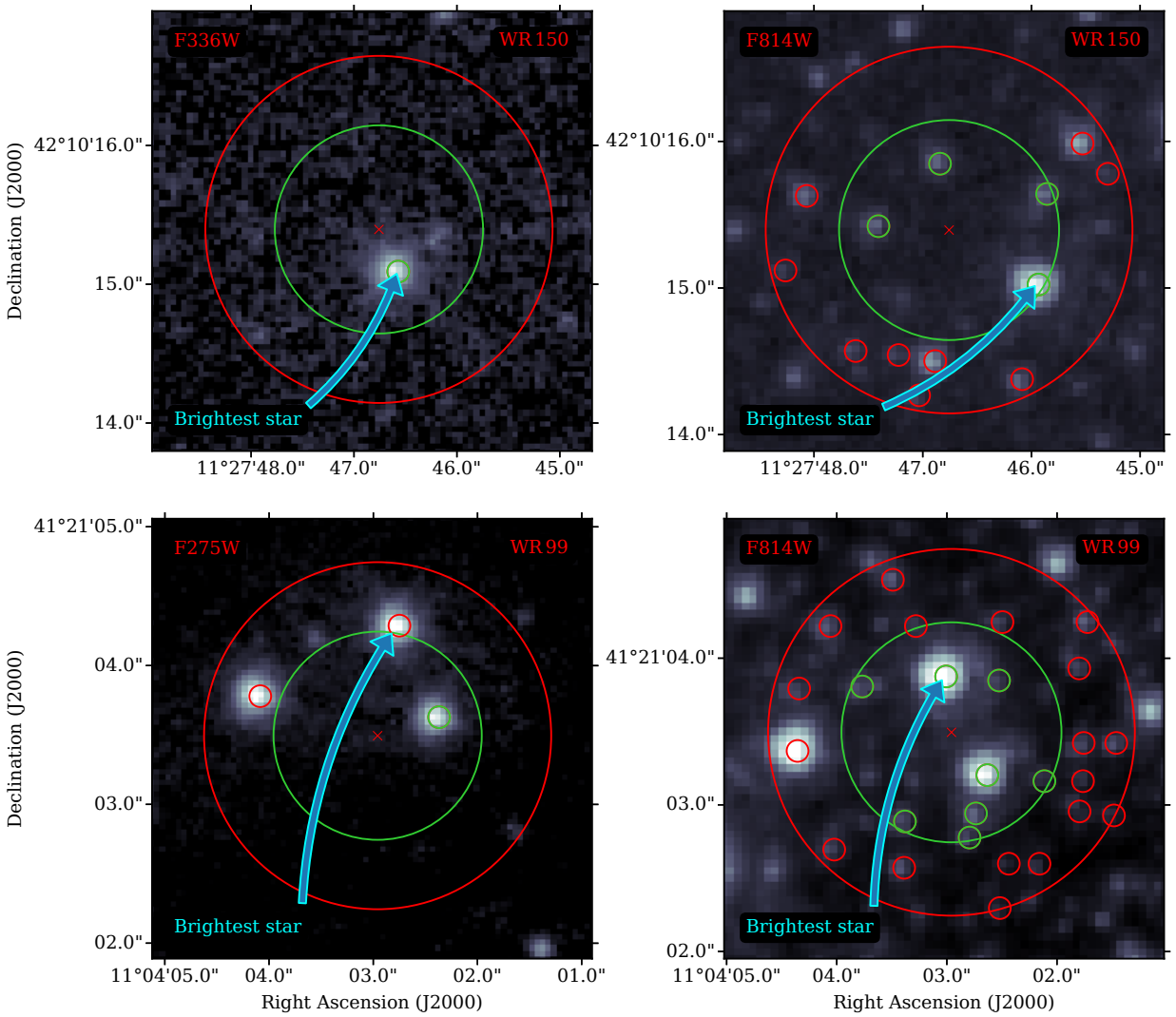

Figure 13: *HST images taken in a red and a blue band for M 31 WR 99 and M 31 WR 150 each. The large green circle indicates the fiber aperture of Hectospec ($d = 1.5''$) with the red cross marking the central point which corresponds to the cataloged position of the stars. The large red circle denotes a radius $0.5''$ larger to illustrate average seeing conditions. Small circles (green and red) show sources with available HST photometry in this band and the color coding shows if they are inside the aperture or seeing radius. The brightest source inside the seeing radius is highlighted. While for WR 150 this is undoubtedly the WR itself. For WR 99, this is not clear.*

The remaining 35 stars are now investigated further. For some of them a significant spectral contamination can be ruled out. Others are not as clearly diluted as the already ruled out stars, but contamination cannot be excluded completely. Those 13 stars (21%) are the *suspects*. For those stars, listed in Table 6, we will attempt to perform a spectral fit as single star, but they are discarded from the later discussion of the results.

From the original sample only 23 spectra (37%) remain that can be assumed to be not contaminated significantly. Those *single* stars are listed in Table 7 and await spectral analysis. Further problems that occurred with spectroscopic data will be addressed in Sect 7. The share of stars assigned to each category

[14] The offset is $\simeq 1''$

Table 6: *M31 WC stars falling into the* suspect *category*

WR #	LGGS	Spectral type	WR #	LGGS	Spectral type
4	J003933.46+402018.9	WC5	59	J004242.03+412314.9	WC7
26	J004043.28+403525.2	WC6	62	J004249.84+410215.7	WC5-6
33	J004107.31+410417.0	WC6	71	X004308.25+413736.3	WC6
49	J004147.24+410647.5	WC8	80	J004331.17+411203.5	WC8
51	J004154.62+404713.8	WC6	84	J004341.72+412304.2	WC6
56	J004234.42+413024.2	WC8	141	J004531.16+420658.1	WC6
58	J004240.81+410241.6	WC6			

Table 7: *M31 WC stars without spectral contamination that are treated as* single *stars*

WR #	LGGS	Spectral type	WR #	LGGS	Spectral type
2	J003911.04+403817.5	WC6	96	J004412.44+412941.7	WC6
7	J003939.97+403450.4	WC6	102	J004422.24+411858.4	WC7-8
12	J004019.47+405224.9	WC4	113	J004436.52+412202.0	WC5
13	J004020.44+404807.7	WC6	121	J004451.98+412911.6	WC7
15	J004022.43+405234.6	WC4	123	J004453.52+415354.3	WC7
19	J004029.27+403916.6	WC5	124	J004455.63+413105.1	WC6
23	J004034.69+404432.9	WC4	132	J004511.27+413815.3	WC6
43	J004134.99+410552.3	WC7	138	J004522.78+420318.2	WC5-6
54	J004213.21+405051.8	WC4	139	J004524.26+415352.5	WC6
55	J004214.36+412542.3	WC6	150	J004551.12+421015.4	WC5-6
93	J004408.58+412121.2	WC6	151	J004551.35+414242.0	WC6
94	J004410.17+413253.1	WC6			

is illustrated for the individual spectral types in Fig. 14. The spatial distribution is shown in Fig14. The contamination by cool stars, namely RSGs, will be treated differently, as their impact is only visible in the red part of the spectrum. We will discuss this further in Sect. 7.2.6.

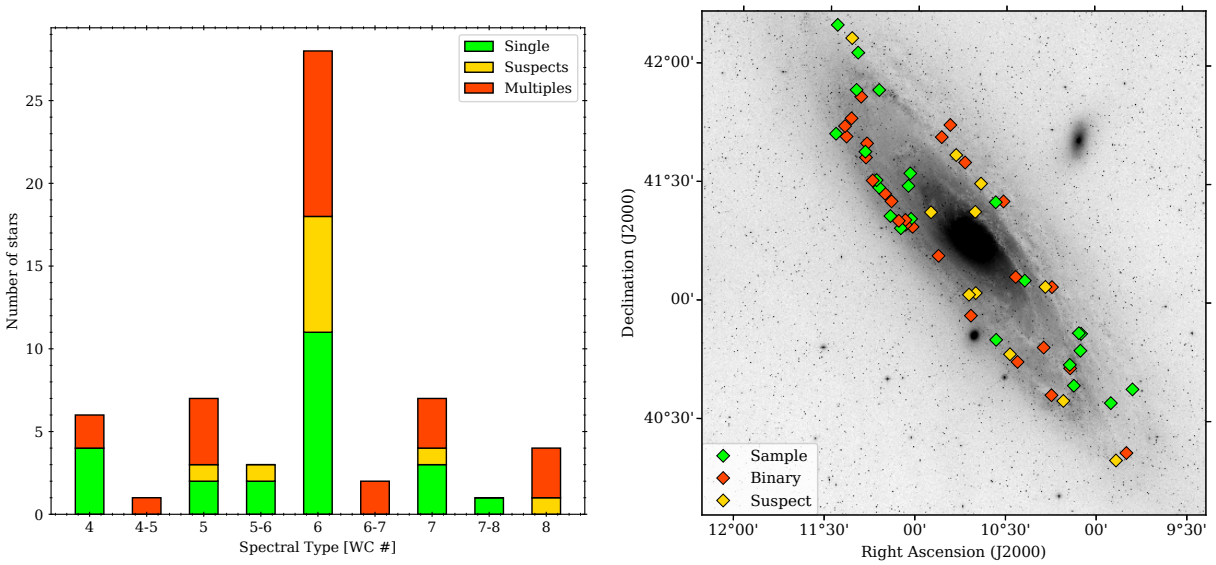

Figure 14: *Fractions of stars assigned to the categories* single, multiple, *and* suspect *according to their spectral appearance. The color coding marks stars identified as* single *(green),* multiple *(red), and* suspects *(yellow). The two stars without a spectrum as well as two stars without detailed classification are not shown*
Left panel: *Histogram depicting the fraction of stars resolved for the spectral types*
Right panel: *Spatial distribution of the WC stars in M31. Background image: DSS2 blue on inverted gray scale*

6 Modeling stellar atmospheres

»Gray, my dear friend, all the theory is; and red the synthetic atmosphere's emergent spectrum.«

– Johann Wolfgang von Goethe, loosely based

A spectral analyses of a star is handled with the help of models. A synthetic stellar atmosphere is created, containing all relevant physics in a numerical approach. From such an artificial atmosphere, a synthetic spectrum is calculated. The resulting spectra are compared to observations. We vary the model parameters until the observation can be reproduced.

The following paragraphs are only meant as a short overview to the model calculation. As this work itself is mainly observational based, a more detailed focus on the theoretical framework of stellar atmosphere models is beyond the scope of this work. However, at various points throughout this work, we will encounter situations where parts of the actual methods and processes of the calculation become important. Those parts of the calculation will be addressed there.

6.1 PoWR-full model spectra

To analyze the observed spectra, we fit them with synthetic spectra calculated with the Potsdam Wolf-Rayet model atmospheres code (PoWR).

The general concept of PoWR is a solution of the radiative transfer equations and the calculation of the population numbers in an iterative manner. PoWR sets up an one dimensional and expanding atmosphere under the assumption of spherical symmetry. Due to the strong radiative field, the plasma is in an highly non-LTE situation. The radial density distribution is given by the mass loss rate $\dot{M}$ and wind velocity field $v(r)$ via the equation of continuity

$$\rho(r) = \frac{\dot{M}}{4\pi r^2}\frac{1}{v(r)}. \tag{5}$$

For computational reasons, the radial dependency is discretized with a radial grid of depth points r_i. The inner boundary of the calculation is set to the radius R_*, where the mean Rosseland depth is $\tau_{\mathrm{Ross}} = 20$. The outer boundary is usually set to $100 - 1000$ stellar radii R_*. The stellar temperature T_* relates to R_* and the luminosity L via the Stefan-Boltzmann-law

$$L = 4\pi\sigma R_*^2 T_*^4. \tag{6}$$

At each depth points, the population numbers are calculated from the statistical equilibrium equations that depend on the temperature $T(r_i)$ and radiative field $J_\nu(r_i)$. The radiation field itself is then recalculated from the new population numbers (Koesterke et al. 2002). Furthermore, temperature corrections are applied to guarantee energy conservation (Hamann & Gräfener 2003). Also, line blanketing effects are accounted for (Gräfener et al. 2002). As can now be seen, the radiative field and population numbers are coupled and a consistent solution can only be achieved iteratively and special methods have to be employed to achieve convergence (accelerated Λ operator, Hamann 1987). Therefore, PoWR calculates them alternating over and over again from each other until the changes compared to the previous step are smaller then a preset threshold. A model that has reached this level is called converged. Details of the calculations can be found in Hamann (1987).

Since the models we are going to use are for WC stars, the stellar winds are optically thick in the continuum. T_* is by far not identical to $T_{2/3}$, which refers to the radius where the Rosseland optical depth has dropped to $2/3$. The latter temperature gives a better characterization of the spectral appearance of the star.

For the expanding part of the atmosphere, the velocity field $v(r_i)$ is prescribed in the form of a β-law, where the exponent β and the terminal velocity v_∞ are free parameters, such as

$$v(r) = v_\infty \left(1 - \frac{R_*}{r}\right)^\beta \tag{7}$$

or alternatively with a double β-law, where two laws using a different exponent are used to describe the velocity field as

$$v(r) = v_\infty \left[q_1 \left(1 - \frac{R_*}{r}\right)^{\beta_1} + q_2 \left(1 - \frac{R_*}{r}\right)^{\beta_2}\right], \tag{8}$$

with the weight factors $1 = q_1 + q_2$.

In the hydrostatic domain of the stellar atmosphere, basically identical with the stellar photosphere and the subsonic part of the wind, the quasi hydrostatic equation is solved (Sander et al. 2015). For a WR star, where the optical depth in the wind is high, the hydrostatic domain is usually not encountered before the inner boundary is reached.

The microturbulence affects the line formation. We specify the micoturbulent velocity in the formal integral by its minimum value $v_{\rm mic}$ at the photosphere and a contribution that grows in proportion to the wind velocity (see also Shenar et al. 2015).

Wind inhomogeneities are accounted for in the microclumping approximation (Hamann & Koesterke 1998), i.e. under the assumption that all clumps are small enough to be optically thin at all frequencies. The density in the clumps is enhanced by a factor D compared to a homogeneous wind with the same mass loss, while the interclump space is assumed to be void. There are indications that clumps exist already at, or very close to, the photosphere (Cantiello et al. 2009; Torrejón et al. 2015). As the photosphere is not visible for a WC star, we assume the clumping factor to be constant.

Photospheric absorption lines show pressure-broadened profiles. Fitting their wings is the main diagnostic for the star's gravity $\log g$. Pressure broadening is taken into account in the formal integral of the equation, which yields the emergent spectrum in the observer's frame. From the star's gravity $\log g$, the stellar mass is then calculated via the radius. However, a WR star does not show any photospheric lines in its spectrum and only the wind is visible[15]. The estimation of the stellar mass and gravity is based on theoretical consideration from Langer (1989) for a helium burning star (see their equation 19). Following these calculations, the mass is a function of the helium mass fraction and the stellar luminosity.

The rotational broadening of photospheric lines can be simulated by convolving the emergent flux spectrum with a semi-ellipse. However, for lines formed in the stellar wind this is a poor approximation. Therefore, we perform a full 3D integration (Shenar et al. 2014), assuming co-rotation of the photosphere ($\tau_{\rm Ross} > 2/3$) and conservation of angular momentum in the wind. The co-rotation radius $R_{\rm corot}$ is a free parameter and is set here initially to $1.1R_*$.

The models calculated for this work account for complex model atoms of He, C, N, O, Si, P, Ne, and S. Not every model includes actually all the aforementioned elements, the included elements are listed for each model separately below. Iron-group elements are treated with the superlevel approximation (Gräfener et al. 2002). A list of the included ions as well as the number of accounted levels and transitions is given in the appendix in Table 15.

The dominating elements in a WC star, He, C, and O, are strongly enriched. The other included elements are assumed to have solar abundance (adopted from Asplund et al. 2009).

It has turned out to be convenient to use the transformed radius $R_{\rm t}$ instead of the mass loss rate as parameter to describe the wind. This parameter does not describe a physical meaningful radius for the star, but is related to the inverse wind density and reduces the number of free parameters from three to two (T_*,L,$\dot{M}$ $\rightarrow$ T_*,$R_{\rm t}$). It is calculated as

$$R_{\rm t} = R_* \left(\frac{v_\infty}{2500\,{\rm km\,s^{-1}}} \left(\frac{\dot{M}\sqrt{D}}{10^{-4} M_\odot/{\rm yr}} \right)^{-1} \right)^{2/3} . \tag{9}$$

The model grid described in the next section is build with regard to this parameter.

6.2 The model grid

It would now be possible to have a look on the spectrum of each individual star, assume reasonable parameters, e.g. from Sander et al. (2012), calculate a model for each star, and start to iterate on the model to improve the fit. But this is an inconvenient process and a waste of time as there are already model grids for certain kinds of stars. Those model grids[16] exist for OB and WR stars for MW, SMC, and LMC metalicities. The metalicity of M31 is comparable to the Milky Way. The Galactic WC grid was adopted as a starting point. Because of a recent PoWR update[17], the grid on the web page was outdated and was currently recalculated. The unfinished grid was adopted and completed (see Fig. 15). Latter means that the hot and dense models were still missing and calculated throughout the starting phase of the present work. At this point, the grid contained 166 models. The grid is two-dimensional. The two dimensions are the stellar temperature T_* and the transformed radius R_t.

The original WC grid kept all other parameter constant, with the exception of $T_{\rm eff}$ and R_t. Constant were in particular

[15] Note that we use the term photosphere here in a sense to denote the hydrostatic part of the atmosphere and not as reference to the layer where the spectrum emerges.

[16] Available under: www.astro.physik.uni-potsdam.de/PoWR/

[17] To include parity splitting for iron

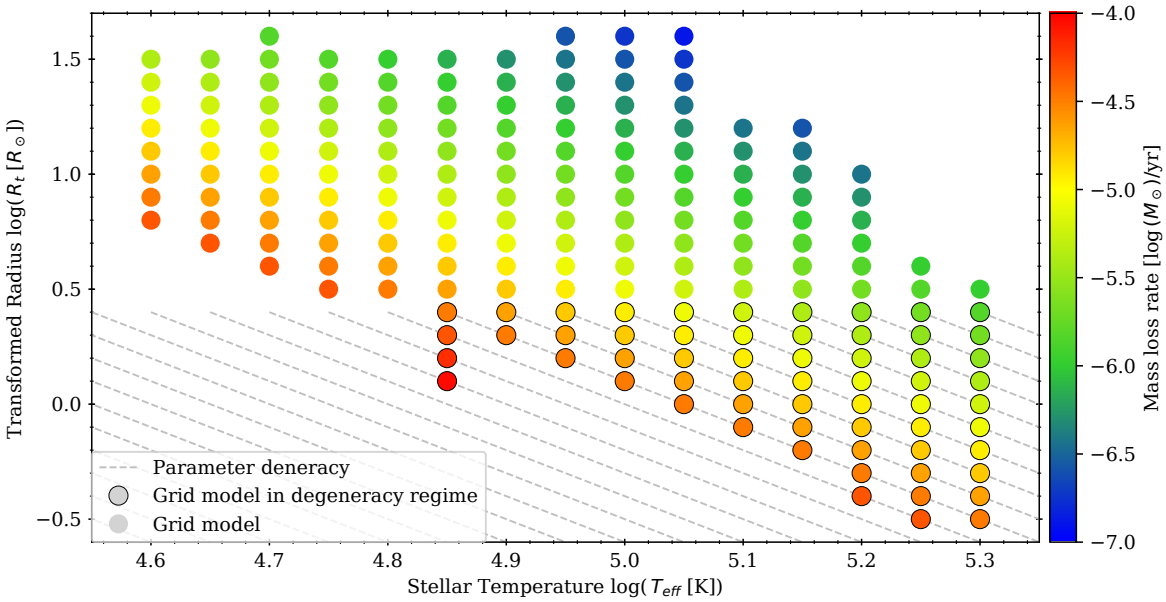

Figure 15: *WC grid adopted for a first look at the models. Each circle represent a grid model and the color coding gives the mass loss rate. The gray lines indicate the region of parameter degeneracy. More on that in Sect.7.5*

- the luminosity, set to $\log L/L_\odot = 5.3$;
- the clumping factor, set to $D = 10$;
- the chemical composition, set to 40% carbon, 5% oxygen, 55% helium, and 0.16% iron group elements (e.g. solar abundance, Asplund et al. 2009), all given as mass fraction;
- the terminal velocity, set to $v_\infty = 2000\,\mathrm{km\,s^{-1}}$;
- the velocity law exponent β, set to $\beta = 1$.

Further model properties follow from the calculations, e.g. stellar mass, radius, and $\log g$.

In the following, we will refer to grid models in a specific way, which will be introduced now. The grid models are addressed according to their position on the grid with the grid coordinate $\mathcal{T}$-$\mathcal{R}$. Hereby denotes $\mathcal{T}$ temperature index and $\mathcal{R}$ the transformed radius index. From the grid coordinate (e.g., 12-18) the stellar temperature T_* and transformed radius R_t can be calculated via

$$\log T_* = 0.05 \cdot \mathcal{T} + 4.35$$

and

$$\log R_t = -0.1 \cdot \mathcal{R} + 2.1.$$

The model grid is build in such way that the mass loss rate along a diagonal line from low grid indices to high grid indices each, stays constant (see Fig. 15). Or in other words the models 12-18 and 18-24 do have the same mass loss rate at different temperatures. Also there is a spectral degeneracy for very dense models ($\log R_t < 0.5$) of same mass loss, that will be addressed later. It is therefore convenient to introduce the following: we will address such a diagonal line as ith diagonal, where i corresponds to the difference between the grid indices

$$i = \mathcal{R} - \mathcal{T}.$$

Hence, 12-18 and 18-24 are therefore both on the 6th diagonal.

7 Spectral analysis

» The right understanding of any line and a misunderstanding of the same line do not wholly exclude each other. «

– Franz Kafka, loosely based

With the model spectra at hand, we can now dive into the spectral analysis. The principles are fairly simple. A synthetic spectrum from a model calculation is compared to the observed spectrum. The goal is a reasonable good reproduction of the observation by the model. Different models of the grid were compared to the observations and – when necessary – new models were calculated. The dependence of spectral lines of the model parameters indicates how to adjust the parameter to obtain a better fit. In reality this process is much more tricky then it sounds here, especially as WC spectra are much harder to reproduce then OB or WN spectra. The general fitting process as well as some of the issues and problems, their solutions, and workarounds are described on the following pages.

7.1 Automated fitting

With a grid of 166 models at the beginning, a sample of 59 stars that have a spectrum, >6 free parameters for the models, a blind start by just randomly picking models and comparing them to the observations would have been pointless. A more elegant approach was developed to find a better starting point for the single stars. The observations and all grid models were fed into an automated tool that compared the individual observation to each grid model, yielding the best fitting models as result.

The fitting process itself employed a very primitive approach but has proven to be helpful for a certain set of models. The model spectra were read in and the tool interpolated linearly on the wavelength scale to obtain the same wavelength grid as present for the observation. Now the difference between the normalized observation and model were calculated on the basis of the wavelength points of the observation. The RMS of those differences for all wavelengths was then used as indicator for the quality of the fit.

This simple approach suffers from issues with the observations. As it just took the simple difference between model and observation, the grading of the model strongly depends on the S/N of the observation, the quality of the normalization, and the amount and strength of nebula emission lines. The quality of the normalization was improved over time, but in the blue range of the spectra the continuum is not always clearly visible. The regions where strong nebula emissions occur where manually cut out form the wavelength range adopted for comparison. However, the biggest problem was due to the S/N of the data. An attempt to overcome this by weighing the calculated difference with flux error for each wavelength failed due to the lack of reported flux errors in the observational data. Another attempt to solve this issue by binning the data, did not show much improvement to the fitting process.

Despite those issues, the fitting tool was helpful to get a starting point for models which are not strongly contaminated by nebula lines or that do not have a low S/N. Due to the fact that a low S/N always appears in spectra with strong nebula emission and for stars with photometry that indicate high reddening, both of those issues affect basically the same set of stars. For the remaining spectra, about half of the sample, the fitting tool was able to give valuable starting points for the manual fitting process.

The tool was not only used to find a starting point, it also provided a nice consistency check later on. With an extended model grid, including models that now account for different carbon abundances, additional elements like silicon and partly nitrogen, and different terminal velocities, the tool was able to identify the models with the right velocities and abundances as fitting best.

7.2 The ways and means to fit a WC spectrum

On the following pages, we address the way how the fitting process for the individual stars went on and how the spectral features can be used to derive stellar parameters. Furthermore, we will discuss issues that occur during the fitting process and have a closer look on lines that could not be fitted by any means.

7.2.1 The *diagnostic pair* and the carbon abundance

The *diagnostic pair* are two close-by lines that have proven to be an indicator for carbon abundance in WC stars. It consists of the He II λ5411.6 line, which is the transition between the 7th and the 4th state in single ionized helium, and lines from the C IV $\lambda\lambda$5356–5519 multiplet. From the multiplet the lines around λ5470 merge due to the wind broadening into a single emission line. At a carbon mass fraction of 40 %, which is typical for WC stars, the ratio between those two lines is about unity, usually in peak height as well as in equivalent width. If a star has a different carbon abundance, the line can work as an indicator as the

line ratio changes. In Fig. 16, this is shown for the spectra of the three program stars WR123, WR113, and WR13, with a carbon mass fraction of 35 %, 10 %, and 60 %, respectively.

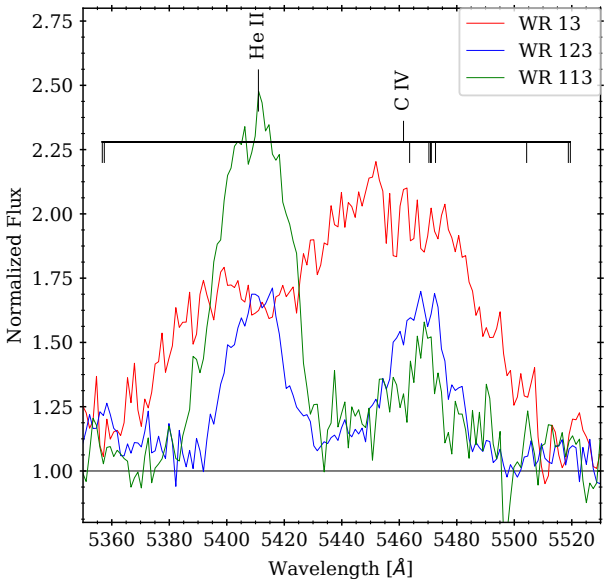

Figure 16: *Comparison of the diagnostic pair for different carbon abundances in the spectra of WR13 (C = 60%), 113 (C = 10%), and 123 (C = 40%).*

Unfortunately this line is not an indubitable indicator. There are additional temperature effects that have to be accounted for, but those are usually minor. In the present work, the carbon abundances derived from the diagnostic pair is nicely confirmed by other helium and carbon lines for most stars.

Another problem arises when the line profile gets very weak. Even in a spectrum that overall inhibits strong lines, the diagnostic pair can have a low equivalent width. These lines are merging, disappearing, or both, cf. Fig. 17. As long as the lines are still somewhat noticeable, like for WR 13, 4, and 7 in this figure, it is still possible to determine the carbon to helium ratio, but for WR 12 it is basically impossible using this line. The carbon abundance has to be determined in a different manner.

Furthermore, it turns out to be very hard to reproduce those kind of weak lines. Only models with very thin winds are able to reproduce the observed line strengths. But those model are highly inconsistent with the rest of the observed spectrum while the line shape of the diagnostic pair can be reproduced.

Merging lines are simply due to high terminal velocities, e.g. the terminal velocity of WR 13 is found to be 2500 km s^{-1}. This is widely consistent with terminal velocities determined from other lines. But for some stars it is not. The diagnostic line pair appears to merge stronger, e.g. the terminal velocity determined from other lines for WR 4 is also 2500 km s^{-1}, but to reproduce the line profile of the diagnostic pair $v_\infty > 3000$ km s^{-1}would be required.

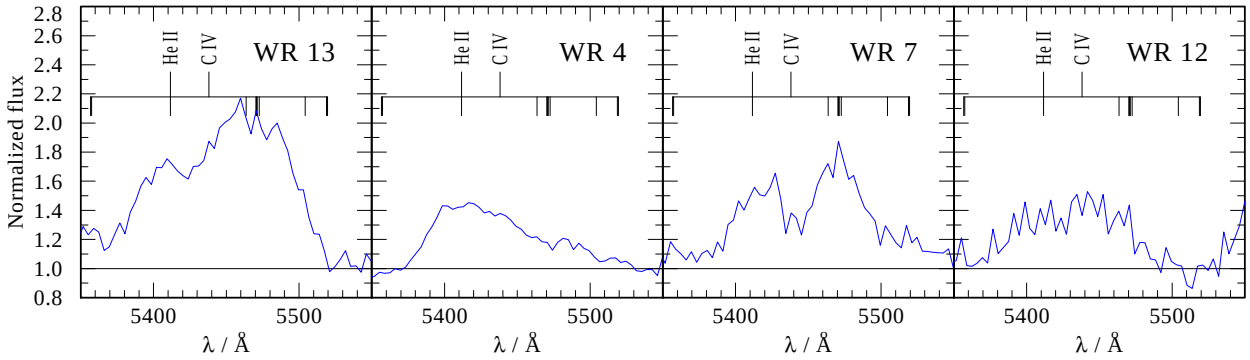

Figure 17: *Comparison of the diagnostic pair in the spectra of WR 13, WR 4, WR 7, and WR 12.*

An attempt to cope with this problem by changing the wind velocity law, which also has an impact on the line shape, failed. The lines appear to merge for lower velocity law exponent β, but the effect is not strong enough to make a significant difference in line shape. Another parameter that impacts this line shape is stellar rotation.

Despite those problems, the diagnostic pair still works as an indicator for the carbon abundance in the WC spectra, and we can easily reproduce the line ratios in it. However, most fits strongly overpredict the total strength of the lines, and the merging line profiles can only be reproduced partly.

7.2.2 Carbon and helium – the iconic lines in a WC spectrum

Wolf-Rayet spectra are outstanding due to their strong emission lines. The most prominent among them are those used for their spectral classification. For WC there are:

- C IV $\lambda\lambda$5802, 5810, due to its merging line profiles often referred to as C IV λ5808, is generally among the strongest observable emission line in the spectrum, with a peak height of more then 20 in a normalized spectrum. The red wing of this line merges with He I λ5877 for higher terminal velocities and line strengths.

- The only line often observed with an even higher peak height is a blend between C III $\lambda\lambda 4647-4651$, He II λ4686, and C IV $\lambda\lambda 4646-4665$. We address this blend in the ongoing text simply as He II λ4686, referring always to the entire blend until noticed otherwise. This blend is sometimes also referred to as the Bowen blend (Bowen 1928).

- C III λ5696 shows the highest sensitivity to the stellar parameter and varies between different stars from absent to equal height compared to C IV $\lambda\lambda$5802, 5810.

At first impulse, declaring those lines to the key diagnostics for the spectral analysis of such stars seems not far fetched. But one needs to proceed with caution. Previous analyses (e.g. Sander et al. 2012) have shown, those lines are hard to reproduce, not only their intensity but also their partly very abnormal line shapes. Furthermore, a line that has a peak height of 20 in a normalized spectrum is highly sensitive to the adopted normalization. With an uncertainty of a factor of 1.5 for the continuum, which is encountered for some of the stars analyzed here, the peak height varies between 20 and 30.

How can we still use the information from those lines? In this work, we attempt to use the ratios of those lines. Whenever the continuum cannot be determined clearly from the observation, we adopt the continuum as seen in a model. The models themself show around this line a normalized fluxes greater then unity. The normalization of the observations is adjusted in a way that the spectrum around the line, meaning the weaker and unresolved lines and their merging line wings, match the current model for comparison. To not invoke unwanted errors that can happen when normalizing a spectrum with to many continuum points, we set only four points, two redwards and two bluewards of He II λ4686, and none inside the line. Those points are then fitted by a low order polynomial which is used to represent the continuum.

Let's have a look on some line systematics for those emission lines. Clearly, we cannot use the observations for that, as we do not know the stellar parameter and the carbon to helium ratio. Furthermore, the number of stars is not high enough to identify the systematics here. Instead, we are using the calculated model grid. In the original grid, all models have the same terminal velocity and carbon abundance, which makes it the ideal point to start[18]. We take the peak height of the above mentioned lines and investigate the evolution of the lines along the grid models. Of course, the lines are more then just their peak height especially for the line blends, but line width and shape, as well as instrumental broadening are only second order effects now and will be considered in the spectral fit later on.

In the Fig. 18, we show the peak heights of the aforementioned lines across the model grid normalized to its strongest appearance throughout the model grid. We see the constrain for C III λ5696. Only models with certain wind density show this line. And the line is getting strong quickly with increasing wind density. For all models that show C III λ5696, the final solution for a model has be along this narrow strip across the model grid. Models with thinner winds do not show this line at all.

For He II λ4686 a central region stands out. Some models in this region predict a peak height of 120 and enormous equivalent widths, far more then any observation show. Those models are considered irrelevant for the modeling process. The lines are getting very weak for hot models with thin winds.

This gives us another constrain on the fitting process. The region of high peak height in He II λ4686 and C III λ5696 are not parallel on the model grid, those region merge for higher temperatures. Therefore, the line ratio between those two lines can tell us something about the position along a grid diagonal and consequently about the stellar temperature T_*. But the effect is very small and leaves us still with a large region along the grid with similar ratios. If we have a look at those ratios, see Fig. 19, it becomes obvious that the grid spacing might not be sufficient to grant all the insights we desire as the changes to line strength are too strong on the grid resolution.

Now we can have a look on C IV λ5808 (Fig. 18, lower left panel). We see a clear peak at the 6 th diagonal. Furthermore, there is a second peak visible in the 2nd diagonal. This is not the C IV λ5808 emission anymore. The emission of He I λ5877 dominates the blend. But at this point, the models reach a regime where the

[18] Note that for some of the model grids plots of equivalent width exist for selected lines. For the newly calculated galactic WC grid, those don't exist so far. The difference to the plots made for the outdated WC grid should be minor but a first check revealed differences. Therefore, we choose not to rely to much on them here.

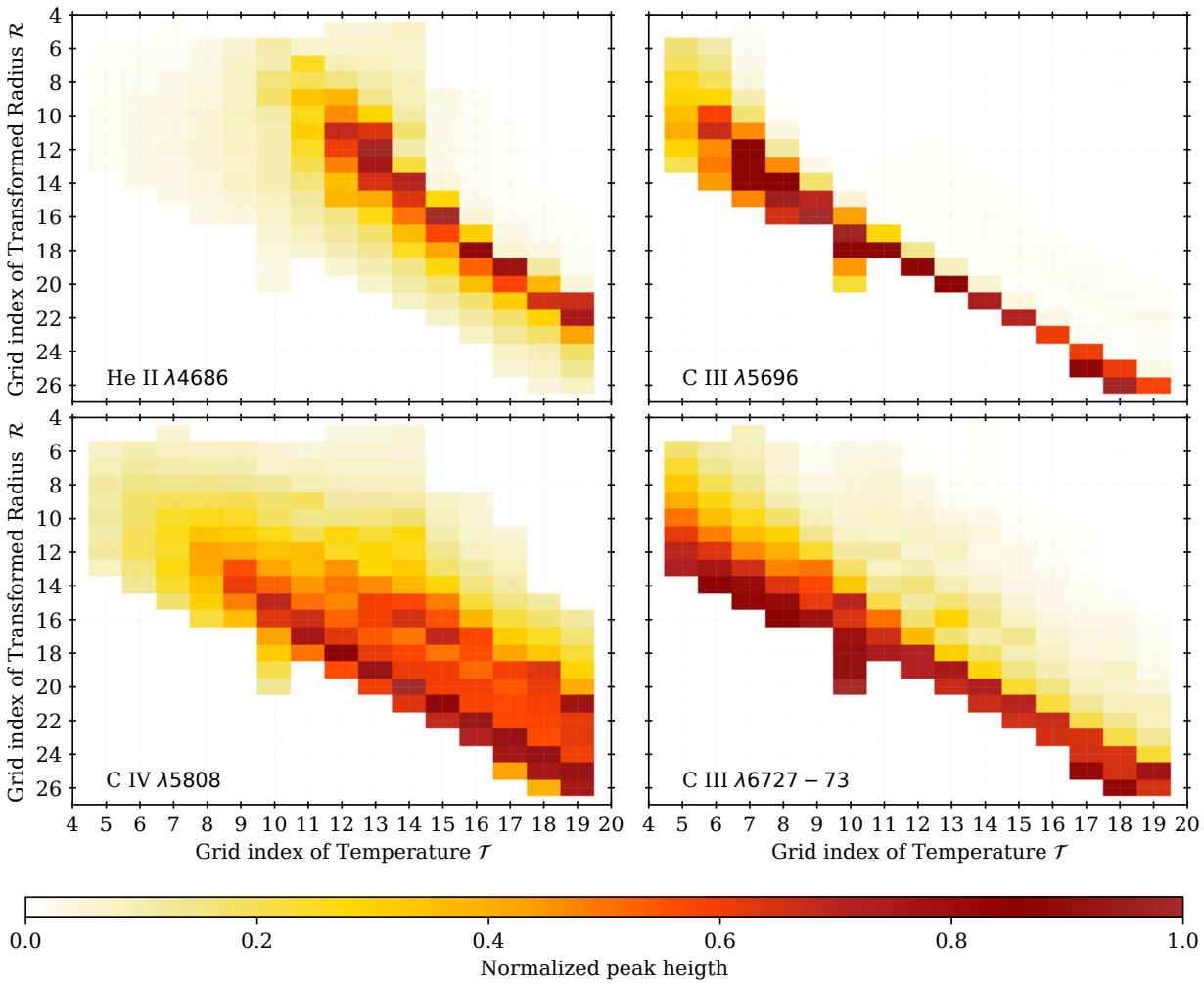

Figure 18: *Peak heights of selected lines, calculated from the original model grid without further adjustments. Grid plot like in Fig 15; the color coding gives the peak height*

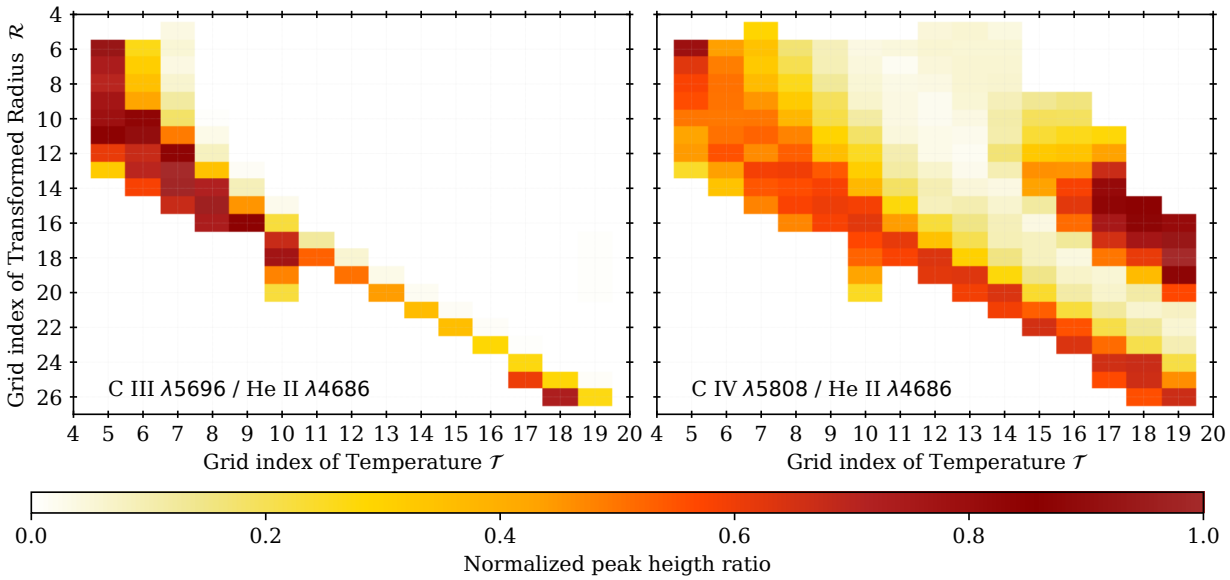

Figure 19: *Line ratios of* He II *λ*4686 *to* C III *λ*5696, *and* C IV *λ*5808 *to* He II *λ*6560 *calculated from the original model grid without further adjustments. Grid plot like in Fig 15; the color coding gives the normalized peak height ratio*

spectra are entirely inconsistent with observed WC spectra. Furthermore, in non of the present spectra this is observed.

We added another multiplet to Fig. 18, which is C III $\lambda\lambda 6727 - 73$. This line behaves similar to C III $\lambda 5696$ but is not identical. It can be a useful indicator for the mass loss rate when the winds are too thin to show C III $\lambda 5696$ because C III $\lambda\lambda 6727 - 73$ does not vanish in a similar fashion.

One reason to investigate those lines in such detail is their importance for the spectral classification. It is assumed that an earlier spectral type implies a hotter star. The spectral types are assigned according to the line ratios, mostly carbon lines. Lines of higher ions indicate an earlier type and a higher T_*. Derived stellar temperature T_* of a star should follow the classification. But for a WR star, where the spectrum forms far away from the stellar surface, this temperature loses its spectroscopic relevance. More important in this context is the temperature within the stellar atmosphere at which point the opacity has dropped to a level which allows the light of the star to leave. Therefore, we adopt the effective temperature of the radius where the optical depth has dropped to 2/3. Radius and temperature are denoted as $R_{2/3}$ and $T_{2/3}$. Figure 20 shows $T_{2/3}$ for the adopted model grid.

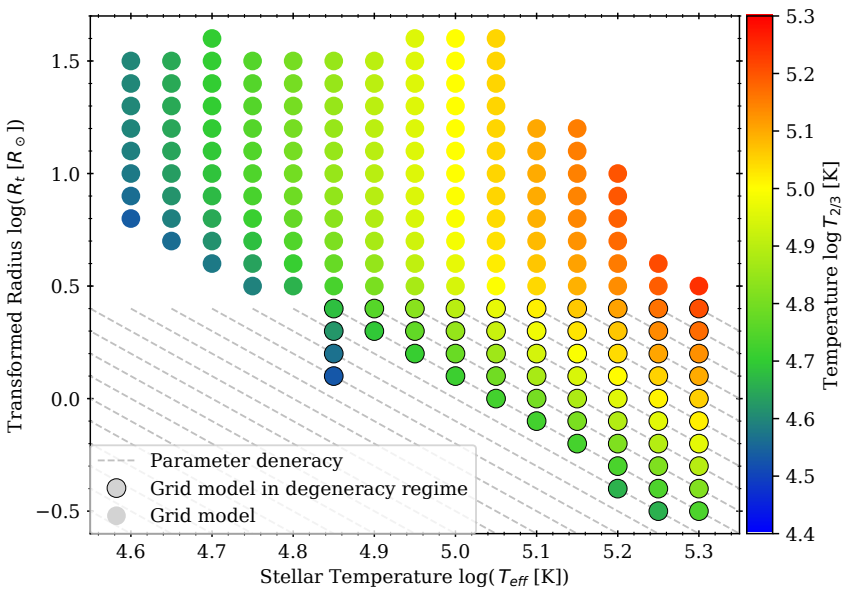

Figure 20: *Grid plot for the standard grid as in Fig. 15. The color coding indicates $T_{2/3}$.*

The ionization balance of the star is determined by the radiation field. Also the stellar temperature plays a role, but for a hotter star, the region where the spectrum forms just moves further inwards. This is also shown by the Figs. 18 and 15. Similar line strengths are reached for spectra from stars with highly different T_*. Thus, the spectral type of the star has to be independent of T_*. And stars with the same spectral appearance can be in principle of very different nature. Also the expectation of finding the earliest types to be furthest evolved stars is not necessarily adequate. We will investigate further problems with the spectral classification below.

7.2.3 The inclusion of other elements

The WC spectra are dominated by carbon and helium lines. Also oxygen lines are clearly visible. Therefore, the grid models are calculated including those three elements. Additionally, the models contain the iron group elements. There are no visible iron lines in the optical range, but the impact of iron cannot be neglected. The standard grid models contain 40 % carbon, 5 % oxygen, and 0.16 % iron by mass. The rest is helium. A successive inclusion of other elements, namely neon, sulfur, phosphorus, silicon, magnesium, sodium, fluorine, chlorine, and aluminium resulted only for silicon in a noticeable change of the emergent spectrum. However, the inclusion of silicon brought not only a significant change in the spectrum, but it also enhanced the fit quality locally.

As already mentioned, WC spectra are generally much harder to reproduce with model spectra than WN or OB spectra. One of the problems in the optical is a line feature around 4100 Å. In a WC star, the spectrum shows a complex structure being a blend of several lines. Reproduced by model spectra are usually a C III doublet and He II ($n = 12 \rightarrow n = 4$). However, the overall structure of this line blend is only poorly reproduced by the models, generally it is strongly underestimated. A fit of this blend is difficult, it is sensitive to various parameter. The carbon to helium ratio impacts the shape of the blend while the total amount of emission stays constant for different ratios.

This is now the point where the previously mentioned local enhancement of the spectrum quality with the inclusion of silicon comes in play (see Fig. 21). Si IV $\lambda\lambda 4088, 4116$ appears as strong emission, helping to overcome the fitting issues with this blend partly. Issues remain as there seems to be still something missing in the red part of this blend.

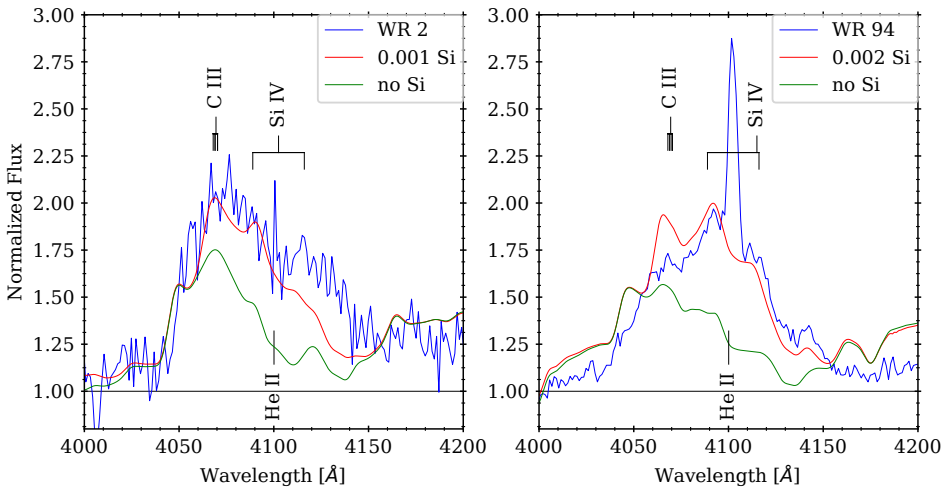

Figure 21: *Comparison between the observed spectra of WR 2 and 94 (solid blue lines) and the best fitting model with silicon included (solid red line) and the same model without (solid green line) for the line blend around* 4100 *Å*

An element with a somewhat special situation for WC stars is nitrogen. According to the evolution theory, WC stars have lost most of their nitrogen. However, the transition between WN and WC is continuous, and the enrichment of carbon and the depletion of nitrogen happen gradually. Following that, there should be some stars that show an enrichment of carbon but still with visible nitrogen. And indeed, stars that show these characteristics are among our sample. For those, an inclusion of nitrogen in the models is necessary.

The amount of nitrogen and silicon included for the individual stars is listed below (Tables 18c – 40c). Silicon is included for all models, nitrogen only for those stars where clear nitrogen features are visible. Note that we derive a super solar silicon abundance for the majority of the stars. This might be due to the fact that the above mentioned blend does also consist of further, unknown emission lines. The derived silicon abundance here is therefore only an upper limit.

7.2.4 Radial velocities

The radial velocity of a star is usually determined by line shifts due to the Doppler-effect. However, some minor points still have to be addressed here.

The spectrum of a WC stars depict only wind lines. The broad emission lines occur due to emission in the fast moving wind, and therefore, the emission is Doppler shifted additionally to the motion of the star. The measurement of the radial velocity is rather imprecise. Due to the width of the emission lines, all radial velocity have an estimated error of $\pm 50\,\mathrm{km\,s^{-1}}$.

If the emission is anisotropic around the star, e.g. due to an anisotropic wind or simply that the parts moving away from us are hidden behind the star and its wind, the lines lose their symmetry. This is exactly something we can observe and is also reproduced for most lines by the model calculations. In thinner winds, this effect can be observed as P-Cygni profiles. The resulting line profiles appears as if the lines were *leaning* to the side (cf. C IV $\lambda 4486$ in Fig 22).

7.2.5 Oxygen lines

Not all problems can be solved by adjusting the model parameters or including more elements. At certain points, the modeling process encounters its own limitations.

The number of oxygen lines is limited in the spectral range for which observations are available. The O IV $\lambda\lambda 3725 - 3774$ blend marks the blue edge of the observed spectra with a complex structure that makes it impossible to clearly determine the continuum. This line is therefore taken out of consideration here. Most of the observed stars show O VI $\lambda\lambda 3811, 3834$ as a moderate emission. Another, more complex structure contains O IV $\lambda 3934$, and O III $\lambda 3961$, and lines of carbon. This blend is visible as moderate emission in most of the spectra. Bridging the gap between the high and low oxygen ions is the O V $\lambda\lambda 5336 - 5519$ blend. On this line blend an telluric O I emission line is superimposed, which was poorly reduced in the spectra. Additionally to the aforementioned lines, O V $\lambda 5114.1$, and O VI $\lambda\lambda 5270 - 5292$ appear in a P-Cygni shaped profile. The latter one is generally very weak and broad which makes it very sensitive to the adopted

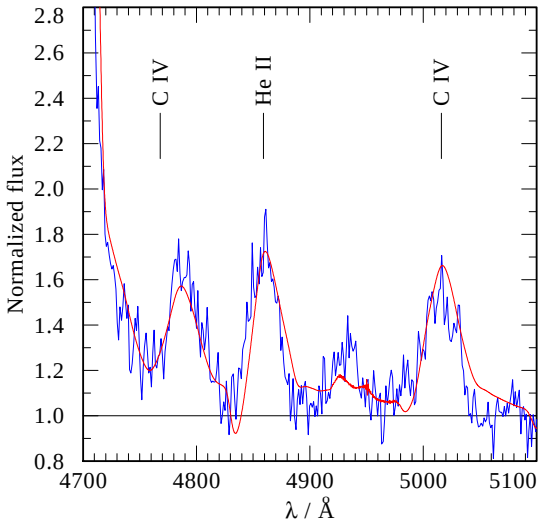

Figure 22: *Observation of M 31 WR 2 (solid blue line) compared to the best fitting model (red solid line) for a selected region where asymmetric lines are visible.*

normalization. Which is why, it is omitted from consideration for the spectral analysis. The spectral ranges that show the above mentioned lines is plotted in Fig. 23 for the sample star WR 2.

Problems occur with the behavior of the oxygen lines in the blue and at $\lambda\lambda 5336 - 5519$. If one adopts a WC model that reproduces the spectrum of a star fairly well, the oxygen lines are usually badly reproduced. Almost all considered observations show the above mentioned lines, while the models do not reproduce O VI $\lambda\lambda 3811, 3834$. At least not in the standard parameter range used to reproduce WC spectra. One needs to go to much thinner winds, to make deeper and hotter layers of the wind visible. However, in this case the entire rest of the spectral fit is inconsistent with the observations. A nice indicator here is C III $\lambda 5695$. This line is highly sensitive to the mass loss rate, and it is only visible for models with thick winds (cf. Fig. 18). The model spectra never show O VI $\lambda\lambda 3811, 3834$ and C III $\lambda 5695$ simultaneously. But in the observed spectra they appear together (see Fig. 23). How comes?

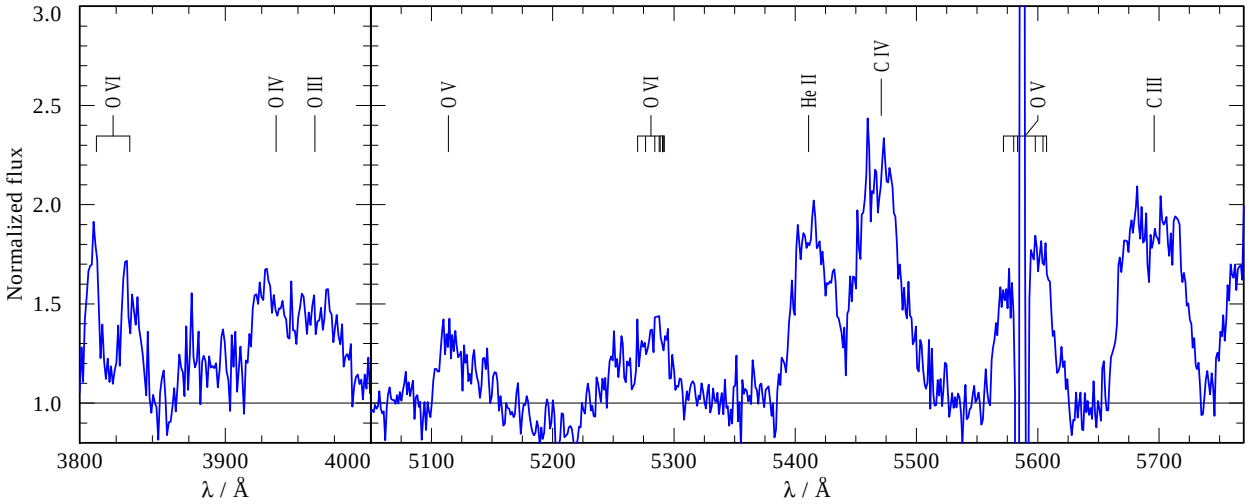

Figure 23: *Two spectral cutouts for M 31 WR 2; the cutouts include all important oxygen lines in the optical spectrum*

The usual picture seen for the oxygen lines is that O III and O IV are overpredicted, O V is reproduced well and O VI not reproduced at all. This might appear as if the temperature is set to low. And this already indicates the cause. The problem is known and the reason might be a shortcoming of the modeling process. The highly ionized oxygen lines originate from layers inside the wind close to the star, the C III line originates further away in colder layers. In a thick wind, the photons from the inner region are scattered before they reach the outer parts, O VI $\lambda\lambda 3811, 3834$ is invisible. A solution to that would be the extension of the model calculation with a two component wind, a dense and low ionized part and a higher ionized and thinner one (cf. porosity and interclumb medium, e.g. Shaviv 2000; Owocki et al. 2004). This would be realized by adopting two different densities for the wind as the temperature's impact on the ionization is negligible compared to the radiative field and the recombination rate is determined by the density. But this is a project for the future and nothing to be solved in the time frame of this thesis. For now, the O VI $\lambda\lambda 3811, 3834$ are taken out of consideration for the spectral analysis. Parameter adjustments are done with remaining lines,

which can be tricky enough already.

The only question remains is, how does this effect influence other lines? How reliable are the synthetic lines ratios of C III/C IV and other elements? This question is difficult to answer. Oskinova et al. (2007) concluded that neglecting the effect of porosity can lead to an underestimation of hot star mass loss rates and that in WR star spectra strong emission lines can be overestimated by a factor of 2 if porosity is not included. Since we can achieve a consistent result for carbon and helium, we assume that this effect is only relevant for oxygen.

7.2.6 The red part of the observed spectral range

A problem with the used spectrograph setting used for the optical observation was that higher order blue light contaminated the recorded spectrum at the red end ($\lambda > 7000$ Å). This should manifest in two ways:

1. The light contamination provides additional flux in the continuum. As a consequence, the lines visible in a spectrum there lose strength in a normalized spectrum.
2. Lines from the blue might become also visible in the red part of the spectrum. The spectrograph works in the first refracting order and the contaminating light originates from the second order. Thus, light from the first order at $\lambda = \lambda_1$ coincides with light at $\lambda = \lambda_2 = \lambda_1/2$ on the detector. The spectral range covered by the available observations is 3700 Å − 9150 Å. A spectral overlapping is therefore expected in the range 7400 Å − 9150 Å with light coming from 3700 Å − 4575 Å.

When we investigate the available spectra, we find:

- Lines redwards Hα are usually overpredicted by the models. While the rest of the spectrum is reproduced satisfyingly, those lines are stronger in the model by a factor of up to 3. Only for a few sample stars the lines are reproduced properly.
- Furthermore, we can observe that for a lot of stars the S/N worsens strongly towards the red.
- The grade to which the spectra a scarred by absorption differs widely.

All of those points can be observed independently from the classification of the star and the identification as *single* or *multiple* star. Figure 24 displays spectra where the mentioned effects can be observed. That all the lines redwards of Hα are overpredicted by the models could have its origin in the line dilution by the second order light. To quantify its influence on the observed spectrum, we can have a look on the strongest emission lines in the blue part of the second order. The strongest feature in this wavelength range is O II $\lambda\lambda$3726, 3728 which originates from nebula emissions. In Fig. 24, it is visible for all stars, and in significant strength for M 31 WR 64 and 94. If we now look at the wavelength equivalent in the first order ($\approx \lambda$6454), we can see a small emission. Furthermore, we can observe the contamination also for Hγ/H II λ4340 in the spectrum of WR 94. In Fig. 25, we show more detailed plot of O II $\lambda\lambda$3726, 3728. There, the normalized spectrum from the first order is shown overlayed by the second order blue light diluted by a factor of 10 and 50 for WR 94 and 140. respectively. With this dilution applied, the second order spectrum reproduces this emission in the first order spectrum. We see that the second order light contributes less than 10% to the observed flux in the red. The line dilution caused by this effect is too small to explain the overpredictions of the models for the lines redwards of Hα. Furthermore, we do see the overprediction of spectral lines for $\lambda < 7400$ Å.

Therefore, we need a different explanation. If the models overpredict emission lines in the red, fit lines in the blue, and that independently of the individual ions that show emissions in these regimes, the reason can be a dilution only affecting the red part of the spectrum. This might be caused by a red supergiant that is capable of outshining a WR star in the red and infrared regime. As the important part of a WC spectrum for us is in the blue to green regime, we neglected this possibility so far. Now we have to reconsider this as a possible explanation for the mismatch in the red. Furthermore, we said already that a late type star would be obvious in the spectrum due to its absorption lines. Matter of fact, most spectra get a very low S/N in the red and some actually do inhabit line features that could be absorption lines originating in a cool star.

But there is another indication, that this overprediction of the red lines is caused by contamination. If we look at the set of photometry for the individual stars and to which fluxes those correspond, it is obvious that the I band photometry indicates a different SED compared to $UBVR$. Stars for which this is very obvious are WR 12, 93, 94, 121, and 132. In Fig. 26, we investigate this potential impact further. The SED of a WR star and two RSGs are approximated as a black body spectrum. A WR star is significantly hotter than a RSG but the latter has the larger radius. This means both stars can have about the same luminosity, while the RSG's SED is much redder. To account for this, we assinged all stars with typical temperatures (100 kK for the WR, and 3.7 kK and 2.5 kK for the RSGs) and radii ($1R_\odot$ for the WR and $500R_\odot$ and $1000R_\odot$ for

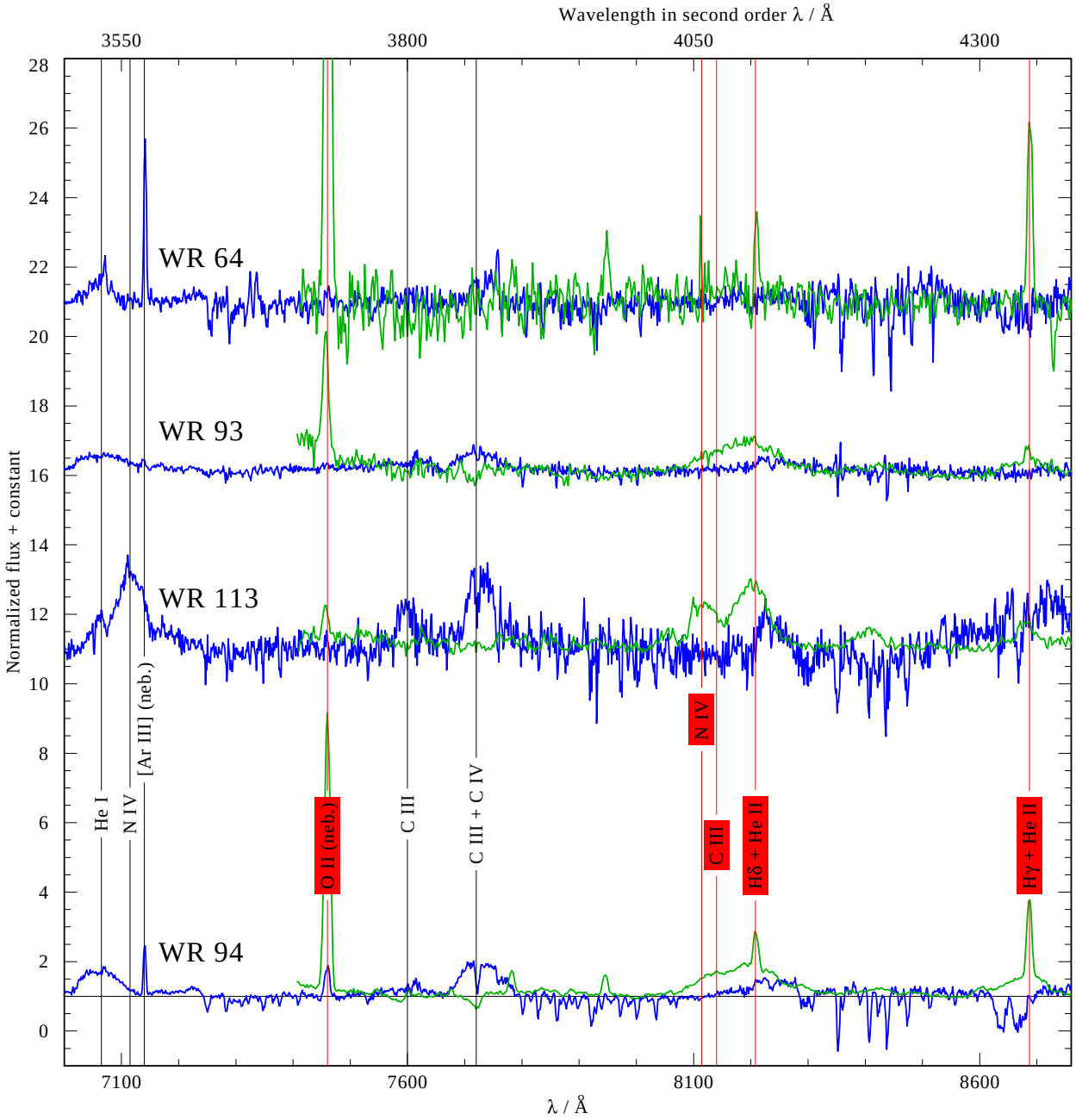

Figure 24: *Normalized spectra (plus constant) of M 31 WR 64, 93, 94, and 113 in the red (blue solid lines), overlayed by spectra of the same stars where the wavelength is multiplied with 2 to illustrated the light from the second order (solid green lines). Line identifications are given for first order spectra (black on white) and for second order light (black on red)*

the RSG). Note that in the figure all radii are normalized to the WR's radius and the absolute flux values are therefore not physical[19].

We can see that a single RSG can have a significant impact on the observed SED (cf. black curve in Fig. 26). The lower panel in Fig. 26 depicts the dilution of the WR spectrum and its emission lines. The total continuum in the red is up to twice as strong as for the WR alone, meaning the emission lines from the WR are diluted by a factor of 2. This corresponds nicely with the overprediction by the model spectra. If one additionally assumes that the observed continuum is shaped by several RSG and red giants, also an overprediction by a factor > 4 can be explained. The lower panel in Fig. 26 also suggests that the dilution increases with wavelength. Again, this is confirmed by the fitting process (see e.g. the spectral fits of WR 7 and 13).

How about the spectral visibility of the late type star contamination in our data. As already stated that

[19] They actually refer to the fluxes received from an object with 1 m^2, 500 m^2, and 1000 m^2 surface area at the given temperatures, respectively

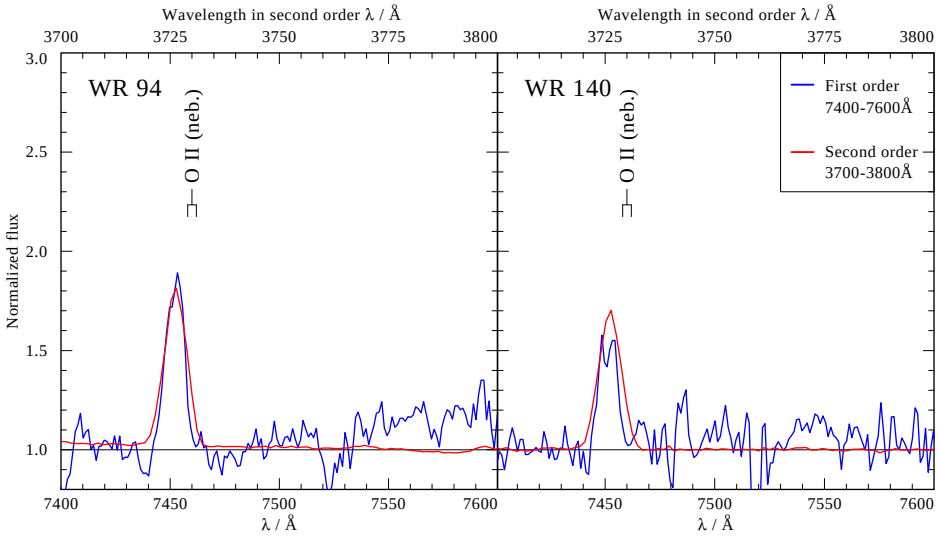

Figure 25: *Normalized spectra of M31 WR 94 (left) and M31 WR 140 (right) in the red (blue solid lines), overlayed each by the spectrum of the same star where the wavelength is multiplied with 2 to illustrate the light from the second order (solid red lines) and which was diluted by factors of 10 and 50 for 94 and 140, respectively*

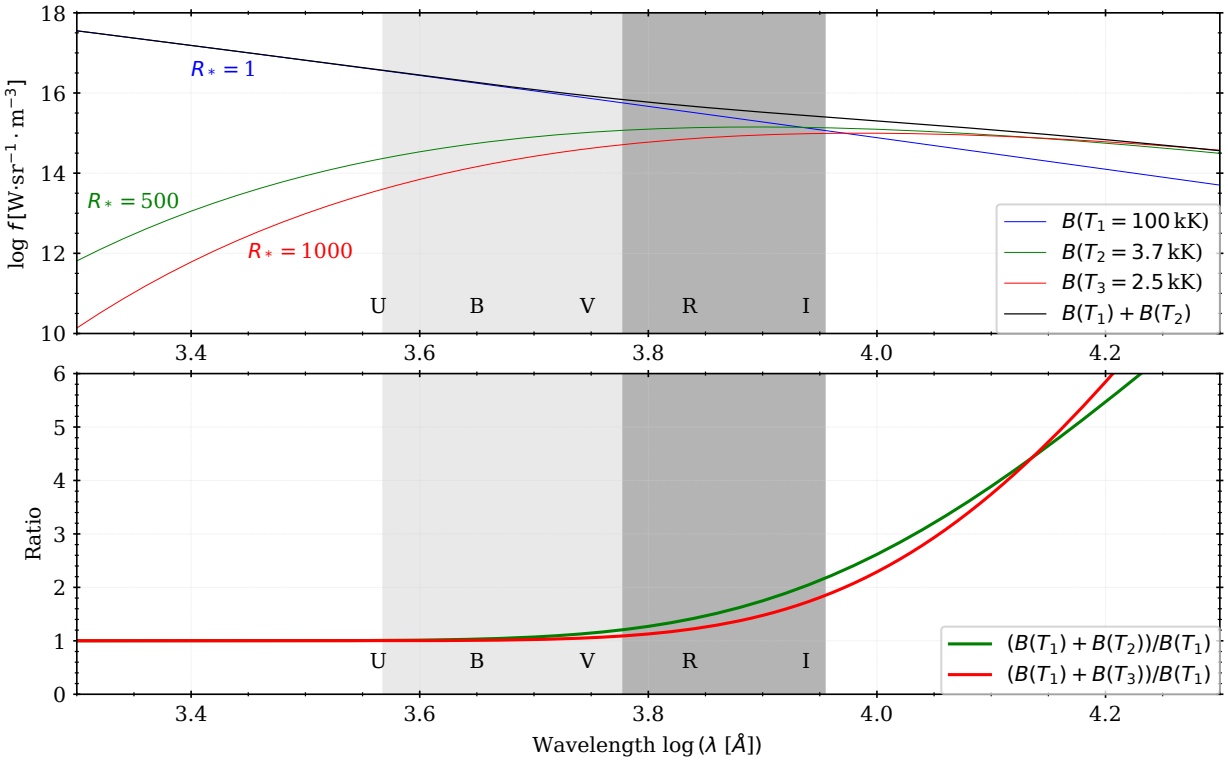

Figure 26: *The impact of light contamination by a cool star*
Upper panel: *Black body spectra calculated for three hypothetical stars as approximation of their SEDs. The WR is represented by the blue solid line which marks the black body curve of a star with $T_* = 100\,kK$. Two SED's of RSG are also shown for $T_* = 3.7\,kK$ and $T_* = 2.5\,kK$ (green and red solid line, respectively). The radii are normalized to the radius of the WR star. The black solid curve shows a combined SED, consisting of the WR and the hotter RSG (blue + green curve). The gray shaded areas denote the spectral range used in this study, with the darker shaded area marking the region where the overpredicted red lines can be found. Also the central wavelengths of the UBVRI filter curves are indicated.*
Lower panel: *Ratio between the continuum fluxes of the combined SEDs of WR+RSG each and the SED of the WR star to estimate the dilution caused by the additional continuum flux.*

the S/N decreases for most spectra towards the red. But if we take a look on the spectrum of a star whose photometry indicates an increasing flux in the I and have a high S/N, we do actually find signs of spectral contamination (cf. SED of WR 94 below and the red part of the spectrum in Fig. 24)

The question is at which point this dilution starts to be negligible? The lower panel in Fig. 26 indicates a decline of the dilution to a negligible level around 5000 – 6000 Å. But the truth will look different for each individual star and its neighborhood. A detailed analysis might be possible with the help of the HLA images

and the extracted photometry combined with a fit to the line overprediction of the model in comparison to the observation. But that would be far beyond the scope of this study and we therefore go with a simpler approach. We assume that all spectra are not diluted up to C IV λ5808. All lines redder than this are assumed to be diluted to a certain extend and the difference between model and the observation will be noted for the individual stars. The lines in the red part of the spectrum are therefore excluded from the modeling process.

7.2.7 Chemical composition

The chemical composition of a WC is dominated by helium and carbon. Those two elements usually make up more than 90 % of the material of the WC wind. Naturally, the central regions of the WC star will look differently but their chemical composition can not be determined spectroscopically. The ratio of carbon to helium will tell something about the evolutionary state of the star as the star enriches itself continuously while evolving further. As already demonstrated in Sect. 7.2.1, the diagnostic pair is a good indicator for the carbon to helium ratio (cf. Fig. 17). The findings based on this line generally agree nicely with what can be seen in the entire spectrum, with the exception of some peculiarities discussed in Sect. 7.8.

The next important element for a WC star is oxygen. In Sect. 7.2.5, we have already discussed the problems of the model spectra with reproducing the observed line strengths. As we cannot overcome this issue, we will use O V $\lambda\lambda 5336-5519$ as indicator for the oxygen abundance if a consistent fit for the entire spectrum is achieved. This will generally lead to an overprediction of O IV λ3934, and O III λ3961 while O VI $\lambda\lambda 3811, 3834$ is not reproduced by the model. In rare cases, there is agreement in the model for O IV λ3934, O III λ3961, and O V $\lambda\lambda 5336-5519$, but O VI $\lambda\lambda 3811, 3834$ is never reproduced at all.

For a handful of WC stars of the sample, nitrogen is also important, see Sect. 7.2.3. The number of nitrogen lines is limited and only allow a rough estimation of the nitrogen abundance. Depending on the individual star, visible are N IV λ4057, N III $\lambda\lambda 4103, 97$, and N IV $\lambda\lambda 7103-29$. In Fig. 27, we depict the important parts of the spectrum for the determination of the nitrogen abundance in two stars that show nitrogen features. Note that the middle panels are shown only to illustrate the evolutionary consistency with the reduced amount of carbon. With the inclusion of nitrogen in the model calculations for the relevant stars, something interesting can be observed. It seems to be impossible to fit N IV λ4057 and N IV $\lambda\lambda 7103-29$ simultaneously, while latter is consistent with N III $\lambda\lambda 4103, 97$. N IV λ4057 is overpredicted by the models. This is in so far peculiar as we have discussed in Sect. 7.2.6 a possible dilution for the red lines. If the model reproduces the line strengths correctly, N IV λ4057 is well reproduced and N IV $\lambda\lambda 7103-29$ should be overpredicted. But the exact opposite is observed. This behavior of the lines is already known and its origin unclear. For the determination of the nitrogen abundance, we use N IV $\lambda\lambda 7103-29$. For some stars, the nitrogen abundance is difficult to estimate, e.g. for WR 15 (cf. Fig 27). The nitrogen lines in the blue are hidden in the line blend around 4100 Å and the spectrum in the red shows clear signs of dilution. The actual line strength of N IV $\lambda\lambda 7103-29$ is therefore not known. We still fit the nitrogen abundance to match N IV $\lambda\lambda 7103-29$ but the derived value is only a upper limit.

We already noted in Sect. 7.2.3 that the inclusion of silicon to the models leads to an improvement in the fit. But Si IV $\lambda\lambda 4088, 4116$ remains the only silicon feature observable in the spectrum. Therefore, it is the only way to estimate the silicon abundance of the stars. Unfortunately, as already stated in Sect. 7.2.3, the blend around 4100 Å is even with the inclusion of silicon only partly reproduced due to some unknown line feature that contributes to it. The models underestimate the blend usually. It is not entirely clear for most of the stars how much Si IV $\lambda\lambda 4088, 4116$ and the unknown line contribute to the blend each. We decide to fit the silicon abundance such that the observation is reproduced best. The derived silicon abundance has to be considered therefore generally as an upper limit.

The last elements included into the calculations are the iron group elements which are calculated together in the superlevel approach as generic element G. Those include scandium, vanadium, titan, nickel, cobalt, chromium, manganese, and iron. No iron lines can be observed in the optical. A determination of the iron abundance is therefore not possible and all models are assumed to have solar iron metalicity. Note that a change in iron abundance can have an effect on other lines. A testwise doubling of the iron abundance brought a significant increase in the emission of C IV λ5808 and the Bowen blend.

As the inclusion of further elements does not bring any significant change to the model spectra (cf. Sect. 7.2.3), abundances for other elements can not be determined.

7.2.8 Terminal velocity

The terminal velocity v_∞ is an important parameter to evaluate the strength of the stellar wind. For OB stars, it is determined from the absorption part of P-Cygni profiles in the UV. In principle, this is also possible for WR stars with thin winds. But as we only have optical data, we have to estimate v_∞ in a

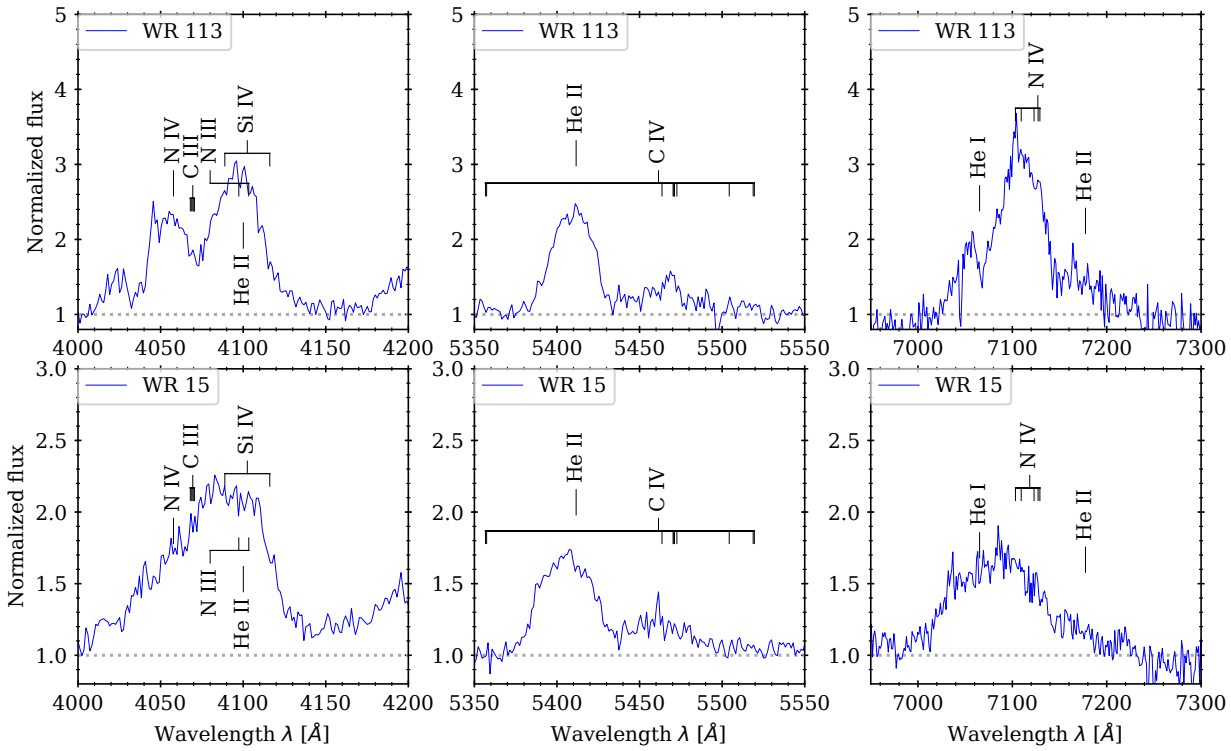

Figure 27: *Nitrogen abundance determination. Shown are the observed spectra (solid blue lines) of WR 113 (upper) and 15 (lower)*

different way from the emission lines. The emission seen in the emission lines in the optical originates from the outer regions of the star and therefore the linewidth of those lines can tell about v_∞. But this is not an independent measurement. The linewidth is further determined by turbulences in the wind, the temperature distribution in the wind, and the wind velocity field. Those are all generally small factors for the line shape compared to the terminal wind velocity but need to be accounted for. To eliminate one free parameter, we keep the velocity law parameter β constant as $\beta = 1.0$. We determine the wind velocity by adjusting v_∞ such that the line profile of the prominent emissions lines are reproduced. The impact of different terminal velocities on the line shape is illustrated in Fig. 28. Especially C III λ5969, if present in the spectrum, proves to be a good indicator due to its box like shape and therefore steep line wings. The weaker lines are generally not used for this estimation but show usually consistency with our findings for the strong lines. The reason why those lines are not used in the first place for the estimation is that they are impacted by rotation of the star much stronger than the prominent lines. This might lead to different estimations of v_∞.

7.2.9 Rotational Velocity

The stellar rotation can have a significant impact on stellar evolution (mixing). Furthermore, a high rotational velocity alternate a star from spherical symmetry and may cause decretion disks (cf. Be stars, e.g. Porter & Rivinius 2003). Therefore, an estimation of the rotation of the star is important. Unfortunately, the estimation of the rotation is rather imprecise and highly biased by the angle under which we see the star. The bias is a problem existing for all stars. The rotation is determined from the broadening of emission lines (Abney 1877). Two problems are obvious in this way of estimation:

1. To measure the actual rotational velocity, it is required to observe the star edge on. However, we cannot choose the angle under which we observe a star for obvious reasons and it is generally impossible to estimate which inclination i the rotation axes of the star has towards us. Every velocity estimated needs to be considered as only the projected velocity and the actual rotation might be (much) faster. Therefore, the usual way to give a measured rotational velocity is as the projected $v'_{\rm rot}$ by

$$v'_{\rm rot} = v_{\rm rot} \sin i$$

2. The estimation of the rotation for WR stars is rather imprecise. A simple estimation of the line broadening is problematic due to various other effects, as the stellar wind expansion velocity, broadening

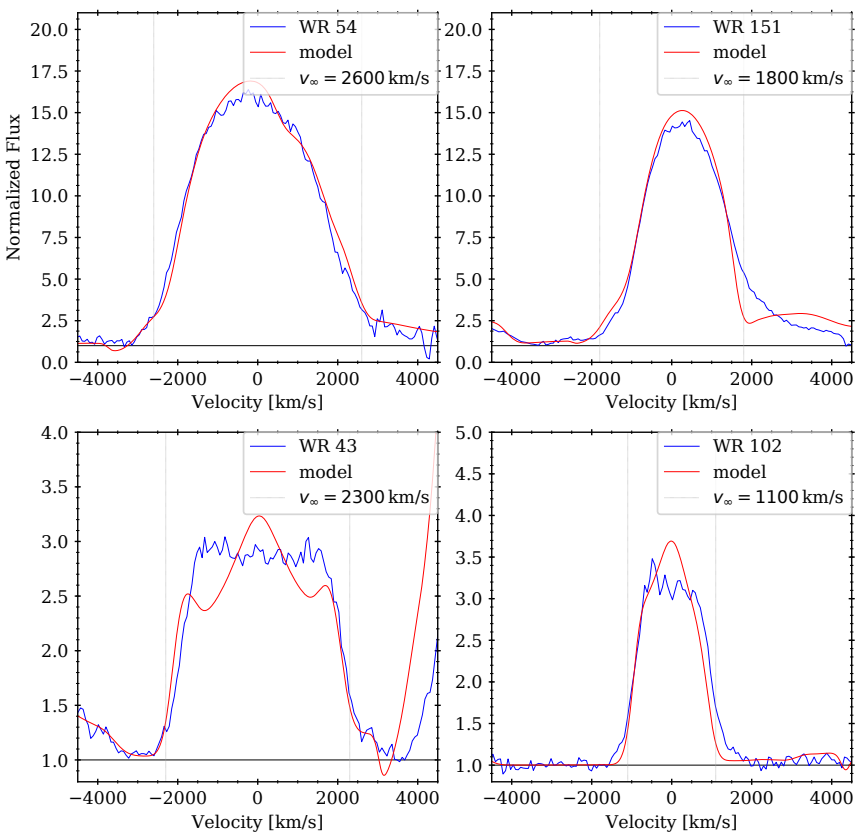

Figure 28: *Comparison of the observed line profiles of* C IV *λ*5808 *in the spectra of WR 54, 151, and* C III *λ*5969 *in WR 43, and 102 (solid blue lines) in velocity space with* $v = 0\,km\,s^{-1}$ *referring to* $\lambda = 5808\,Å$ *and* $\lambda = 5696\,Å$*, respectively. The terminal velocity for the individual stars is indicated by the vertical gray lines.*

due to temperature and pressure that influence the observed lines shapes. In principle, those effects are already accounted for by modeling process, but uncertainties still remain.

3. Different wind lines are affected differently

The standard procedure utilizes that the line shape of a rotationally broadened line can be reproduced with a convolution of the line profile with a semi ellipse whose width corresponds to $v \sin i$. However, this method does not work for a WR star as the spectrum is not formed in a thin layer at the stellar surface. We will determine the rotational velocity by applying rotational field for the expanding wind as described in Sect. 6 consisting of a linear increase up to the co-rotation radius $R_{\rm corot}$ and decreases outwards under the assumption of angular momentum conservation (for more details, see Shenar et al. 2014). $v_{\rm rot}$ always describes the rotational velocity at $R_{\rm corot}$. Due to this radial dependency, lines forming in different layers of the wind, experience different line broadening. This effect can be seen easily when comparing the diagnostic pair to C IV 5808. Both lines originate from C IV, but in different layers which causes C IV 5808 to be barely effected even by strong rotations while the diagnostic pair shows a strongly broadened line profiles. In Fig. 29, this effect is illustrated for a selection of lines indicating the different effect of rotation and showing the difference when assuming a co-rotating wind.

We will eventually find a surprisingly high rotational velocity for about half the stars which exceeds their critical rotation. This means those stars should rotate fast enough to disintegrate themselves. As do we see the stars this has obviously not happened yet. We will investigate this issue and possible solutions further in Sect. 9.4. For now, we adopt the rotational velocities as we determined them here, since the present analysis reveals striking agreement between the observation and our models that adopt the above mentioned formalism for rotation.

Other methods to derive the stellar rotation (e.g. periodicity in light curves) have their own (dis)advantages (see, e.g. Bouvier 2013) but those are also not available to us here.

7.3 A key parameter - the luminosity

A main motivation for this work is to obtain stellar parameters for a sample of WC stars with known distances and about solar metalicity. A keystone to reach this goal is to estimate the stellar luminosity. In the ideal case, one would use space based flux calibrated spectra to determine the spectral energy distribution (SED) of a star. As we do not have such observations, we use photometry. Photometric measurements correspond

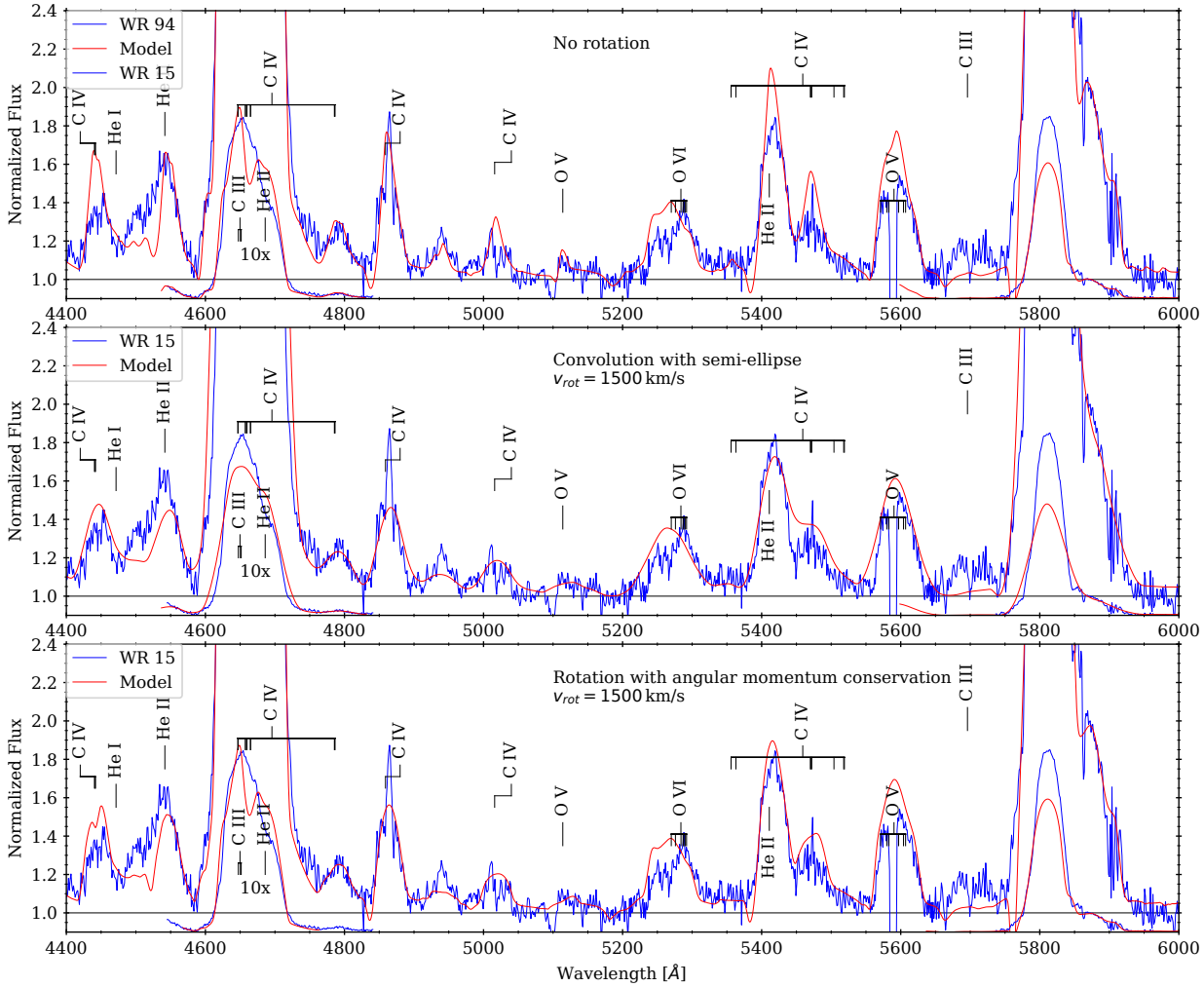

Figure 29: *Line broadening due to stellar rotation. Comparison between the observed spectrum of WR 15 (solid blue line) and the best fitting model (solid red line). In the upper panel, no rotational broadening is applied to the model. The central panel simulates rotation broadening with a convolution with a semi-ellipse and* $v_{rot} = 1500\,\mathrm{km\,s^{-1}}$. *The lower panel uses the line broadening as described in Shenar et al. (2014) with a co-rotating part and angular momentum conserving part of the wind.*

to a certain flux at a filter dependent wavelength. Those fluxes can then be compared to the model SED. The flux of the synthetic SEDs is reduced accordingly to the geometrical dilution due to the distance of the analyzed star and interstellar extinction along the line of sight.

Geometrical dilution goes quadratic with the distance, $F \propto \frac{1}{d^2}$. The distance to all our stars is assumed to be the same (770 kpc, see Sect. 3.2). The division with d^2 corresponds to subtraction on a logarithmic scale of $0.4 \times \mu$ with μ being the distance modulus, given as

$$\mu = 5 \log_{10}\left(\frac{d}{[\mathrm{pc}]}\right) - 5 = 5 \log_{10}\left(\frac{d}{10\,\mathrm{pc}}\right)$$

and we scale the model flux as

$$F'(\lambda) = F(\lambda) - 0.4\mu.$$

This step is done for each individual star.

Differences between the stars are found for the reddening. The absorption and scattering by the interstellar matter (ISM) reddens the SED and reduces the overall flux. An observation of stars in M 31 is not much influenced by the ISM in the MW. The foreground reddening is almost negligible since we look perpendicular to the disk. A larger impact is from the local interstellar medium in M 31. We observe a different degree of reddening for the individual stars. To account for this reddening, we again subtract a certain flux from our synthetic SED. This time, the amount is wavelength dependent. This dependency can have different shapes, depending on the composition of the interstellar gas and dust. We can adopt various empirically found reddening laws, such as Seaton (1979), which for the optical range adopts the results of

Nandy et al. (1975), as well as Cardelli et al. (1989), or Fitzpatrick (1999). Those differ in the UV, but in the optical the extinction is similar. We adopt Seaton (1979)/Nandy et al. (1975) for all stars. The ratio of total to selective extinction is hereby fixed at $R_V = 3.2$. The color excess E_{B-V} is determined for each star by fitting the synthetic SED to the observed photometry. Figure 30 illustrates this process for WR 54.

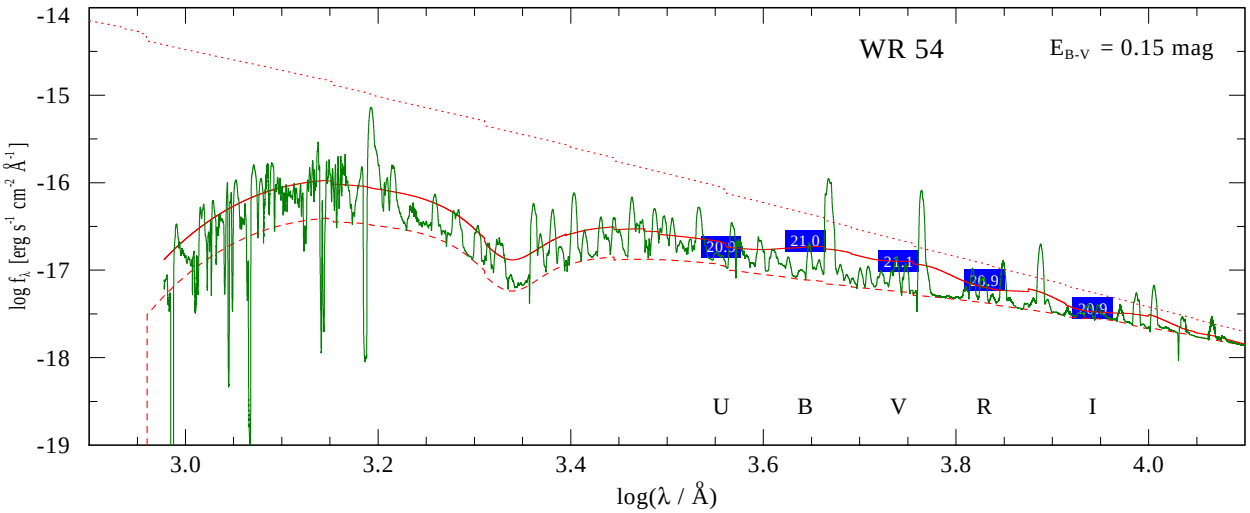

Figure 30: *The diluted synthetic SEDs without lines with reddening (red dashed line) and without (red dotted line) compared to the photometry of WR 54 (blue boxes). The reddened SED including the spectral lines is also shown (green solid line). Furthermore, the reddened SED with the same line spectrum is shown. This time it is convoluted with a Gaussian (FWHM = 1000) to approximately illustrate the impact of the strong lines on the measured photometry in the UBVRI broad band filters (red solid line).*

We derive the luminosity of a stars now in the following way: we take the known distance, which dilutes the entire spectrum accordingly, fit the slope of the synthetic SED to the photometry by adjusting E_{B-V}, and set the luminosity in a way to reproduce the absolute fluxes.

For OB stars, the process would be done here. But for a WC we need to account for something more. Due to the nature of WC stars, the real continuum flux is not always visible anymore. The UV line emission completely outshine the continuum, it becomes invisible. However, we don't have UV photometry. But also in the optical the spectral lines cause problems. There are not so many of them, but the prominent lines mentioned above contribute significantly to the observed flux in the broad band *UBVRI* filters. As we can see in Fig. 30, the B magnitude will be impacted by strong He II λ4686 emission and V and R are impacted by C IV λ5808. If those emission lines are strong, *BVR* will indicate a higher flux, only U and I show the continuum.

7.4 Photometry: HST vs. LGGS

The luminosity is determined as described above. Naturally it depends on the accuracy of the obtained photometry. The LGG-Survey was a ground based mission and therefore affected by the seeing conditions. Massey et al. (2006) showed that despite of the seeing conditions, the data reduction was able to identify most of the stars as multiple in the ground based survey as was seen at HST resolution (cf. Fig. 3 of Massey et al. 2006). However, not all stars were identified correctly. Also the worse spatial resolution can impact the obtained photometry. To evaluate the quality of the LGGS data, we compare the measurements with actual HLA photometry for three different of our *sample* stars in Fig. 31. These stars were selected such that they are covered by multiple HST images, covering the UV, optical and NIR regimes. WR 23 acts as a benchmark as it is widely isolated from possible contaminating sources. WR 94 is of interest as it is located in a H II region and the star seems to have created a wind blown bubble around itself. WR 124 is located in proximity of other stars that might influence the obtained photometry. As can be seen in Fig. 31, the photometry of HLA and LGGS are in good agreement. Therefore, we assume all LGGS photometry to be accurate and appropriate for a determination of the stellar luminosities. The extracted photometry for the individual stars from the HST images is listed in Table 8.

7.5 The spectral degeneracy

Fitting WC spectra is difficult. But not only some lines avoid being fitted at the same time. There is also a degeneracy among the spectral appearance for different parameters. Stars with very dense winds, namely

Table 8: *HLA photometry for the three* sample *stars WR 23, 94, and 134. Note that some stars were covered by images with the same filter several times in different surveys or as they are located in overlapping regions between the images in one survey and that the extracted photometry varies by up to 0.3 mag between those images. For this quick comparison no further effort was taken and just simply one image selected each. Most stars only have* DAOPHOT *photometry listed and if* DAOPHOT *and* SExtractor *were available, the former was used.*

Filter	WR 23	WR 94	WR 134
F170W	19.93	18.71	-
F220W	-	-	-
F255W	20.47	19.15	-
F275W	-	19.39	20.70
F336W	20.50	19.81	20.69
F439W	20.26	-	-
F475W	-	19.42	20.45
F555W	20.54	-	-
F606W	-	-	20.54
F775W	-	-	20.72
F814W	20.98	20.38	20.76
F110W	-	19.90	20.70
F160W	-	19.90	21.41

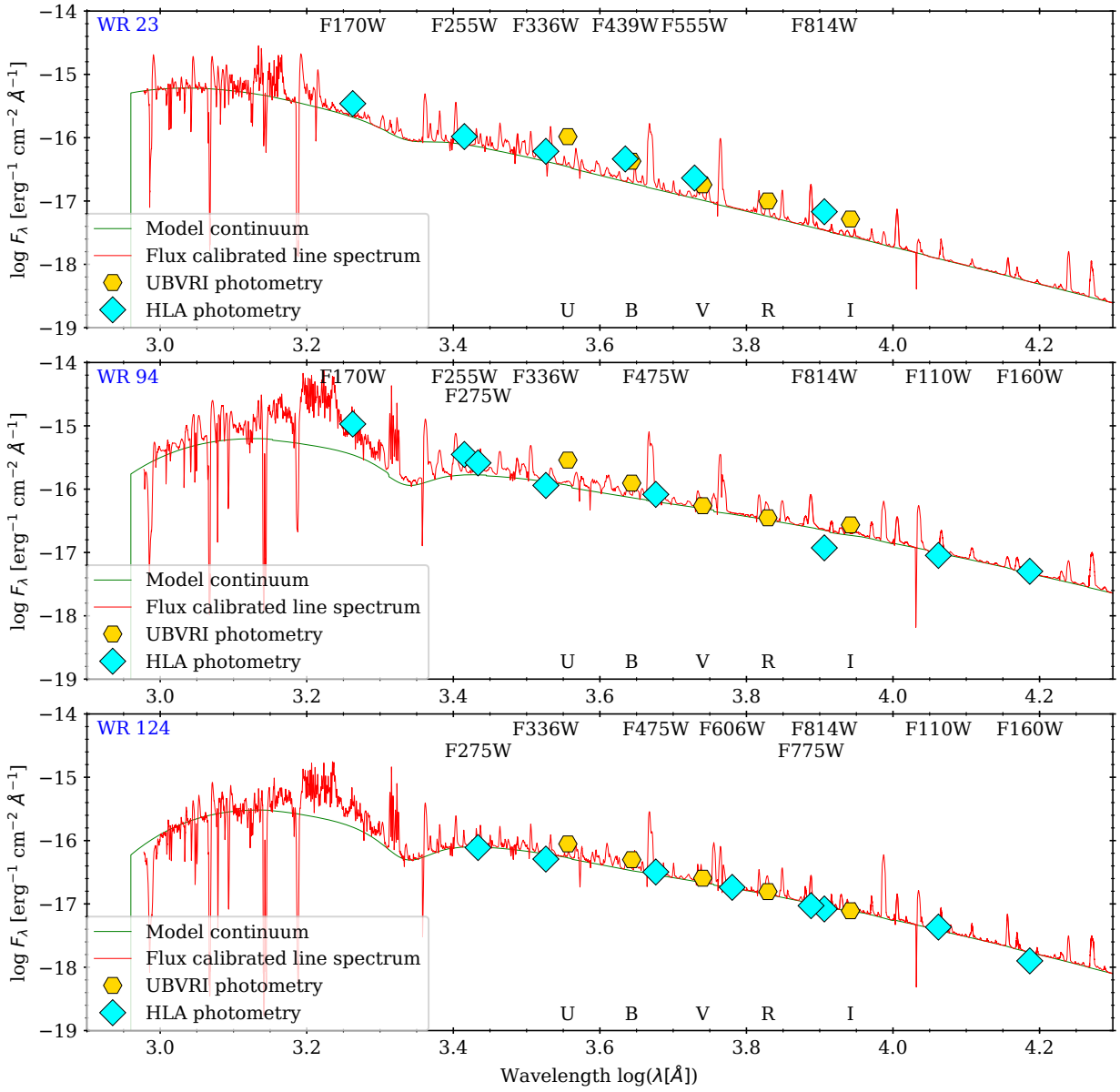

Figure 31: *A comparison of the synthetic SED of WR 23, 94, and 124 (from top to bottom panel) to photometry from LGGS and extracted from HLA data. The solid green curves indicated the stellar continuum flux without lines, and the red solid lines with spectral lines. The photometry is displayed as blue diamond (HLA) and yellow hexagons (LGGS) with the corresponding filters indicated.*

with $\log R_t/R_\odot < 0.4$, show spectra whose appearance does not depend on the two individual parameter T_* and R_t anymore, but only on the product $T_* R_t$. This is caused by the fact, that those thick winds block the light from slow moving wind layers and only the fast ones are visible. The details have been presented by Hamann et al. (2003). The consequence is that stars on the same grid diagonal and with $\log R_t/R_\odot < 0.4$ might be indistinguishable Fig. 15 for the affected parameter space.

How is the present work affected by this problem? As already stated, the degeneracy occurs for very dense models. Further a quick overview for the prominent lines revealed that only a narrow region in the parameter space is appropriate for reproducing WC stars. This narrow region is almost parallel to the grid diagonals. This means the affected stars are those with thick winds and high temperatures. Presumably WC4 and WC5 stars. Cooler stars are less affected by this. Furthermore, we have seen that the evolution of the lines across the model grid (cf Sect. 7.2.2) is different for the prominent lines even in the region of dense winds. Those differences are not strong but noticeable. This fact might help us to overcome the problem with this approximate degeneracy.

The way to do so is to find the right diagonal for an individual star. This means that temperature and mass loss are balanced such, that e.g. C III λ5696 is reproduced well. Now the model is shifted along a grid such that the line strength of C III λ5696 stays constant and the evolution of other spectral lines indicate the best parameter range. It can be seen that the line to shift along given by, e.g. C III λ5696, in the $\mathcal{R}$–$\mathcal{T}$ plane is not necessarily parallel to the grid diagonals and the fitting processes is carried out accordingly. This process is done for each star individually until the best fitting model is found.

7.6 The deficiencies of the spectral classification system for WC stars

The problems for the spectral classification arising from the way a WC spectrum forms were mentioned already. Now we want to have a look on it the other way round. The spectral type of a star should, in principle, tell us already something about the star itself, its parameters, and its evolutionary state. The idea is that the earlier types are the hotter stars. And when we look at evolutionary models, hotter star usually means further developed. Let's dive into parts of the present data. We will show that this assumptions can not be uphold. In Fig. 32, the spectra of all six WC 4 stars are shown. Two of them are identified as clearly diluted (M 31 WR 3 and M 31 WR 61). The other spectra (M 31 WR 12, 15, 23, 54) are free of contamination. After a look on Fig 32, this might seems surprising, since C IV λ5808 shows the same line strength in M 31 WR 15, 23, and 61. But a closer look reveals, M 31 WR 61 resembles the spectrum of M 31 WR 54, just diluted by a factor of ≈ 2.5. Also the line shapes are similar. M 31 WR 61 and 54 are similar stars. The spectrum of one is just diluted. WR 12 shows a very strong He II λ4686. The only other comparable star is again M 31 WR 54. But for C IV λ5808, M 31 WR 12 is much weaker. Still those stars are classified WC 4 as both don't show C III λ5696 which is used for the classification. That this is not a dilution effect can be seen from the weaker lines, shown in the lower plots of Fig. 32.

Another M 31 WC4 star is M 31 WR 23. Judging from C IV λ5808 and He II λ4686, this star again appears to resemble a diluted M 31 WR 54. But in contrast to M 31 WR 61, the weak lines here do not show any sign of dilution.

M 31 WR 15 is a WC 4 star that shows clear signs of nitrogen and a strongly reduced amount of carbon. This star has to be in an early evolutionary state. Still, its classification is solid. Also its line strengths resemble M 31 WR 23, only the line shape is different.

We have seen now that stars with the same spectral classification show largely different spectral appearance in the strongest spectral lines, there are large deviations in the chemical composition, indicating different evolutionary states, and the model fits will also show, that the stellar parameters of those stars differ widely. All of this deprives the spectral type of a WC star the role of an indicator for the stellar parameters and the evolutionary state.

Earlier analyses of Galactic WC stars found a clear correlation between spectral type and stellar parameters, see Barniske et al. (2006) (their Fig. 2), and Sander et al. (2012) (Figs. 6 and 7). How can we bring this into agreement with what we have seen now? Spectral fits of WC stars are considered problematic. Various lines cannot be reproduced nicely by models. Especially the strongest lines in a WC spectrum suffer from this shortfall. Figure 3 of Sander et al. (2012) shows the spectral fit of a WC 6 star. Neither He II 4686, nor C IV λ5808 could be reproduced satisfyingly. Both lines are off by a factor of 2. On the other hand, C III λ5696 is fitted nicely. But in consequence this deviation can mean that the model spectrum and the observed spectrum are not assigned to the same subtype. A good example is the spectral fit of WR 017 in Sander et al. (2012). The star is classified as WC5. The spectral fit shows that the C III λ5696 is overpredicted by a factor of two, and C IV λ5808 is underpredicting by a factor of two. When looking Table 2, we can see that the ratio between those two lines is used as the main indicator for the classification. If it is off between model and observation by a factor of 4 (≈ 0.6 dex), model and observations are most likely classified in different

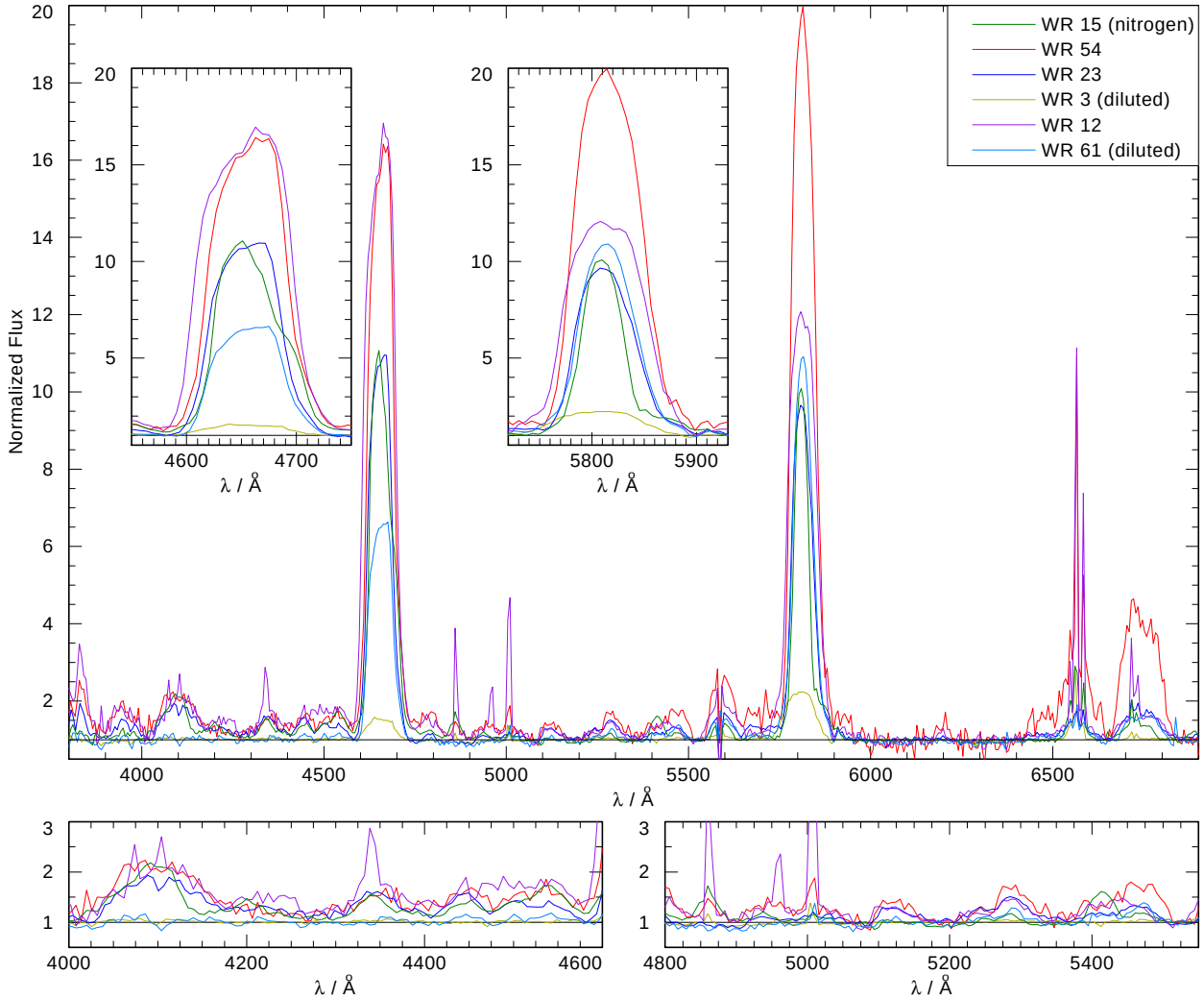

Figure 32: *Spectra of all WC4 in M 31 for comparison: WR 3 (diluted, solid yellow line), WR 15 (with nitrogen, solid green line), M 31 WR 23 (solid blue line), WR 54 (solid red line), WR 61 (diluted, light blue line), and WR 12 (solid purple line). The entire spectral range is shown, with additional zooms on specific regions.*

ways. In this case the star is a WC5, while the model would be classified as WC6. A fact that undermines all attempts of a reliable correlation between the stellar parameter and its classification.

7.7 The late type WC stars

We have seen now that there are some issues for the spectral classification and its predictions for the nature of an individual star classified in a certain way. The same analysis of the WC4 spectra as we have done in Sect. 7.6 can be done for WC5 as well with the same outcome. However, this changes if we go to the later types. The stellar spectra for each individual subtypes get much more consistent among the same type.

One motivation to have a closer look on the spectral classes again in such detail is the lack of analyzable late type WCs. The sample contains only 4 WC8 spectra and no WC9. From the WC8, only M 31 WR 56 was not identified as clearly contaminated but it is suspicious. The latest type of star which is not suspicious of contamination is M 31 WR 102, the only WC7-8 in the sample. The spectra of all those stars are shown in Fig. 33.

The differences between the individual stars is much smaller than it was seen in Fig 32. The main difference is the strength of the emission lines, but the shape is similar for all stars in the sample. The spectra of M 31 WR 49 and 80 are almost identical and WR 136 resembles their spectra only diluted by a factor of 2. The lines of WR 56 are stronger then of those mentioned and the overall spectra resembles much more the one of WR 102.

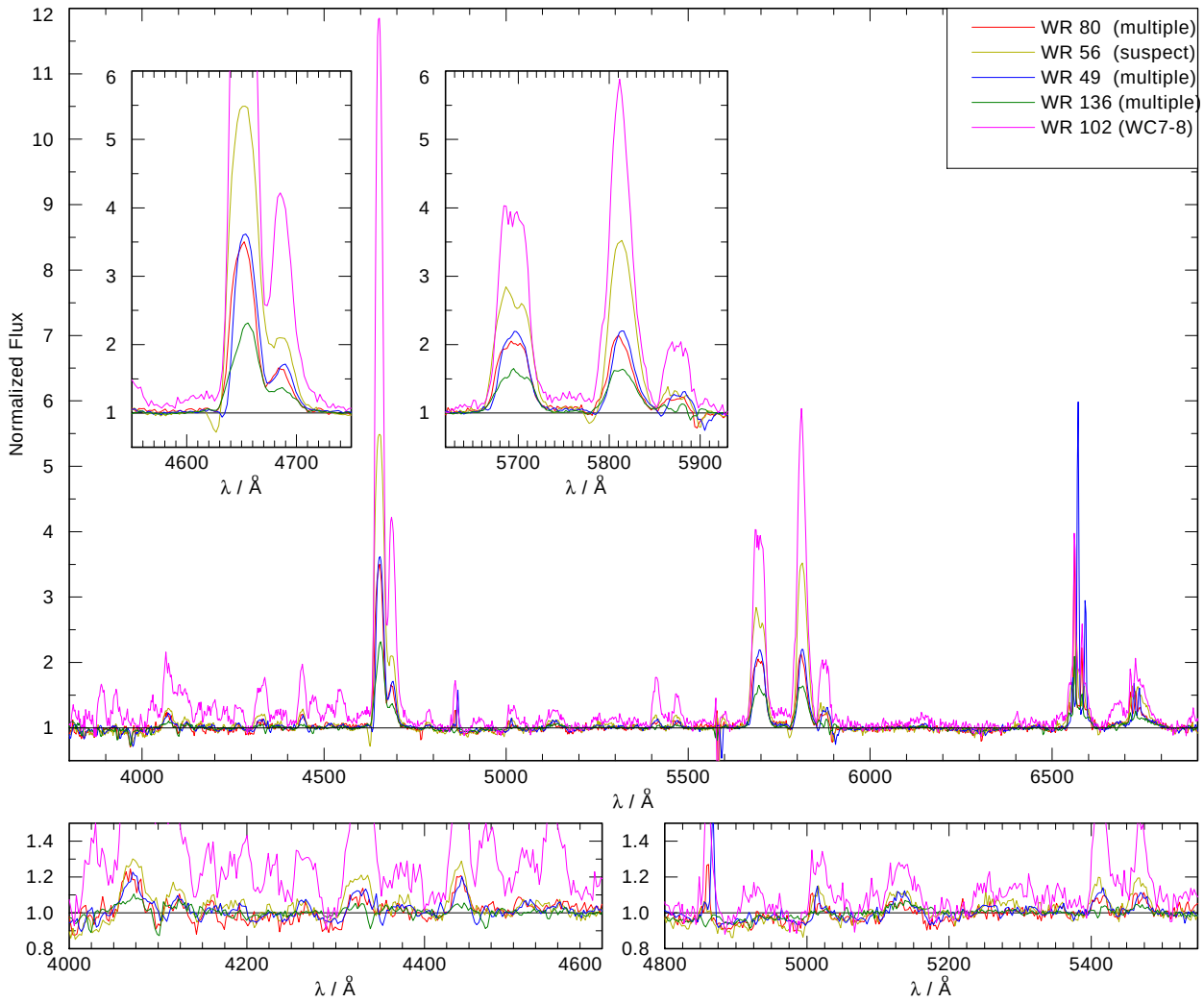

Figure 33: *Spectra of all WC8 and WC7-8 in M 31 for comparison: M 31 WR 49 (diluted, solid blue line), M 31 WR 56 (solid yellow line), M 31 WR 80 (solid red line), WR 54 (solid red line), WR 136 (diluted, solid green line), and WR 102 (WC7-8, solid pink line). The entire spectral range is shown, with additional zooms on specific regions.*

7.8 Fitting issues and peculiarities

Although for most of the sample stars, a decent spectral fit could be achieved, various problems could not be solved in the process. In this section we want to investigate those line features more in detail.

7.8.1 General problems

Next to the already mentioned issues with the oxygen lines, there are various weaker lines which could not be reproduced satisfyingly for a large fraction of the sample.

Overpredicting C IV λ4451, underpredicting H II λ4339: The lines located blue wards of He II λ4686 suffer on issues in a large fraction of the sample stars. One important deviation seems to contradict the estimated carbon abundance. While the diagnostic pair is reproduced fairly well, C IV λ4451 and H II λ4339 indicate a much lower carbon abundance. H II λ4339 is underestimated by the model calculations while C IV λ4451 is overpredicted (cf. Fig. 34). In fact, in a model with strongly reduced carbon abundance, like we used for M 31 WR 113, those two lines are reproduced nicely. If we adjust the abundance in a way that this *pseudo-diagnostic pair* is reproduced, the spectra gets inconsistent all over. Except for those cases in which the real diagnostic pair also indicates a strongly reduced carbon abundance. An increased carbon abundance indicated by the diagnostic pair is also not seen in its *pseudo* counterpart. Therefore, we adjust the carbon abundance according to the diagnostic pair and the overall spectrum and ignore the mismatch for C IV λ4451 and H II λ4339. A way to partially overcome the strongly overestimated C IV λ4451 is the inclusion of rotational broadening. This line is strongly affected. In fact, for high velocities this line split into sublines, a development that is not an artifact of the calculation but actually supported by the observations (cf. WR 94 in Fig. 34). There is

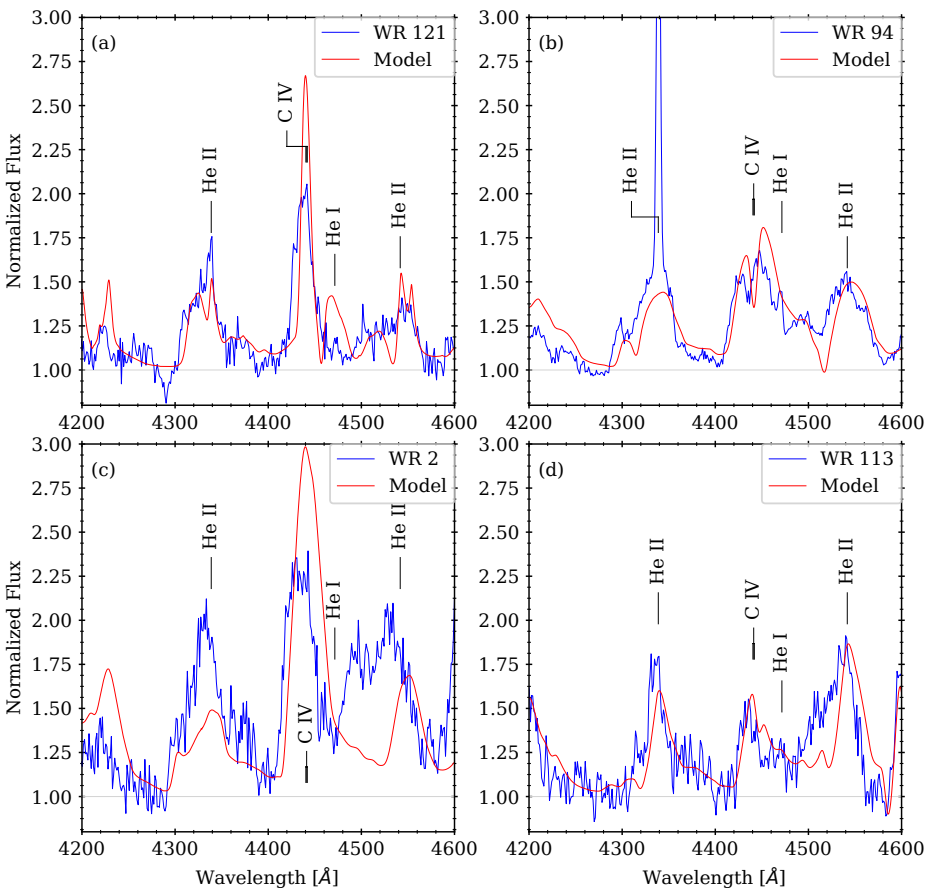

Figure 34: *Spectral cutouts for M 31 WR 121, 94, 2, and 113. Shown are lines that turn out to be difficult to reproduce for most of the sample stars, i.e. WR 2 and 121. WR 113 has a strongly reduced carbon abundance and WR 94 is a fast rotator. The observation is shown as solid blue line and the best fitting model spectrum as solid red line.*

no strong effect on H II λ4339. The helium line is part of the Pickering series ($10 \rightarrow 4$). A comparison to the neighboring lines of that series reveals that their line strength follow the expected decline towards bluer wavelength. Moreover, $9 \rightarrow 4$ (4541 Å) and $11 \rightarrow 4$ (4200 Å) reveal nice agreement between model and observation. By inversion of argument one can say that the observed emission profile has to be shaped by more than just helium. However, the inclusion of other elements in the calculation did not brought any advancement in this regard.

Flat top C III λ5690: The emission lines in the emergent spectrum created by PoWR show for certain lines a shape which is not observed in reality. For a single line, the emission lines appears to have three individual peaks, one at the actual wavelength of the line, the two others blue- and redwards shifted in dependence of v_∞. Those affectionately called *church steeples* are most prominent for C III λ5690. and are shown exemplarily in Fig. 35. The observation shows for this line instead a very peculiar

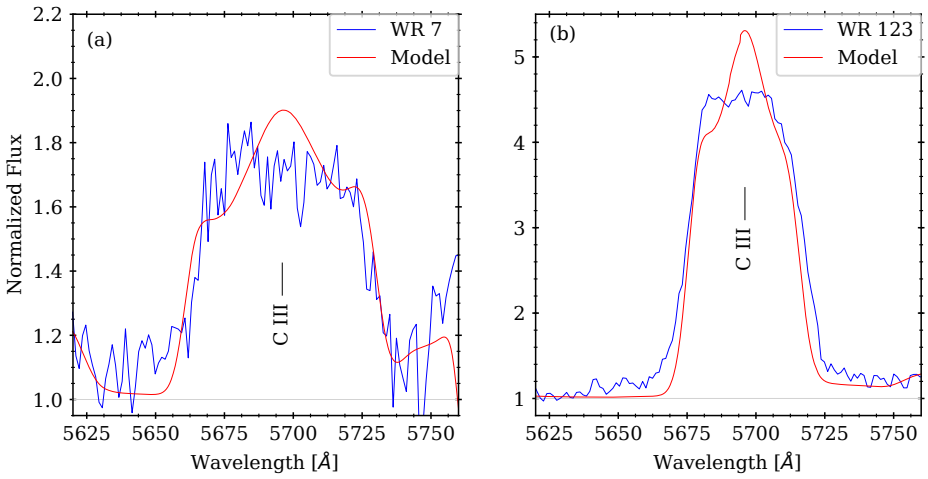

Figure 35: *Church steeple and flat top line shapes for* C III λ5690. *The blue solid lines show the observed spectra for WR 7 and 123, and the red solid lines a model for comparison each. The flat top shape is clearly visible even for spectra with low S/N. Note that for some stars (like WR 7) this flat top seems to be mildly tilted.*

shape. The line seems to have a box like shape with a very flat top. No parameter set explored in the

models calculations could reproduce a similar shape. Only a test case were the rotational velocity was increased to $v_{\rm rot} \sin i = 10000\,{\rm km\,s^{-1}}$ altered the synthetic line in a way that the observed line shape are nearly reproduced, but this situation is highly unphysical and was also inconsistent for the rest of the spectrum.

7.8.2 Unusual line shapes

Throughout this analysis and the investigation of the spectra, some of the spectra turned out to be rather peculiar inhibiting very unusual line shapes. Those were also generally not reproducible by the modeling process but affected only a few stars.

Double Peak He II λ4686: The Bowen blend is a complex line structure as it is composed of emission lines of C III, C IV, and He II. Therefore, its appearance at different stellar parameter is barely predictable due to interplay between the lines. E.g. C III $\lambda4646-4665$ and C III $\lambda5690$ react sometimes similar sometimes entirely different to parameter changes. Generally, two overall line shapes seem to be present for most of the stars. The first one (WR 2 in Fig. 36(d)) is dominated by C III and shows a rather narrow, spike like shape. The red wing is given by He II λ4686. C IV is not prominent here. For slower winds and thinner winds, this also can develop to a point where C III and He II are seen more or less separated from each other (cf. M 31 WR 123). For hotter and denser atmospheres, C IV dominates the line, giving it a more box like shape (cf. WR 12 Fig. 36(e)). Those two shapes are observed for the majority of the stars (see Fig. 36) However, not all stars show those line shapes. In Fig. 36(a-c),

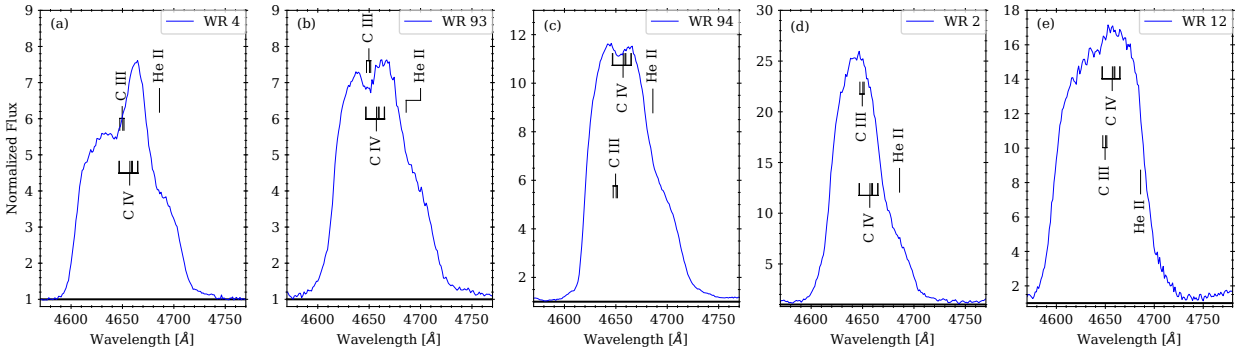

Figure 36: *Normalized spectra of the stars WR 4, 93, 94, 2, 12 (from a–e) for the Bowen blend to illustrate the various line shapes.*

three stars of the sample are displayed where the line shape shows an additional, central peak. The model calculations are not able to reproduce those observations. The model parameters for the fit for those star allow a decent fit along the entire spectrum, and also the Bowen blend is reproduced in its overall flux, but the line shape is not. This might be a sign of contamination. However, the fact that the overall flux in the blend is reproduced with a reasonable overall model fit is an indication against this idea and only M 31 WR 4 of the shown stars was classified as binary *suspect* while the others are all *single* stars. The stars that inhabit this double peak line shape show all signs of very fast rotation ($v_{\rm rot} > 2000{\rm km\,s^{-1}}$). The detailed calculations have shown that the Bowen blend itself is barely affected by rotation in terms of line broadening. But the fast rotation does not only cause line broadening, it shapes the entire star ellipsoidal and can cause decretion disks. Those deviations from spherical symmetry might be responsible for line shapes like this. On the other hand, not all fast rotating stars do show this kind of line shape. Unfortunately, there is no way to explore this in more detail as PoWR only calculates one dimensional, spherical symmetric atmospheres. Note that a similar line shape for galactic WC stars is only observed for WR 021 (cf. Sander et al. 2012), which is also a WN/WC transition type and the second peak here is clearly given by He II. All stars that show this observed double peak structure, require models with reduced carbon abundances, partly the inclusion of nitrogen to reproduce the spectra and high rotational velocities.

Sharp lines on the wings of C IV λ5808: This prominent emission line has a much simpler structure then the Bowen blend as it is dominated by the C IV doublet. Only He I λ5877 contributes a notable flux. However, some of the same stars that already became conspicuous due to the unusual shape of the Bowen blend do also show a peculiarity for this emission line. In Fig. 37 the same stars are displayed as in Fig. 36. However, not all line shapes are as simple as assumed. M 31 WR 93 and 94 show a sharp cut at around 5840 Å. Due to their high T_* and v_∞, there are usually no sharp lines in

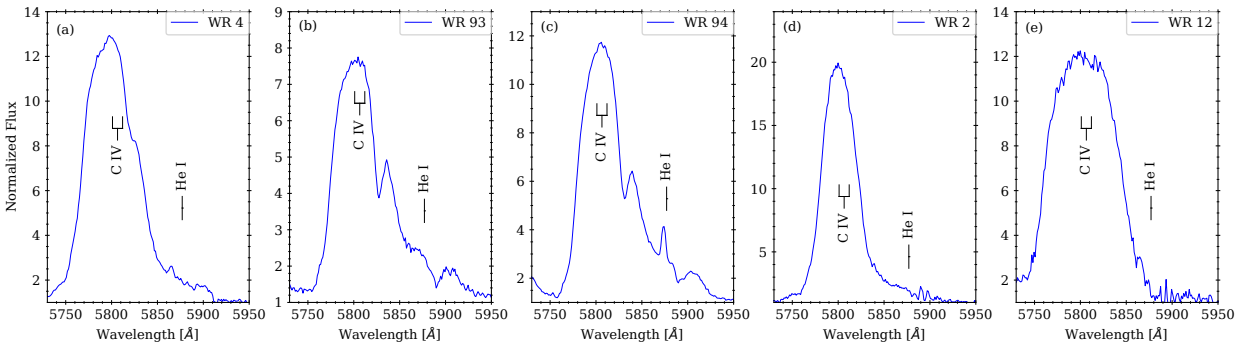

Figure 37: *Normalized spectra of the stars WR 4,93,94,2,12 (from a–e) for* C IV *λ*5808 *illustrate the various line shapes. Note that those are the same stars as in Fig. 36*

the spectrum of WR star. Narrow and pointy emission lines originate from nebula emissions. Pointy absorption like features can result from two close-by emission lines, whose red and blue wings almost touch, respectively. Those structures are observed in the present data and are also reproduced by the model atmospheres. However, the line shape in question here is different. Its edges are in principle too sharp to be of stellar origin. But certain sets of model parameter do reproduce an absorption line feature with an appropriate strength at the right position (see model fit for WR 94). But those features are in fact broadened and do not show a similar pointy-like appearance. However, we assume the line to be of stellar origin and might be shaped by internal wind structures like clumping or the wind velocity field. A time series observation of this line might grants some interesting details on WC winds.

7.9 Fitting the suspects

Originally, we also attempted to fit the binary suspects, but to exclude the derived parameters from the discussion. This attempt failed as the suspects spectra were also not reproducible in a reasonable way. The observed line strengths of the prominent lines might still reach a significant level, but in combination with all other observed line features in the spectrum no consistent fit could be achieved. Therefore, we decided to also exclude the suspect stars from the attempt of a spectral fit. The probability is high that those stars are actually also multiple systems and a detailed analysis of those would be beyond the scope of this thesis.

7.10 A spectrum of more than just stars

We mentioned already the impact of extinction and reddening for the observed SED. As we directly look out of the Galactic disk, the impact of local gas on the reddening is negligible. It is the local gas around the stars in M 31 that has the stronger impact. Next to absorption and scattering, the ISM in M 31 contributes to the SED and spectra in the form of nebula emission lines. We do not want to go into the details of the formation of those lines, but due to their very narrow linewidth, nebula lines are easily distinguishable from the emissions of WR stars.

Those emission originate in excited gaseous regions. The excitation is usually caused by a strong radiative source, such as an early type star. Therefore, we can expect to find nebula emission in the spectrum of a WR star as it creates H II/He III regions and emission nebula around itself. If we investigate our data, we find such emission lines in the spectra of a large fraction of stars (Fig. 38). The line strengths of the individual elements forming such an nebula spectrum can provide information on the metalicity of the ISM. But an analysis in this regard is beyond the scope of this thesis. Note that we also have WR stars in our sample whose spectra do not show any significant nebula emissions. This can indicate a situation where the massive stars have blown away all gas around them with their strong wind, leaving no gas that could cause those emissions.

7.11 Room for improvement

The model fits presented in this work and used to determine the stellar parameter do not perfectly reproduce all of the observed spectra. Some of the issues were already discussed in Sect. 7.8, 7.2.5, and 7.2.6. Some originate in the limitations of the modeling process, some are caused by spectral contamination. Furthermore, the time constraints on this work limit us to in the depth of the exploration of the spectral fits.

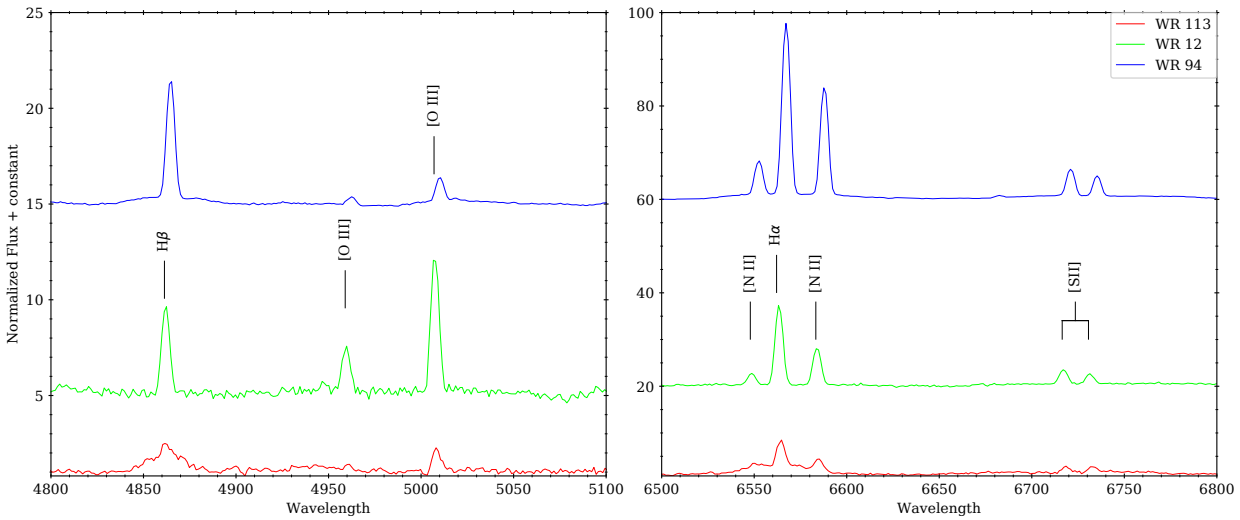

Figure 38: *Cutouts of the normalized spectra (+ constant) of WR 12, 94, and 113 around the prominent nebula emissions. The three stars exhibit the strongest nebula lines in the sample. While for WR 13 and 113, the cause of the emissions is not visible, WR 94 has created a large wind blown bubble around itself together with an extended* H II *region (see Fig. 72). Note that the spectra shown here are corrected for the wavelength shift due to the radial velocity of the star, which can cause the nebula emissions to not be aligned with their rest frame wavelength.*

We present now a list of points, insights and findings that could not be investigated more into detail due to time constraints. Those await future work on the subject.

Velocity Law: The velocity field in the wind is a highly discussed topic. From the early attempts for a description (Castor et al. 1975b), to the modern attempts with hydro-dynamically consistent models (Sander et al. 2017), a satisfying solution is yet still pending. We adopted a classical β-law with $\beta = 1$ for all models. A more detailed investigation of the spectral behavior with a changed β or even a double-β-law are not feasible in the time frame for this thesis. However, a small number of models were calculated with a changed β. The adopted values range between 0.5 and 10. It could be observed that

- the emission lines get generally stronger with an increasing β;
- the line wings of neighboring lines merge for lower β, as described in Sect. 7.2.1.

Especially the first point can change the position of a star in the $\mathcal{R}-\mathcal{T}$-plane. The individual behavior of the spectral lines under the change of β needs to be investigated. But this is a long process that has to be done for each star individually and requires a vast amount of computational time. Therefore, we didn't investigated this further.

C III as indication for the temperature: The optical spectra utilized in this work show three C III lines with varying strength at 4068−168 Å, at 5696 Å, and at 6727−73 Å. Throughout our analysis, it seemed that those lines each react differently on changes of the model parameters. A future investigation could explore the applicability of the 5696 Å to 6727 − 73 Å ratio to determine the stellar temperature (cf. Fig. 18).

Partly co-rotating winds: We found very fast rotation for some of the stars. The applicability of the rotational broadening method presented by Shenar et al. (2014) was confirmed in this work by observing the varying impact of rotation on spectral lines across stellar spectra (cf. Sect. 7.2.9). This can be investigated for the dependency on the co-rotation radius and the interplay with the wind velocity field. To a limited extend this is done here, but only exemplarily for one star. Furthermore, the rotational velocity field is most likely more complex than assumed here. Different fields ought to be tested.

All those points can be done with the current state of spectral modeling and the available data. They are omitted here due to time constraints.

7.12 Error Estimation

As can be seen above, we haven't denoted any errors to our derived stellar parameter so far. In this section want to shortly address how errors are estimated. The spectral fits are done by eye. No RMS or χ^2 fitting

was used. Therefore, the quantification of errors is based on observable changes in the spectral fit and the errors denote the range where there is no significant change in the synthetic spectra that worsens the fit. The free parameter for our spectral fits are:

Temperature: We find significant changes when deviating from the best fit by $0.5\,\mathcal{T}$ (half a grid step). This corresponds to a temperature error of $\Delta T = \pm 0.025\,\mathrm{dex}$.

Transformed radius: For stars showing C III λ5696, the uncertainty is rather small with $0.1\,\mathcal{R}$. This corresponds to $\Delta R_t = \pm 0.01\,\mathrm{dex}$. For stars that do not show C III λ5696 (WC4 stars) the error is larger as the the other lines do not react that strongly on changes in R_t. Therefore, we estimate the error to $0.3\,\mathcal{R}$, corresponding to $\Delta R_t = \pm 0.03\,\mathrm{dex}$.

Terminal velocity: For all stars the uncertainty is $\Delta v_\infty = \pm 100\,\mathrm{km\,s^{-1}}$.

Chemical abundances: For the carbon abundance, we find an uncertainty in mass fraction of $\Delta X_\mathrm{C} = \pm 0.05$. The silicon abundance is only an upper limit. The actual abundance might be lower be an order of magnitude compared to the derived value here. The oxygen abundance, when only estimated from O V $\lambda\lambda 5336 - 5519$ has an uncertainty in its mass fraction of $\Delta X_\mathrm{O} = \pm 0.01$.

Rotational velocity: v_rot at R_corot is uncertain by $\Delta v_\mathrm{rot} = \pm 250\,\mathrm{km\,s^{-1}}$due to the broad lines.

Luminosity: $\log L$ is precise to $\Delta \log L/L_\odot = \pm 0.1\,\mathrm{dex}$.

Clumping The clumping factor is only seen in the line wings of strong emission lines that are caused by electron scattering. Due to ambiguities with the normalization around the prominent lines, the uncertainty is rather larger with $\Delta D = \pm 50\%$

Radial velocity: Due to the broad lines and the partially low S/N, the error on the radial velocity is $\Delta v_\mathrm{rad} = \pm 50\,\mathrm{km\,s^{-1}}$.

Additional parameter like the stellar radius, mass, and mass-loss rate are derived parameters from the above.

8 Results

»Every result achieves its perfection by serving not one, but several objectives.«

– Aristotle, loosely based

In this section the results for the sample stars are summarized. Table 9 gives an overview about the main parameters derived for the WC sample. A complete overview of all derived parameters is given in Appendix A Table 16.

Table 9: *Derived parameter for WC sample; only the single stars*

Star	LGGS	WC	$T_{2/3}$ [kK]	$T_{\rm eff}$ [kK]	$\log L$ [$L_\odot$]	M_* [$M_\odot$]	R_* [$R_\odot$]	v_∞ [km s^{-1}]	$\log \dot{M}$ [$M_\odot$ yr^{-1}]
WR 2	J003911.04+403817.5	6	62.0	89.0	5.4	12.8	2.11	2000	-4.62
WR 7	J003939.97+403450.4	6	65.0	71.0	5.3	11.5	2.98	2000	-5.03
WR 12	J004019.47+405224.9	4	98.0	188.0	5.6	16.9	0.59	2800	-4.83
WR 13	J004020.44+404807.7	6	59.0	71.0	5.6	16.7	4.21	2300	-4.50
WR 15	J004022.43+405234.6	4	65.0	71.0	5.6	17.7	4.21	2200	-4.83
WR 19	J004029.27+403916.6	5	64.0	67.0	5.4	13.1	3.75	2500	-5.07
WR 23	J004034.69+404432.9	4	67.0	71.0	5.4	13.0	3.34	2000	-4.98
WR 43	J004134.99+410552.3	7	65.0	79.0	5.6	17.0	3.34	2300	-4.65
WR 54	J004213.21+405051.8	4	98.0	178.0	5.55	15.3	0.63	2600	-4.80
WR 55	J004214.36+412542.3	6	59.0	71.0	5.45	14.3	3.54	2200	-4.74
WR 93	J004408.58+412121.2	6	55.0	71.0	5.85	25.5	5.61	2200	-4.35
WR 94	J004410.17+413253.1	6	57.0	75.0	5.9	27.2	5.29	2300	-4.36
WR 96	J004412.44+412941.7	6	57.0	67.0	5.9	27.1	6.67	2400	-4.47
WR 102	J004422.24+411858.4	7-8	46.0	60.0	5.3	12.2	4.21	1100	-4.82
WR 113	J004436.52+412202.0	5	56.0	79.0	5.5	15.7	2.98	1800	-4.61
WR 121	J004451.98+412911.6	7	53.0	60.0	5.2	10.5	3.75	1400	-4.92
WR 123	J004453.52+415354.3	7	53.0	63.0	5.1	9.3	2.98	1200	-5.05
WR 124	J004455.63+413105.1	6	54.0	56.0	5.62	17.8	6.82	2000	-4.83
WR 132	J004511.27+413815.3	6	59.0	63.0	5.7	19.7	5.94	1900	-4.76
WR 138	J004522.78+420318.2	5-6	87.0	178.0	5.2	10.2	0.42	1800	-5.12
WR 139	J004524.26+415352.5	6	63.0	71.0	5.2	10.2	2.65	2000	-5.12
WR 150	J004551.12+421015.4	5-6	82.0	178.0	5.4	13.0	0.53	1600	-5.05
WR 151	J004551.35+414242.0	6	67.0	178.0	5.3	11.7	0.47	1800	-4.91

In the subsequent subsections, we will address individual parameters separately, summarized for the *sample* stars. This will be done for all the parameters where a summation of the results is actually meaningful for M 31 as a whole, like metalicity, stellar feedback, and the radial velocity profile. Detailed analyses of the derived parameters and their relation to each other and the evolution of WC stars are discussed in Sect. 9.

8.1 Radial velocity

The radial velocities from line shifts can be obtained for all WC stars, even for the ones with a diluted spectrum. If one investigates the spatial distribution of the measured velocities, see the left panel of Fig. 39, two points become obvious.

1. The radial velocities reproduce, at average, the rotation of M 31.
2. However, the absolute values of the velocities in the assumed rest frame of M 31 indicate that the rest frame might be off by $v \approx -100\,\mathrm{km\,s^{-1}}$, resulting in a system velocity of M 31 of $r_{\mathrm{rad}} \approx -400\,\mathrm{km\,s^{-1}}$.
3. Furthermore, it seems that the rotational axis is not in the visual center of the galaxy.

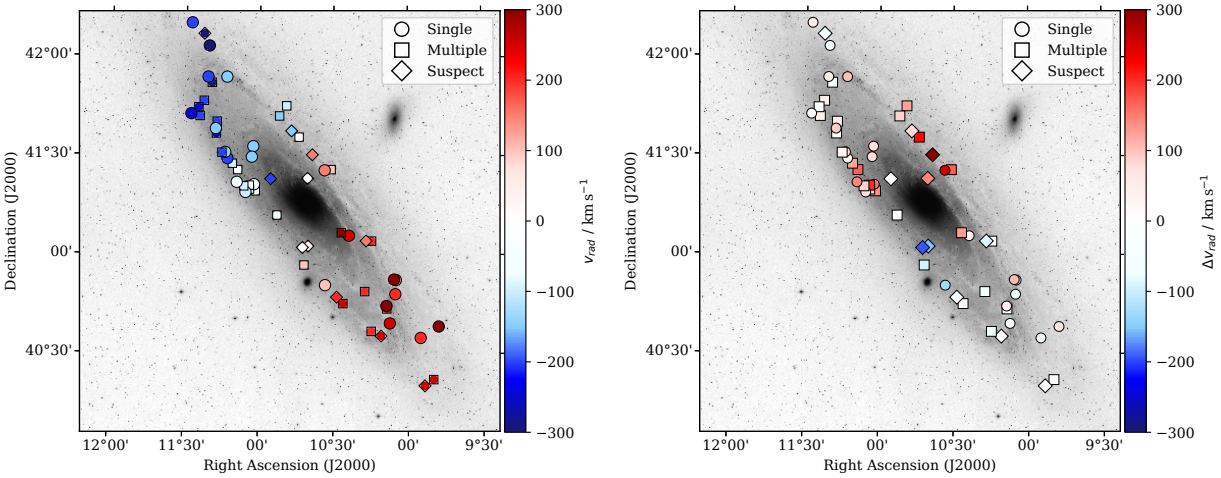

Figure 39: *Radial velocity map of all WC stars in M 31. The color coding denotes the measured radial velocity in the rest frame of M 31. The marker shape denotes the assigned status as indicated. Background image: DSS2 blue on an inverted gray scale*
Left panel: *Rotational velocity in the rest frame of M 31 as observed in the spectra.*
Right panel: *Rotational velocity additionally corrected for the rotation of M 31 as described in Sect. 8.1 and Fig. 40. WR 55 is lies north-west of and close to the center of M 31. It is the only* sample *star that shows a large deviation between expected and measure radial velocity.*

To find peculiarities and outliers among the radial velocity we have to subtract the rotation of M 31 for the individual stars. If we assume the projection of M 31 in the night sky as described in Sect.3.2 and adopt a circular shape with a radial velocity curve based on the measurements by Unwin (1983) and Carignan et al. (2006), we can reconstruct the radial velocity of any location in M 31. The upper panel in Fig. 40 shows the adopted rotation curve with a parabolic interpolation between the measurements and extrapolation to larger radii. Negative radii represent hereby already the projection on the night sky with the sign of the velocity changed. The interpolation is assumed to be parabolic for the reasons:

1. A smooth and steady curve is more physical than a just linear interpolation between the points.
2. A cosine spline would only work for an interpolation and is not suitable for an extrapolation.
3. Higher order polynomials, like a cubic spline, as interpolation resulted in nonphysical results for the extrapolation to larger radii.

The only further physical and very reasonable assumption taken was that the radial velocity curve is symmetric around the center of M 31 at 00:42:44.330 +41:16:07.50 (Skrutskie et al. 2006). This radial velocity curve is then adopted under the assumption of circular orbits and the lower right panel in Fig 40 shows a face on view of how the projected radial velocity of each point in such a galaxy would look like when observing edge on. The lower left panel projects this field on M 31, enabling us to estimate the projected orbit velocity of the individual star based on their location. Everything that was described before assumes that all stars are located inside an infinitesimal thin disk.

With the apparent radial velocity known at any location inside the disk of M 31, we can calculate the radial component of the peculiar velocity for individual stars. The location and the distance to the galactic center of the stars in M 31 can be determined by the same projection adopted above and the results are summarized in Appendix A Table 17. We are interested in the difference between the expected velocity due

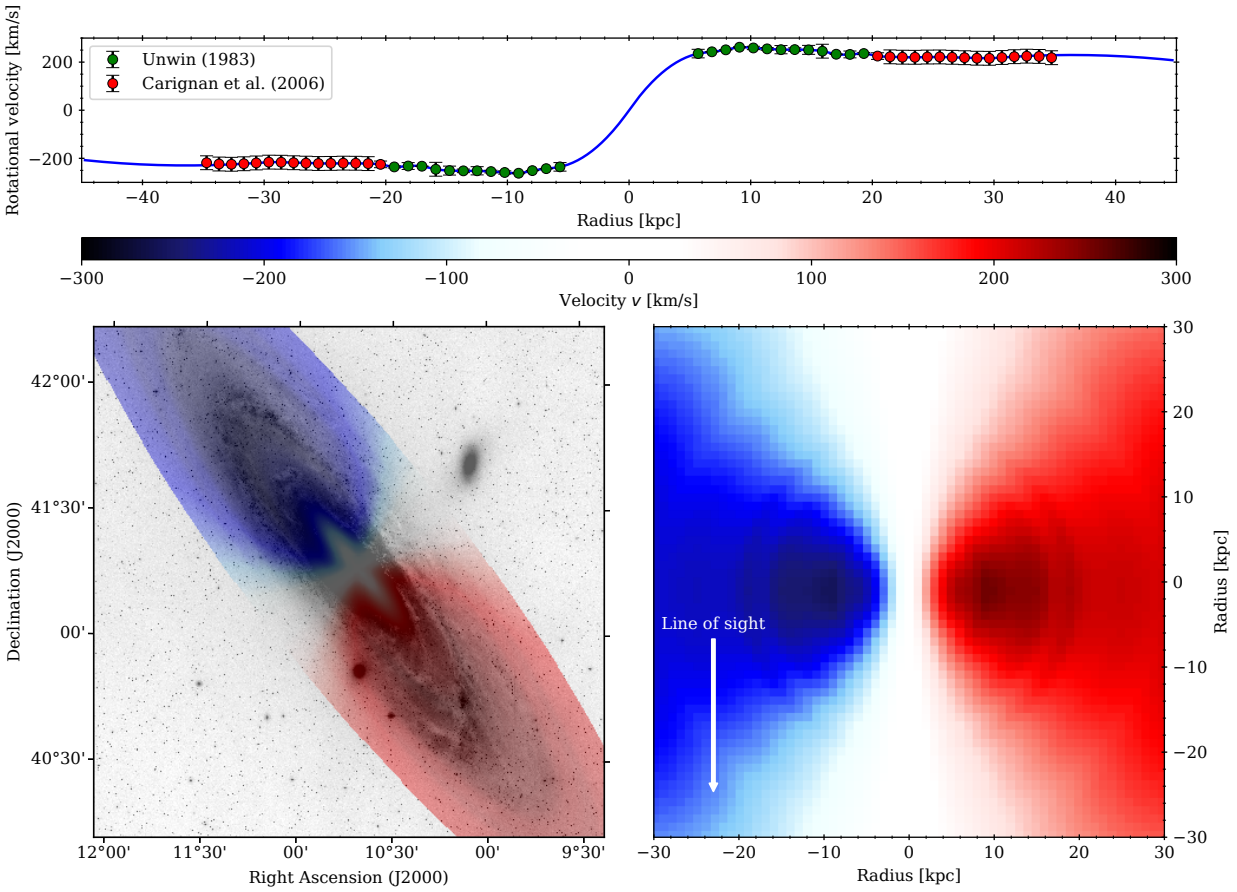

Figure 40: *The rotation of M 31*
Upper panel: *Measured radial velocities in M 31 (Unwin 1983; Carignan et al. 2006, green and red points respectively) and an parabolic inter- and extrapolation based on these measurements (blue solid line).*
Lower right panel: *Face on view of a galaxy with circular orbits and the rotation curve from the upper panel. The color coding gives the projected velocity from rotation as seen edge on along the indicated line of sight.*
Lower left panel: *Rotation profile from the right panel projected on M 31, accounting for the inclination of $i_{And} = 77°$ and a position angle of 54°. The color coding gives the apparent radial velocity due to rotation. Only regions with $R <= 20$ kpc are colored. Background image DSS2 blue on an inverted gray scale. Note that to make M 31 and the rotation profile visible in the image simultaneously, latter is shown with 60% transparency which might causes a wrong impression of the shown colors.*

to the rotation of M 31 and the observed ones. The right panel in fig. 39 shows the resulting velocities which are also listed in Appendix A Table 17. For most of the stars the difference is in the order of the assumed uncertainty for measurement of the radial velocity from the spectra. The agreement is much better than expected, since quite a number of uncertainties and assumptions went into the calculation of the expected projected rotational velocity. However, some stars show large deviations. We will assume generously that deviations up to 150 km s^{-1} are due to the shortcomings with the projection, that the disk is not infinitely thin, and the orbits are not circular. However, deviations above 150 km s^{-1} might indicate binaries or run-away stars.

Note that the velocities shown in Fig. 39 show a suspicious behavior. The most obvious deviations from the expected radial velocity is present for stars close to the line of sight in the north eastern half of M 31. This was already mentioned above.

We can see that the strong deviations between expected and measured radial velocity is found basically only for binary suspects and multiples. WR 55 is the only *sample* star that shows a strong deviation in its radial velocity. There is no HST image to investigate the stellar neighborhood, but the DSS2 image shows vicinity to a denser populated region. This star might be a run-away. The spectrum does not show signs multiplicity. The observed reddening combined with the weak nebula lines might indicate that this stars sits behind the disk of M 31.

8.2 Chemical abundances

A good estimate of the stellar evolutionary state is given by the abundances derived for the individual stars. Table 10 gives an overview of the found chemical composition of the individual stars. The helium and carbon abundances span a large parameter range from stars almost purely made of helium to more than 60% carbon. Three stars are found to have nitrogen visible in their spectra. The appearance of nitrogen coincides with a low carbon abundance, as one would expect. All stars need the inclusion of silicon to the model calculations. We derive partly abundances that are more than ten times solar. In Fig. 41, we show a map of the found helium abundance for the sample stars. No correlation between the distance or the general position of a star and its abundances is visible. Stars in proximity, like WR 93, 94, and 96, which have similar helium abundances might share the same star formation history.

Table 10: *Stellar abundances for WC sample; only the single stars. All abundances listed as mass fraction*

Star	LGGS	He	C	N	O	Si
WR 2	J003911.04+403817.5	3.7E-1	6.0E-1	-	3.0E-2	1.0E-3
WR 7	J003939.97+403450.4	4.8E-1	5.0E-1	-	2.0E-2	6.5E-4
WR 12	J004019.47+405224.9	4.1E-1	5.0E-1	-	8.0E-2	1.0E-2
WR 13	J004020.44+404807.7	3.4E-1	6.0E-1	-	5.0E-2	5.0E-3
WR 15	J004022.43+405234.6	7.9E-1	1.5E-1	6.0E-3	5.0E-2	5.0E-3
WR 19	J004029.27+403916.6	5.0E-1	4.5E-1	-	5.0E-2	6.2E-4
WR 23	J004034.69+404432.9	4.4E-1	5.0E-1	-	6.0E-2	1.0E-3
WR 43	J004134.99+410552.3	4.6E-1	5.0E-1	-	4.0E-2	1.0E-3
WR 54	J004213.21+405051.8	1.9E-1	7.0E-1	-	1.0E-1	5.0E-3
WR 55	J004214.36+412542.3	6.8E-1	3.0E-1	-	2.0E-2	2.0E-3
WR 93	J004408.58+412121.2	8.9E-1	1.0E-1	2.0E-3	1.0E-3	1.0E-2
WR 94	J004410.17+413253.1	7.9E-1	2.0E-1	-	1.0E-2	2.0E-3
WR 96	J004412.44+412941.7	7.3E-1	2.5E-1	-	2.0E-2	1.0E-3
WR 102	J004422.24+411858.4	8.3E-1	1.5E-1	-	1.0E-2	5.0E-3
WR 113	J004436.52+412202.0	8.7E-1	1.0E-1	2.5E-2	5.0E-3	1.0E-3
WR 121	J004451.98+412911.6	6.8E-1	3.0E-1	-	2.0E-2	1.0E-3
WR 123	J004453.52+415354.3	6.3E-1	3.5E-1	-	9.0E-3	5.0E-3
WR 124	J004455.63+413105.1	6.3E-1	3.5E-1	-	2.0E-2	2.0E-3
WR 132	J004511.27+413815.3	5.1E-1	4.5E-1	-	4.0E-2	2.0E-3
WR 138	J004522.78+420318.2	4.7E-1	5.0E-1	-	2.0E-2	1.0E-3
WR 139	J004524.26+415352.5	4.8E-1	5.0E-1	-	2.0E-2	6.5E-4
WR 150	J004551.12+421015.4	4.7E-1	5.0E-1	-	2.0E-2	1.0E-3
WR 151	J004551.35+414242.0	5.7E-1	4.0E-1	-	2.0E-2	5.0E-3

Note that the silicon and nitrogen abundances have to be seen as an upper limit, the oxygen abundance is rather uncertain and the the iron abundance is assumed to be solar.

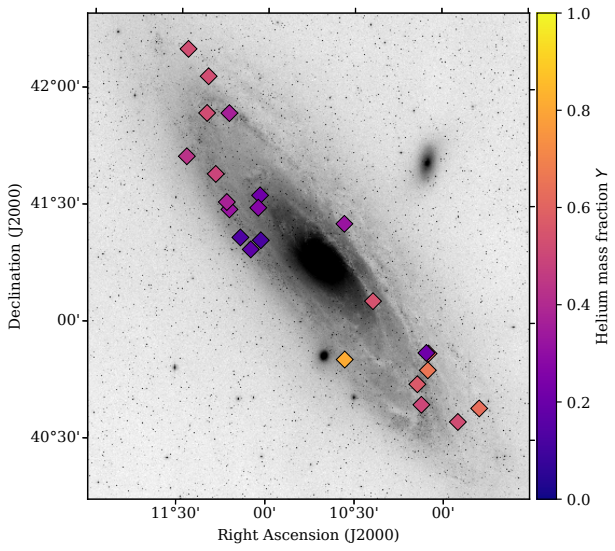

Figure 41: *Map of M31 with the WC sample stars. The helium mass fraction is color coded. Background image: DSS2 blue on an inverted gray scale*

8.3 Stellar rotation

Only for the fast rotators a line broadening is visible in the form broad and roundish lines. Furthermore, the estimation is rather imprecise with a typical error of $\pm 250\,\mathrm{km\,s^{-1}}$. This also indicates another point. Some of the stars are very fast rotating. PoWR assumes a spherical symmetric star while calculating the emergent spectrum and for a moderately rotating star this approximation is valid. But for fast rotating stars deformation like flattening or even decretion disk will break this symmetry. And this will also be visible in the spectrum. A good indicator of how much a star is deformed by its own rotation is its critical rotational velocity, which gives the velocity at which point the stellar gravity is completely counterbalanced by centrifugal forces:

$$v_{\mathrm{crit}} = \sqrt{\frac{M_* \cdot G}{R_{\mathrm{eq}}}}. \tag{10}$$

With the stellar mass M_*, the equatorial radius of the star R_{eq} and the gravitational constant G. For a WR star, the gravity at the stellar surface is already counterbalanced by radiative pressure. Otherwise there would not be any stellar wind. This means the critical velocity is even lower than in Eq. (10). But as the radiative pressure is difficult to determine precisely, we stay with Eq. (10) and consider it an upper limit to the critical velocity.

In Table 11, we list the determined rotational velocity, together with v_{crit} which was derived from our determined stellar parameter and the ratio between those as an indicator for deformation of the individual star for the sample. The stellar atmosphere is assumed to co-rotate up to $R_{\mathrm{corot}} = 1.1\,R_*$ with $v_{\mathrm{rot}} \sin(i)$ denoting the rotational velocity at R_{corot}. The rotational velocity at the stellar photosphere $v_{*,\mathrm{rot}} \sin(i)$ is then given by

$$v_{*,\mathrm{rot}} \sin(i) = \frac{v_{\mathrm{rot}} \sin(i)}{R_{\mathrm{corot}}/R_*}, \tag{11}$$

as described in Shenar (2013).

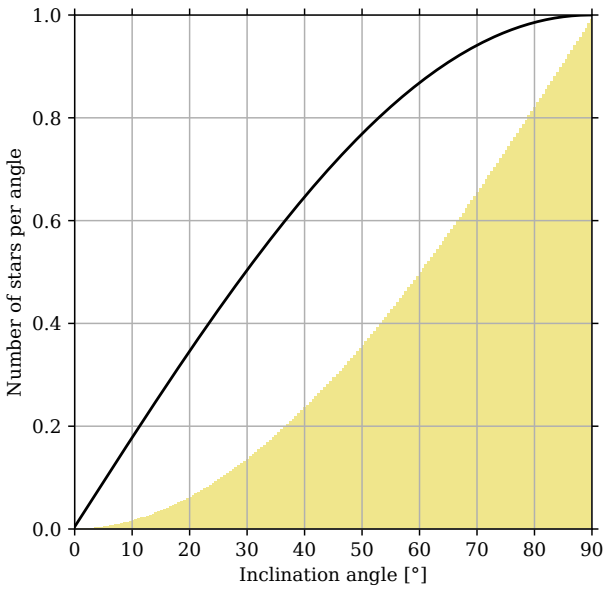

Figure 42: *Projection angles of randomly distributed inclinations for a fixed observer. The black curve indicates the number of stars in an angle bin normalized to the maximum value. A cumulative histogram is shown in yellow indicates the number of stars with inclination below the denoted angle.*

The found rotational velocities are surprisingly high and they exceed the critical velocity for about half of the sample stars. Strong effects of rotation have only been observed for a small sample of WR stars so far (e.g. by Shenar et al. 2014; Sander et al. 2012). Due to the fact that the obtained velocities appear not physical, since they would cause the disintegration of the star, we will discuss possible reasons for the observed velocities and investigate a parameter degeneracy between $v_{\mathrm{rot}} \sin(i)$ and R_{corot} in Sect. 9.4.

Table 11: *Stellar rotation for WC sample; only the single stars.* $v_{rot}\sin(i)$ *is the stellar rotation adopted for the star, and* v_{crit} *is the critical velocity, calculated according to Eq.* (10). R_{corot} *denotes the co-rotation radius in stellar radii and* $v_{*,rot}\sin(i)$ *is the rotation at the stellar surface. For the calculation of latter see Eq. 11.*

Star	LGGS	$v_{\rm rot}\sin(i)$ km s^{-1}	$R_{\rm corot}$ $[R_*]$	$v_{*,\rm rot}\sin(i)$ km s^{-1}	$v_{\rm crit}$ km s^{-1}	$v_{*,\rm rot}\sin(i)/v_{\rm crit}$
WR 2	J003911.04+403817.5	0.0	1.1	0.0	1080.5	0.00
WR 7	J003939.97+403450.4	2000.0	1.1	1818.2	860.7	2.11
WR 12	J004019.47+405224.9	500.0	1.1	454.5	2334.0	0.19
WR 13	J004020.44+404807.7	2000.0	1.1	1818.2	873.5	2.08
WR 15	J004022.43+405234.6	1500.0	1.1	1363.6	898.7	1.52
WR 19	J004029.27+403916.6	1500.0	1.1	1363.6	818.5	1.67
WR 23	J004034.69+404432.9	2500.0	1.1	2272.7	862.9	2.63
WR 43	J004134.99+410552.3	2500.0	1.1	2272.7	987.5	2.30
WR 54	J004213.21+405051.8	0.0	1.1	0.0	2158.4	0.00
WR 55	J004214.36+412542.3	2500.0	1.1	2272.7	881.3	2.58
WR 93	J004408.58+412121.2	2500.0	1.1	2272.7	933.0	2.44
WR 94	J004410.17+413253.1	3000.0	1.1	2727.3	992.7	2.75
WR 96	J004412.44+412941.7	2500.0	1.1	2272.7	882.5	2.58
WR 102	J004422.24+411858.4	500.0	1.1	454.5	744.8	0.61
WR 113	J004436.52+412202.0	0.0	1.1	0.0	1005.1	0.00
WR 121	J004451.98+412911.6	1000.0	1.1	909.1	734.0	1.24
WR 123	J004453.52+415354.3	0.0	1.1	0.0	773.7	0.00
WR 124	J004455.63+413105.1	1000.0	1.1	909.1	708.3	1.28
WR 132	J004511.27+413815.3	1000.0	1.1	909.1	796.9	1.14
WR 138	J004522.78+420318.2	0.0	1.1	0.0	2152.3	0.00
WR 139	J004524.26+415352.5	2000.0	1.1	1818.2	857.6	2.12
WR 150	J004551.12+421015.4	500.0	1.1	454.5	2174.7	0.21
WR 151	J004551.35+414242.0	0.0	1.1	0.0	2178.3	0.00

If we assume the orientation of the stellar rotation axis as randomly distributed in space the inclination of the axis behaves as displayed in Fig. 42. 50% of the stars have an inclination of $> 60°$. This means vice versa that for a small number of stars ($\approx 15\%$) the rotational velocity is underestimated by a factor of > 2 ($i \leqslant 30°$), and for the majority of the sample stars the rotational velocity is only slightly underestimated.

An additional point to mention here is that the deformation of the star can cause an error in our estimate of the stellar luminosity and mass loss. The observed luminosity differs for a fast rotating star when seen pole on or at the equator (cf. Von Zeipel theorem, von Zeipel 1924) and cause an error up to a factor of 2 (Peterson et al. 2006). Furthermore, the strong rotation can also result in anisotropic mass loss (Maeder 1999). Investigating those effects is impossible from our spectral data and also beyond the scope of this work.

8.4 Interstellar reddening

The interstellar redding is no stellar parameter. A meaningful estimation of the redding is only possible for the single stars as for the other the stellar SED is unknown. For all stars the reddening laws of Seaton (1979) and Nandy et al. (1975) were adopted as described above. The resulting reddening parameter are listed in Appendix A Table 16.

As the reddening is more an important factor for the research on the ISM in M 31, we do not list the derived values here. Figure 43 shows the reddening distribution in M 31 according to our sample. Naturally, our sample size is too small for a any meaningful conclusions. However, notable is that the reddening does not exceed $E_{B-V} = 0.2$, and no overall structure in the distribution is recognizable.

8.5 Stellar feedback

The stellar feedback is an important matter for the evolution of galaxies and the enrichment with heavy elements. In Table 12, we summarize the results of our analysis for the chemical enrichment, mechanical feedback and ionizing radiation for the individual stars and give a total amount for all the analyzed stars in the sample.

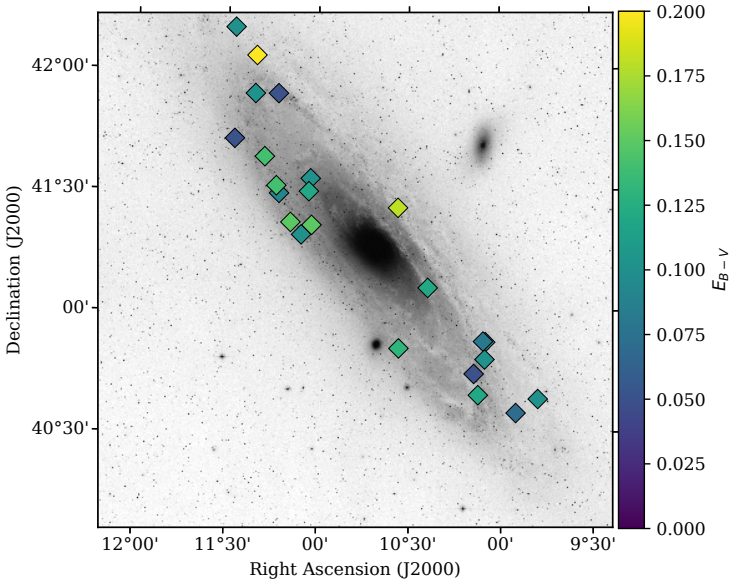

Figure 43: *Reddening map of the WC sample stars. The color coding shows the found $E(B-V)$.*

Table 12: *Stellar feedback for the WC sample; only the single stars. The first column block gives basic informations about the star. The second column block lists the amount of matter outflow for the individual stars. Note that the matter given for the wind outflow is given in earth masses per year. The mechanical feedback is calculated in the third column block and the final column block denotes the ionizing photons for hydrogen and helium in photons per second.*

Star WR	WC #	q_{He}	q_{C}	q_{N}	q_{O}	q_{Si}	q_{Fe}	E_{mech} erg s^{-1}	$[L_\odot]$	H	He I	He II
		Wind outflow $[M_\oplus/\mathrm{yr}]$								$\log Q_{\mathrm{ion}}$		
2	6	2.94	4.81	-	0.24	0.008	0.013	6.1E+38	$10^{4.20}$	49.2	48.4	37.7
7	6	1.51	1.58	-	0.06	0.002	0.005	2.4E+38	$10^{3.79}$	49.1	48.3	37.8
12	4	2.03	2.50	-	0.40	0.050	0.008	7.4E+38	$10^{4.29}$	49.4	48.7	38.9
13	6	3.63	6.35	-	0.53	0.053	0.017	1.1E+39	$10^{4.44}$	49.4	48.4	36.7
15	4	3.87	0.74	0.03	0.25	0.025	0.008	4.5E+38	$10^{4.07}$	49.4	48.8	38.3
19	5	1.42	1.28	-	0.14	0.002	0.005	3.4E+38	$10^{3.94}$	49.2	48.4	37.9
23	4	1.53	1.75	-	0.21	0.003	0.006	2.7E+38	$10^{3.84}$	49.2	48.7	39.8
43	7	3.43	3.75	-	0.30	0.008	0.012	7.5E+38	$10^{4.29}$	49.4	48.5	37.0
54	4	1.00	3.68	-	0.53	0.026	0.008	6.7E+38	$10^{4.24}$	49.3	48.8	39.6
55	6	4.16	1.84	-	0.12	0.012	0.010	5.6E+38	$10^{4.17}$	49.2	48.3	36.2
93	6	13.33	1.51	0.03	0.02	0.151	0.024	1.4E+39	$10^{4.56}$	49.6	49.1	39.1
94	6	11.38	2.90	-	0.14	0.029	0.023	1.5E+39	$10^{4.58}$	49.7	48.8	36.5
96	6	8.23	2.83	-	0.23	0.011	0.018	1.2E+39	$10^{4.51}$	49.6	48.6	36.5
102	7-8	4.21	0.76	-	0.05	0.025	0.008	1.2E+38	$10^{3.48}$	49.0	47.9	34.5
113	5	7.18	0.83	0.21	0.04	0.008	0.013	5.1E+38	$10^{4.12}$	49.3	48.6	37.7
121	7	2.71	1.20	-	0.08	0.004	0.006	1.5E+38	$10^{3.59}$	49.0	48.2	37.3
123	7	1.88	1.04	-	0.03	0.015	0.005	8.1E+37	$10^{3.32}$	48.9	47.9	35.6
124	6	3.07	1.71	-	0.10	0.010	0.008	3.7E+38	$10^{3.98}$	49.4	48.4	36.6
132	6	2.95	2.62	-	0.23	0.012	0.009	4.0E+38	$10^{4.01}$	49.5	48.6	37.1
138	5-6	1.21	1.28	-	0.05	0.003	0.008	1.6E+38	$10^{3.61}$	49.0	48.3	38.6
139	6	1.23	1.28	-	0.05	0.002	0.004	1.9E+38	$10^{3.70}$	49.0	48.1	37.2
150	5-6	1.40	1.48	-	0.06	0.003	0.009	1.4E+38	$10^{3.57}$	49.2	48.4	38.2
151	6	2.38	1.67	-	0.08	0.021	0.010	2.6E+38	$10^{3.82}$	49.0	48.1	36.5
	Total	86.7	49.38	0.27	3.94	0.482	0.238	1.2E+40	$10^{5.50}$	50.7	49.9	40.2

As the chemical enrichment is an important matter for planet formation, we give the amount of an element blown into the ISM in earth masses $M_\oplus$. The individual values are calculated as described in Sect. B. Note that this is just the amount of matter currently transported by the wind. There is no estimate for the evolution over time of those values as well no account for the amount of the specific element that was present when the star formed from the ISM to determine the actual yield.

We stated above that the feedback of WR stars is significant and can be larger compared to SNe. With our derived feedback parameter, we can make a rough estimation. Table 12 lists the cumulative mechanical luminosity and photon flux for the entire sample. If we assume the lifetime of a WR star to be $\approx 10^4$ yr

and that the derived parameter for our sample represent an average for this time, we can calculate the total feedback of a generation of WR stars. We find a total mechanical energy deposited in the ISM of

$$E_{\mathrm{mech}} = 3.78 \cdot 10^{51}\,\mathrm{erg}.$$

For the ionizing flux we adopt the number of hydrogen ionizing photons and assign to each of them the ionization energy of hydrogen to obtain a lower limit for the energy. We find

$$E_{\mathrm{ion}} = 3.65 \cdot 10^{51}\,\mathrm{erg}.$$

The energy released in a SN is in the order of $1 - 2 \cdot 10^{51}$ erg (Khokhlov et al. 1993). We see that our WC sample provides more total feedback than a SN by a factor of three to seven. And this is only our small sample. The total number of WC stars is a factor of two larger. Then there are also the WN stars. Furthermore, if we compare the number of known WR stars in M 31 to the MW, we find that the total number of WR stars in M 31 is probably higher by a factor of 20 or more. In total one can roughly say that the cumulative feedback a generation of WR stars in M 31 is about a factor of 10^2 higher compared to a SN. However, one also needs to account for the SN rate in M 31 which is estimated to be about one SN every 50 yr (Berkhuijsen 1984). At this rate, WR stars and SN would provide approximately the same amount of feedback.

9 Discussion

»Every conclusion we draw from an observation is most often preliminary, since behind the observed phenomena there are also such we see only vaguely and behind those probably there more which we don't see at all.«

– Gustave Le Bon

With all available data collected and the spectral analysis done for the individual stars of our sample, we can have a look on the implications provided by those results. Therefore, we compare our derived parameters with evolutionary models. In Fig. 44, we show HRDs of our sample stars together to the evolutionary tracks from Ekström et al. (2012).

When we look at the HRDs for T_* it is obvious that there seems to be two groups of stars in our sample. A group at very hot temperatures made of only an handful stars and one group composed of all other stars at significantly lower temperature. Both are spread over a large luminosity range. It was already noticeable during the fitting process that such a bifurcation emerges. When adopting the first appropriate models, most stars seem to be best reproduced by models with $70\,\mathrm{kK} \leqslant T_* \leqslant 90\,\mathrm{kK}$, while some needed very hot models with $T_* \simeq 180\,\mathrm{kK}$. This was, and still is, a surprising result. Previous analysis indicated a different behavior (e.g., Sander et al. 2012) but some do also confirm a confinement of the WC stars around $70\,\mathrm{kK} \leqslant T_* \leqslant 90\,\mathrm{kK}$ (cf. WC-s stars in Fig. 16 of Koesterke & Hamann 1995). It was argued that the found temperatures of WR stars are too low. WR stars are helium burning stars and can, to a certain extend, be seen as stars evolving of the helium Zero Age Main Sequence (He-ZAMS) and thus should have temperatures in this regime (cf. He-ZAMS in Fig. 44). But the found temperatures indicate that the stars are mostly much colder than that. This was already discussed by Hamann & Gräfener (2004) and later highlighted by the analysis of galactic WN stars by Hamann et al. (2006) and galactic WC stars by Sander et al. (2012).

In principle, the spectral degeneracy should allow to fit spectra with models with significantly different temperatures without changing the quality of the fit, as long as they are in the degeneracy regime. We attempted to proceed like this but found inconsistencies, since the spectral degeneracy is partly absent for the prominent emission lines (cf. Sect. 7.5). Exploiting the spectral degeneracy is not the way to overcome this issue.

A proposed physical explanation states that massive stars in their late evolutionary stages undergo a radius inflation, which leads to the apparent low temperatures (e.g., Gräfener et al. 2012; Grassitelli et al. 2018). The hot group of stars in our sample may not have undergone such an inflation. A conclusive solution for this problem[20] is still to be found.

Note that some of the spectral fits indeed indicate a slightly higher temperature (e.g., WR 113) with a mismatch for C IV λ5808. But those could not be solved by raising the stellar temperature. While the fit for C IV λ5808 got indeed better, the overall fit worsens. We adopted the model spectrum that throughout the covered spectral range provided the best fit.

Note further that the argumentation for the spectral degeneracy refers to dense atmospheres with $\log R_t \leqslant 0.6$ which applies only for the hottest stars in the cold star group.

The hot group of stars might be WC that did not encounter a radius inflation. Notable is that all of them show signs of an advanced evolutionary state. In previous analysis for galactic WR stars, only the WO stars reached a similar temperature regime

Having all those points in mind, we adopt our results for the upcoming discussion as is. Note that the sample of WC stars analyzed here is small. All derivations and relations based on our results are low number statistics and have to be treated with the appropriate caution.

9.1 The evolutionary state of the sample stars

The evolution of WR stars is highly uncertain and debated. Therefore, we compare our results to evolutionary models of Ekström et al. (2012) and Eldridge & Stanway (2009). Other evolutionary models commonly used for massive stars such as those from Brott et al. (2011) are only calculated for pre-He burning phases.

9.1.1 The WC sample in an HRD

In Fig. 44, we compare our results to the tracks of Ekström et al. (2012) for stars with and without rotation in an HRD. It is evident that there is a mismatch between our results and the tracks. The color coding of the tracks gives the assumed evolutionary state of star along the tracks based on the surface abundances of CNO and H. The hottest stars in our sample seem to have temperatures appropriate for an WO star.

[20] Which is also called the *WR radius problem*

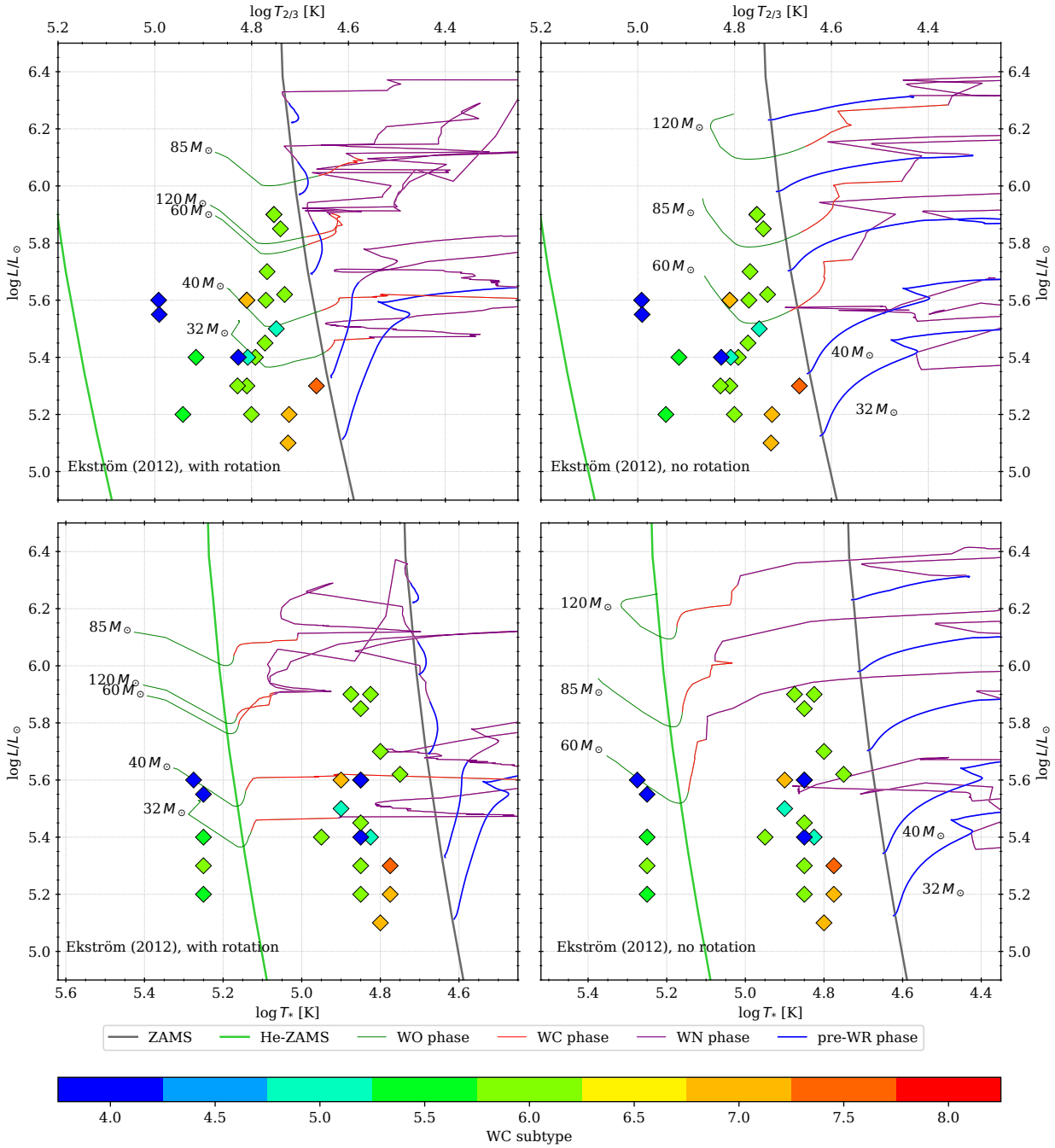

Figure 44: *HRD of the analyzed WC stars in M 31. Our sample stars are plotted according to their luminosity and $T_{2/3}$ and T_* in the upper and lower panel, respectively. The color coding of the symbols indicates the spectral type of the stars. Overplotted are the evolutionary tracks of Ekström et al. (2012) for rotating (left) and non-rotating (right) stars. The color coding of tracks indicates the individual evolutionary phases a star passes through. These phases are determined by the given surface abundance of CNO and hydrogen as: $X_H > 0.5$ (pre-WR), $X_H < 0.5$ (WN), $X_C > 0.1$ (WC), $X_O > 0.1$ (WO), all given in mass fraction.*

The only star for which there is a little resemblance to a WO stars is M 31 WR 54 with its strong lines and increased oxygen abundance. Despite of that, the spectrum of WR 54 is still one of a WC star. For all the other stars in this temperature range, the oxygen abundance is lower and they do not show any similarities to a WO.

The regime where we would expect WC stars according to the tracks is exactly the region between our two groups of stars. If we look at the HRDs with $T_{2/3}$, the WC region is again not populated, but this time all stars seem to be too hot.

Additionally, a handful of sample stars appears to be underluminous. No evolutionary track reaches the WR phase and regions hotter than the MS for low masses ($< 30 M\odot$). This is also a known issue and

indicates a problem with the evolutionary tracks. The evolutionary models overpredict the mass threshold for a WR star.

Interesting to note is that according to the tracks for non-rotating stars the threshold for initial mass to enter the WR phases is $\approx 50\,M_{\odot}$. This leaves clearly populated regions by our sample without an evolutionary track that reaches there. This might be an indication for the importance of the inclusion of rotation to the models. One may also argue that the remaining mismatch between the tracks with rotation and our sample results from an underestimated rotation for the tracks. This is supported by the clear signs of strong rotation in our models.

To sum up, we have to say that the similarities between the evolutionary models and our derived parameters are small.

9.1.2 Comparison of derived stellar parameters to evolutionary models

The spectral type is only a proxy for the spectral appearance of the stars. We have seen that stars with similar spectral types might be widely different in their nature. Therefore, we compare the stellar parameter to the evolutionary model predictions by Eldridge & Stanway (2009) and Ekström et al. (2012). For the latter we adopt the models for rotating stars, while the Eldridge & Stanway (2009) tracks do not account for rotation.

In Fig. 45, we compare the derived current stellar masses to the predicted current masses by the evolutionary models. The agreement is obvious. Note that the masses are not directly estimated from the model fit but base on the mass-luminosity relation of Langer (1989) for a helium star. Notable is that the sample masses appear to be slightly higher than the prediction of both sets of evolutionary models.

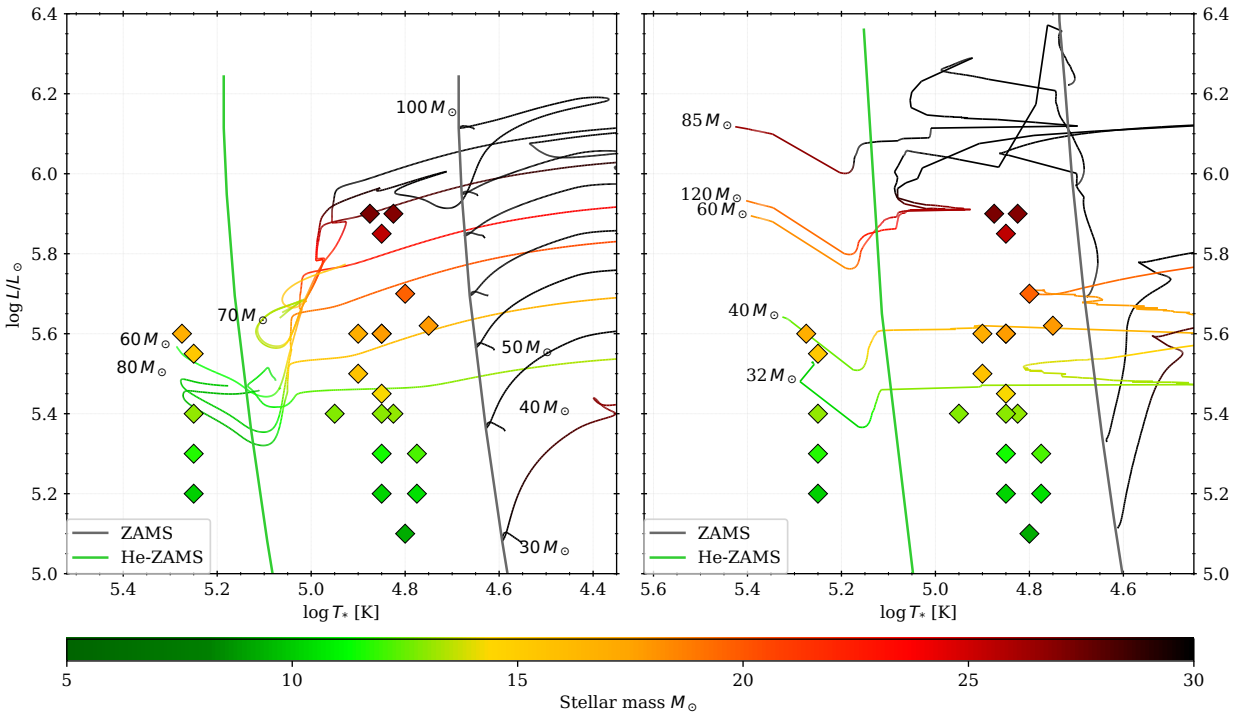

Figure 45: *HRDs of the analyzed WC stars in M31. Our sample stars are plotted in the left and right panel, each. Overplotted are the evolutionary tracks by Eldridge & Stanway (2009) and Ekström et al. (2012) left and right, respectively. The color coding of the symbols indicates the derived mass for the sample stars and the color coding of the tracks gives the mass of the models along the tracks.*

A different picture is painted when comparing the surface metalicity Z (in Fig. 46 displayed with the helium abundances Y with $1 = Y + Z$). While the overall trend that the hotter more evolved stars show a higher metal abundance (mostly carbon) is given by evolutionary models as well as by our sample, the process of enrichment in carbon is widely different. The stars show carbon at much lower temperatures compared to the predictions of the tracks. This is an expected result as we have seen already in Fig. 44 that the WC phase, determined mostly from the carbon surface abundance, sets in at higher temperatures in the evolutionary models.

Massive stars live a short life and the WR phases last only a few 10^4 yr. In Fig. 47, we compare the location of the sample stars in the HRD with the stellar ages predicted by the tracks. Most of the stars of

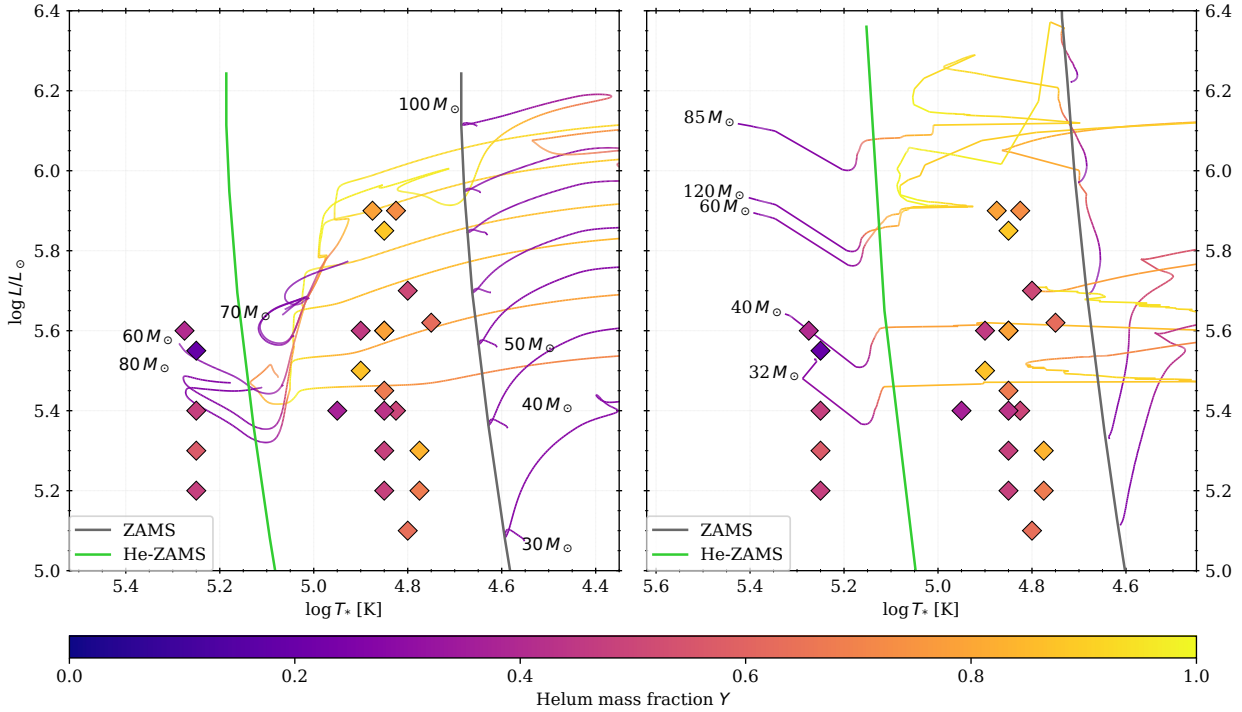

Figure 46: *Same as Fig. 45. The color coding indicates the derived mass for the sample stars and the mass of the stars along the track, each.*

our sample with $\log L > 5.4$ appear to be older than $4 \cdot 10^6$ yr with the oldest stars around $7 \cdot 10^6$ yr. For stars with $\log L < 5.4$ no estimation can be done due to the lack of evolutionary tracks that reach the region of the HRD.

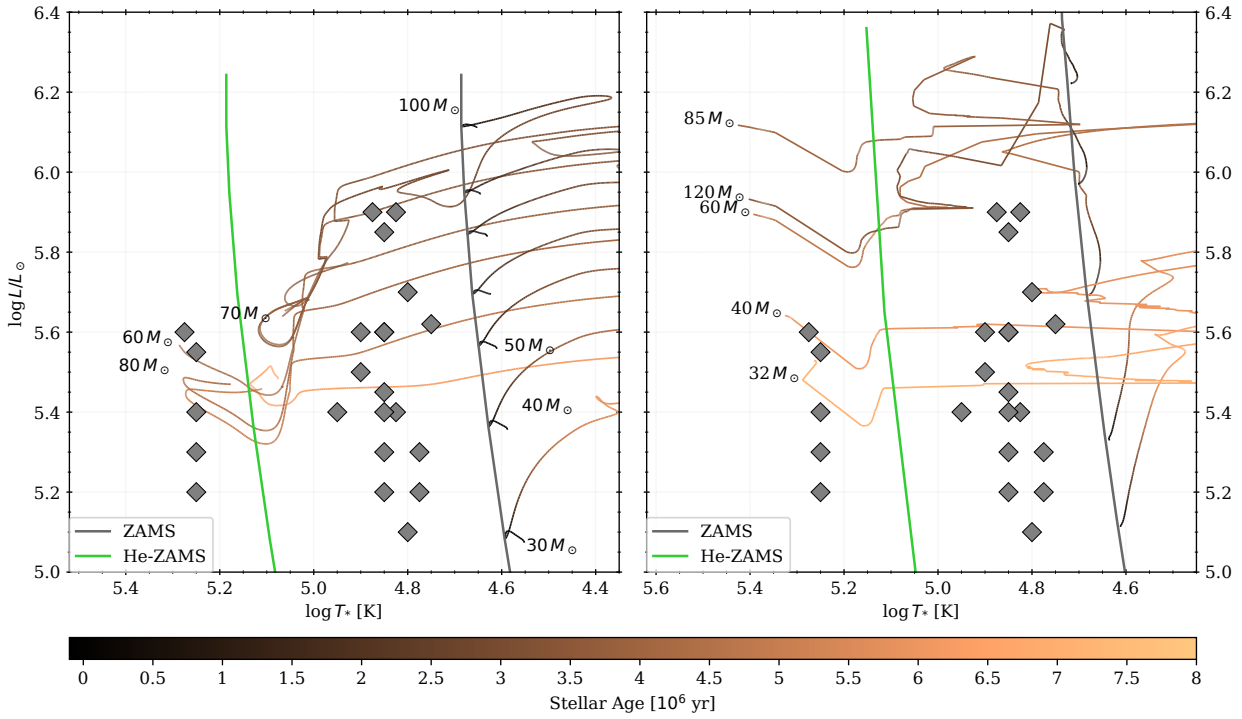

Figure 47: *Same as Fig. 45. The color coding indicates the predicted age of the stars along the track.*

9.2 The different spectral appearances of WC 6 stars

The evolutionary models do not provide the all the insights we desire due to the above mentioned reasons. Therefore, we investigate the results itself more into detail. Thereby, we focus on appearing patterns, expected and unexpected ones, as well as obvious correlations between the individual stellar parameter. We note again that the sample size is comparably small and all results have to be treated with caution.

The WC6 stars make the largest group of the sub-types among the sample. If we compare them to each other we can notice that they show differences among each other.

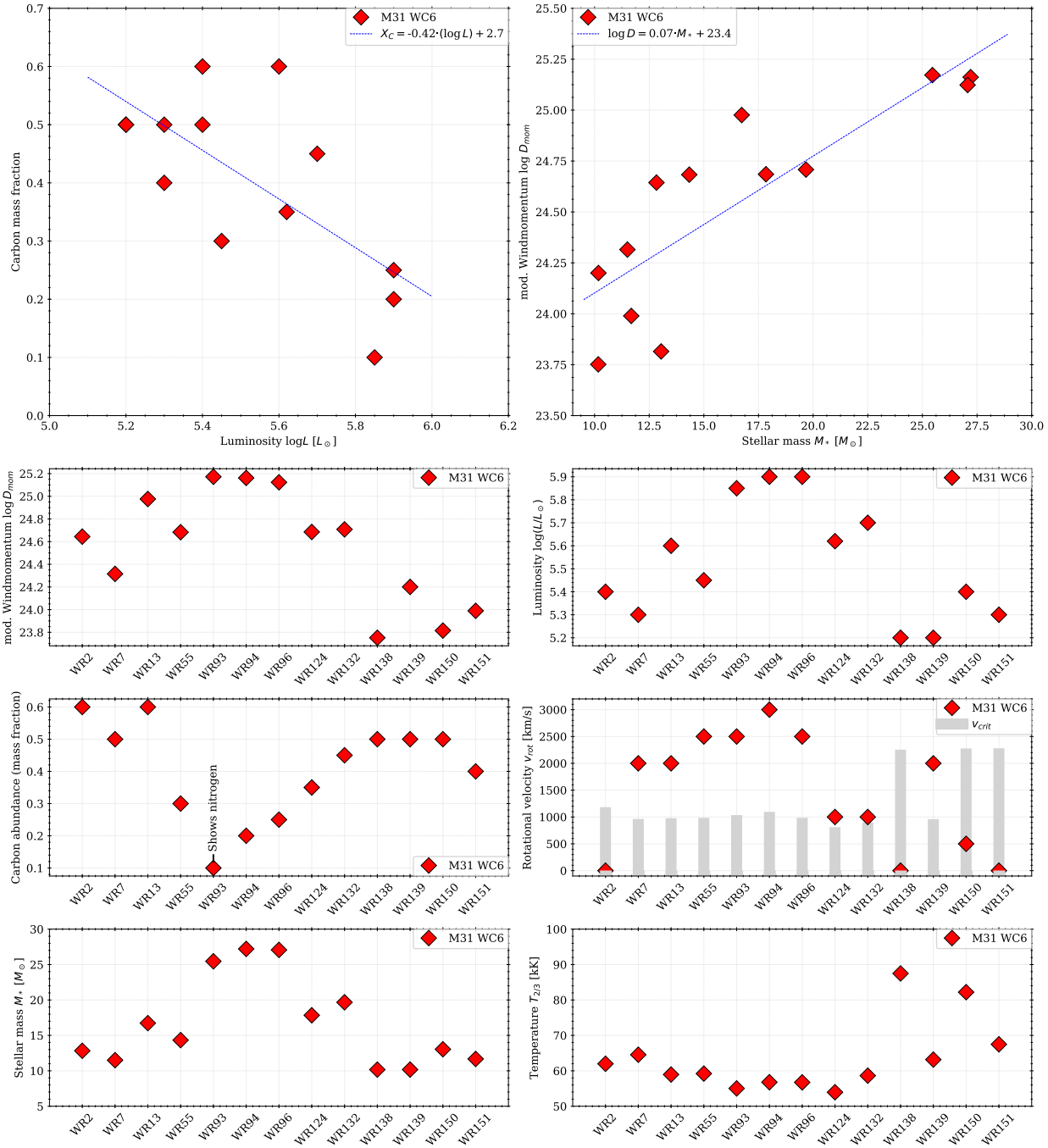

Figure 48: *Comparison of the results of the WC6 stars (red diamonds) for selected stellar parameter as indicated. The upper panels shows a relation between the carbon abundance and the luminosity (left), and between the stellar mass and the mod. wind momentum, while the blue line depicts a least square fit to the data.*

Originally, it appeared that the stars separate into two distinct groups. Whereby one featured high luminosities, fast rotational velocities, low carbon abundances and a very strong wind, while the other showed the opposite. This separation vanished over time with the ongoing the fitting process, but a distinction is still slightly visible. In Fig. 48, we depict selected derived parameters for all WC6 and WC5-6 stars in the

sample. The stellar parameters show a large scatter and some stars show some striking similarities (such as WR 93, 94, and 96). The observed parameters support what we found already for the WC4 stars. Stars of similar spectral differ widely in their spectral appearance and their parameter. What can be seen in Fig. 44 is also that with increasing brightness, the stars get slightly colder. The correlation is weak but noticeable.

An interpretation of the presented results is that the WC6 stars represent WR stars of different masses which caused the apparent differences. This is in fact not surprising as we would expect different stellar parameter for stars of different mass. Also the stronger wind for the more massive stars as expected (upper right panel of Fig. 48). An additional information seen here is that the stars appear as a certain WC subtype at different phases of their evolution, when we adopt the carbon abundance as indicator for their evolutionary state (upper left panel of Fig. 48). While fainter and lower mass stars reach the WC6 phase later, when they have evolved further, the more massive stars are brighter and might enter the WC phase already as WC6.

While this picture is reasonable for stellar evolution, it also states again that the spectral sub-type of a WC does not provide reliable calibration for the stellar parameters and evolutionary state.

9.3 A comparison to previous work on Galactic WC stars

How do our results match to the findings of previous work done on WCs in particular and WR in general? The study conducted in this thesis is one in a number of studies on WC stars. But it is the first one focusing on WC stars in M 31. The WC stars most similar to those are the galactic WC's due to the similar abundances of the host galaxies. Therefore, we compare our findings in Fig. 49 with the results of Koesterke & Hamann (1995), Hamann et al. (2003), Barniske (2008), and Sander et al. (2012) for galactic WCs and Crowther et al. (2002), Shenar et al. (2016), and Grafener et al. (1998) for LMC and SMC WC and WO stars. We see that our results, in principle, align very well with those findings regarding the occupied parameter space. With the difference that all those studies, with exception of Hamann et al. (2003), found a more or less tight correlation between spectral type and stellar temperature. This correlation is strongest in Sander et al. (2012). The earlier types are generally hotter. In our results, we do not find a similar correlation. Most of the stellar parameter appear randomly scattered without a correlation to the spectral type.

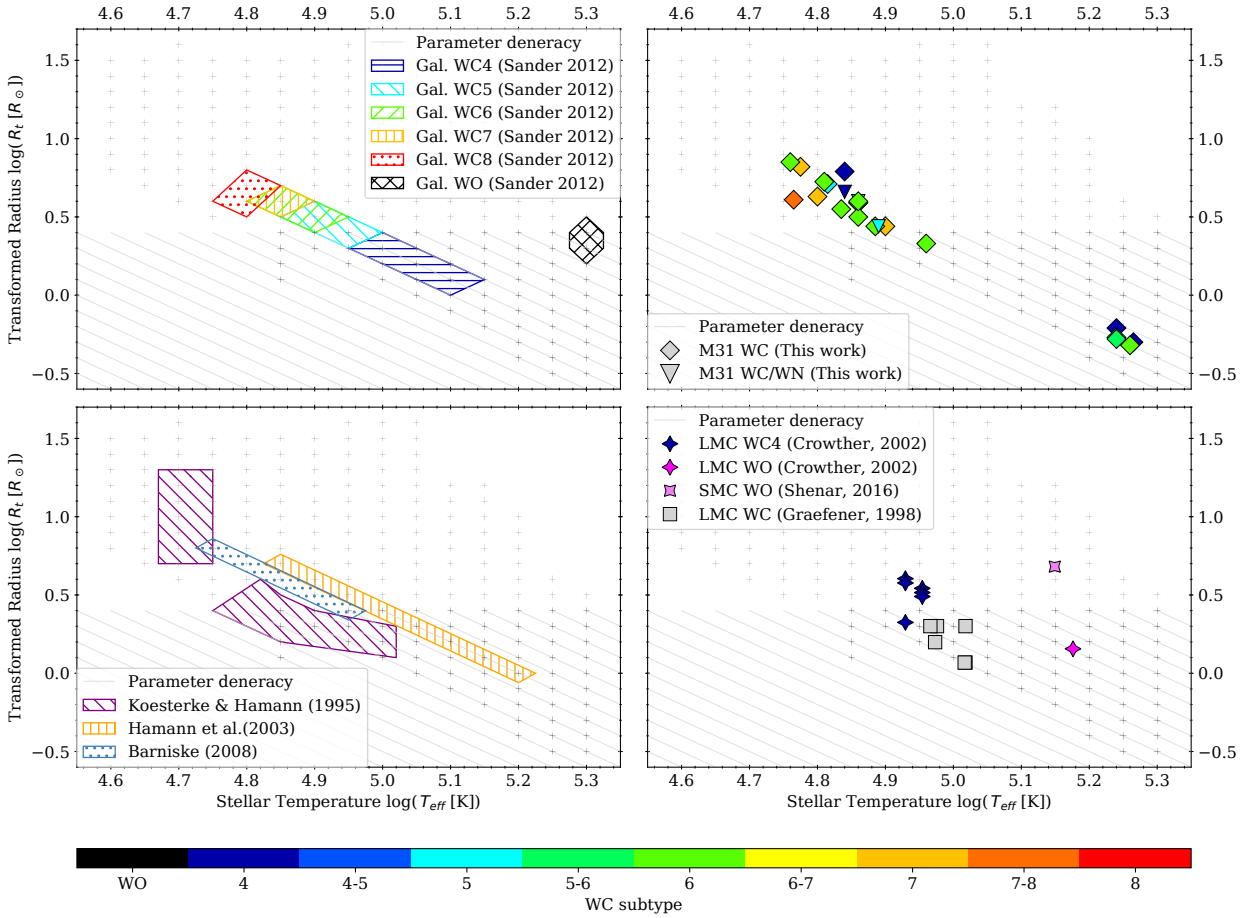

Figure 49: *Original model grid where each + represents a grid model. The degeneracy regime and grid models within it are indicated.*
Upper left panel: *Results of the analysis of the galactic WC and WO stars by Sander et al. (2012). For visibility reasons, only hatched areas are shown that depict where stars of a certain spectral type can be found. The color coding indicates the spectral type.*
Upper right panel: *Results of this work. The color coding denotes the observed spectral type.*
Lower left panel: *Results of Koesterke & Hamann (1995), Hamann et al. (2003), and Barniske (2008) for galactic WC stars. The color coding does not represent the spectral type. For visibility reasons, only hatched areas are shown.*
Lower right panel: *Results of Crowther et al. (2002), Shenar et al. (2016), and Grafener et al. (1998) for LMC WC and WO stars as well as the only SMC WO star.*

It cannot be concluded, why the correlation between spectral type and temperature emerged in other work but not in this. One issue might be that all those previous analyses were carried out less sophisticated (e.g. they did not include an adjustment of the carbon abundance) or where done with older and less sophisticated versions of the stellar atmosphere codes. We do see that the fit quality reached in this work is superior to those in previous analyses.

9.4 Stellar Rotation

A problematic, important, and interesting finding in this spectral analysis is that quite a number of stars rotate faster than their break up velocity. It is problematic due to the fact that a star that would rotate overcritical disintegrates itself over time. As the star is obviously still there, the disintegration happens either very slowly (which is unlikely) or the rotational velocities are strongly overestimated here. Interesting is the fact that fast rotation, even if it not exceed the critical velocity, has an impact on the evolution of a star. This impact can be seen for the wind driving, which has to overcome a lower, effective gravity due to centrifugal forces and can result in higher mass-loss rates, in an angular momentum loss of the star over its life time, and in increased mixing processes inside the star that are driven by the rotation. Therefore, the rotation of a star needs to be accounted for.

We do not want to go into the details here of the impact of strong rotation on the stars itself. This has been done elsewhere extensively and would exceed the scope of this thesis. Instead, we will investigate the limitation of spectroscopy in determining the rotation of WR stars. For this reason we will quickly repeat the important points of how stellar rotation is treated in the present models.

1. The stellar atmosphere models are spherical symmetric and usually do not account for rotation in the main iteration.

2. In PoWR, the formal integral can account for rotation by calculating the projected radial velocities along the line of sight for each impact parameter.

3. In the formal integral, the stellar atmosphere is assumed to be spherical symmetric.

4. It is distinguished between two regimes. A co-rotating part is assumed between the photosphere and $R_{\rm corot}$, with $v_{*,\rm rot}\sin(i)$ the velocity at the photosphere, and $v_{\rm rot}\sin(i)$ the velocity at $R_{\rm corot}$ and a linear increase in between. For radii $> R_{\rm corot}$, the rotational velocity decreases according to angular momentum conservation. Figure 50 displays this behavior.

5. $v_{\rm rot}\sin(i)$ and $R_{\rm corot}$ are treated as free parameter in the formal integral. $v_{*,\rm rot}\sin(i)$ can be calculated via Eq. (11).

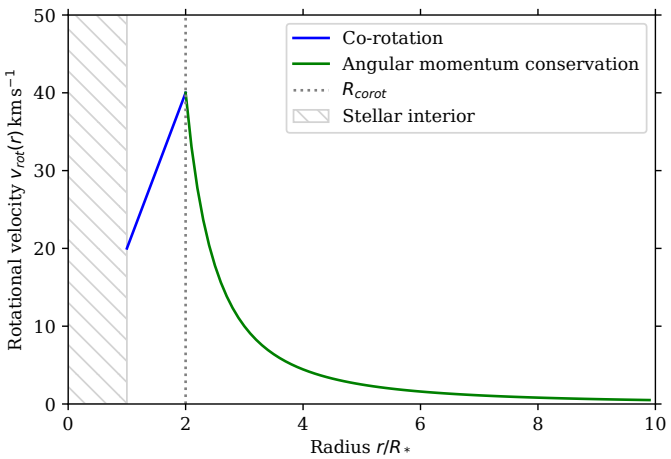

Figure 50: *Radial velocity distribution in the stellar atmosphere with $R_{corot} = 2R_*$ and $v_{rot}\sin(i) = 40\,km\,s^{-1}$. The blue line describes the co-rotating part of the atmosphere with the linear increase of v_{rot} and the green line depicts the $1/r$ decrease according to angular momentum conservation. $v_{*,rot}\sin(i)$ can be calculated with Eq. (11)*

The curve displayed in Fig. 50 shows that lines that form at different radii are affected by rotation differently. This is also found in our analysis (see Sect. 7.2.9). We adopted $R_{\rm corot} = 1.1\,R_*$ and obtained a striking agreement for the varying impact of rotation on the individual features in the spectra. But it is also obvious that lines originating at different radii originate at the same rotational velocity. Already Shenar (2013) noticed that different combinations of $R_{\rm corot}$ and $v_{\rm rot}$ can lead to similar results. They also found that for $1 \leqslant R_{\rm corot} \leqslant 10$, the changes in the spectral appearance are significant while the for $R_{\rm corot} > 10$ almost no changes are visible due to rotation.

Therefore, we want to examine the behavior of the spectral features under different rotational parameters. Due to time constraints, we do this exemplary for M 31 WR 94 in the spectral region between 4000 Å and 6000 Å which has shown to be the best indicator for the rotation here. We adopted the final model for WR 94 and calculated a grid of synthetic spectra with $R_{\rm corot} \in (1.0, 1.5, 2.0, 2.5, 3.0, 4.0, 5.0, 10.0)\,R_*$ and $v_{\rm rot} \in (1000, 2000, 3000)\,{\rm km\,s^{-1}}$. Figure 51 shows an excerpt from the synthetic spectra for different parameters. It is obvious that changes in $R_{\rm corot}$ and $v_{\rm rot}$ cannot lead to a straight forward solution as the

changes of the lines seem to contradict each other. Outstanding in this regard is the merging of C III λ5969 and C IV λ5808 that occurs for $R_{\rm corot} > 5.0\,R_*$. Further can be noticed that with increasing $R_{\rm corot}$, the emission peaks of various lines shift to longer wavelength (cf. diagnostic pair and C IV λ4859). This effect gets stronger with larger $v_{\rm rot}$.

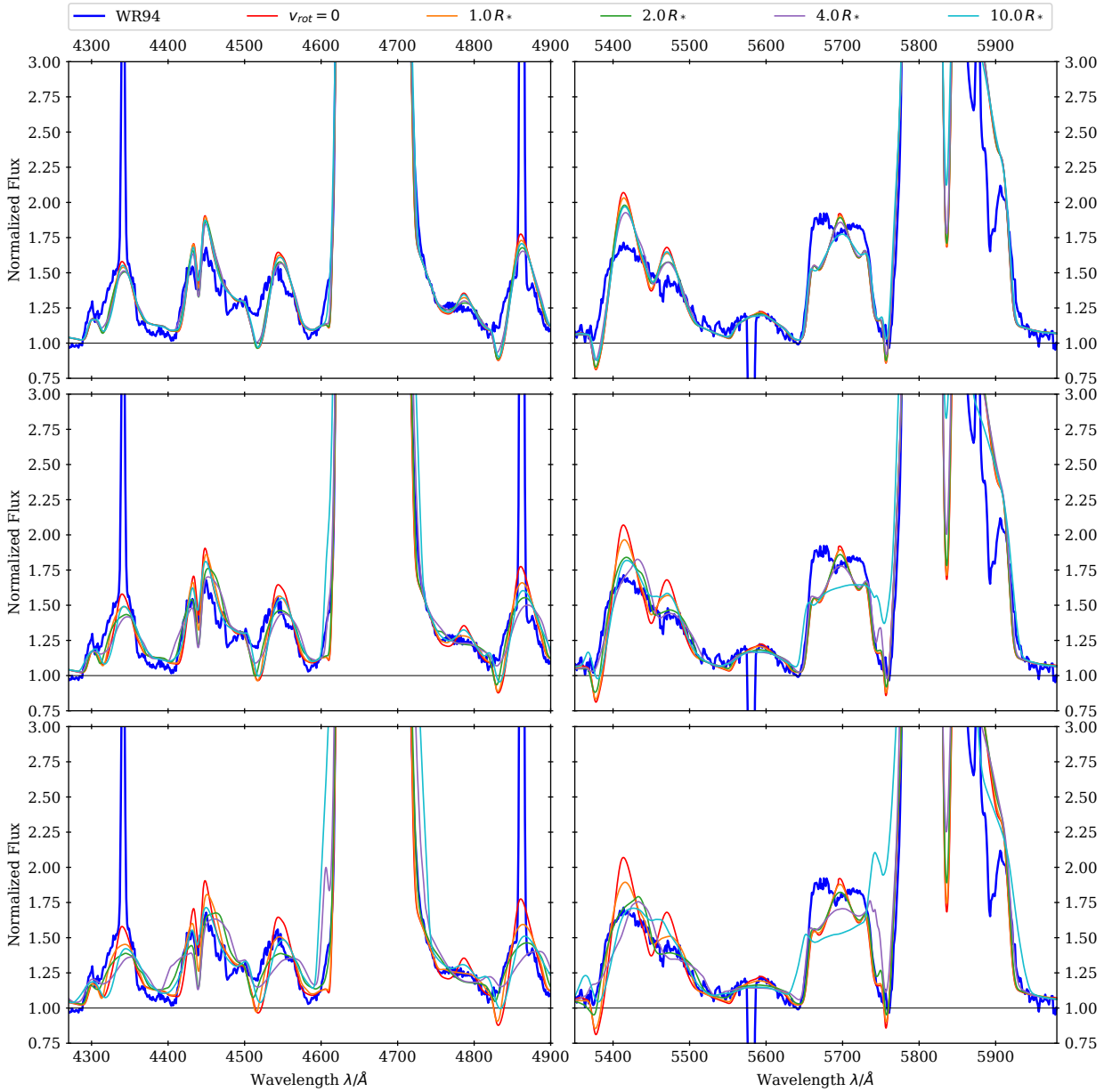

Figure 51: *Series of model spectra compared to WR 94 (solid blue line). The rotational velocities are 1000 km s^{-1}, 2000 km s^{-1}, and 3000 km s^{-1}, in the upper, middle, and lower panels, respectively. The co-rotation radius is indicated. The red solid line depicts a model without rotation in each plot.*

Even with a rather inconsistent behavior under the change of $R_{\rm corot}$ and $v_{\rm rot}$, we can say that the agreement is best for $R_{\rm corot} = 4$. If this trends holds for all stars, the rotational velocity $v_{*,\rm rot}$ at the stellar photosphere is almost quartered and therefore, all stars would rotate below critical again. Note that those estimates for $R_{\rm corot}$ are lower than the estimated $R_{\rm corot} \backsimeq 10\,R_*$ as found by Shenar (2013).

We can also go the opposite way and adopt a reasonable rotational velocity $v_{*,\rm rot}$ for a fast rotating star and adjust $R_{\rm corot}$ to fit the stellar spectrum. Again, we adopt the spectrum and final model found for M 31 WR 94. According to Eq. (10) and our derived parameters for WR 94, the critical velocity for this star is $v_{\rm crit} \approx 1000\,{\rm km\,s^{-1}}$. As there are no studies concerning the rotation of WR stars, we adopt what is known for their direct precursors, the OB stars. Fast rotating stars are denoted as Be or Oe due to the emissions lines in their spectra caused by a decretion disk. Rivinius et al. (2013) displayed the measured rotation rates for galactic Be stars and those widely show a ratio between $v_{*,\rm rot}$ and $v_{\rm crit}$ of ≈ 0.75. If we assume WR 94 to show a similar ratio, we find a rotational velocity of the photosphere of $v_{*,\rm rot} = 750\,{\rm km\,s^{-1}}$. We now tune

$v_{\rm rot}$ such that with a given $R_{\rm corot}$ we always obtain $v_{*,\rm rot} = 750\,{\rm km\,s^{-1}}$. Table 13 lists the adopted parameter calculated according to Eq. (11). As can be seen, the previously found $R_{\rm corot} = 4$ is also present here with the adopted $v_{\rm rot} = 3000\,{\rm km\,s^{-1}}$.

Table 13: *R_{corot} and v_{rot} pairs adopted for a comparison of spectra for rotating atmospheres with different R_{corot} while $v_{*,rot} = 750\,{\rm km\,s^{-1}}$ is kept constant. v_{rot} is calculated according to Eq. (11).*

$R_{\rm corot}$ R_*	$v_{\rm rot}$ km s^{-1}	$R_{\rm corot}$ R_*	$v_{\rm rot}$ km s^{-1}
1.0	750	4.0	3000
2.0	1500	5.0	3750
3.0	2250	10.0	7500

In the upper panel of Fig. 52, the adopted rotational velocity profiles are displayed and compared to the wind velocity field and the particle density, both extracted from the underlying stellar atmosphere model. The lower panel in Fig. 52 shows the radial distribution of the emission calculated according to Hillier (1987). The showed lines are such selected that the different responses to the rotation are shown.

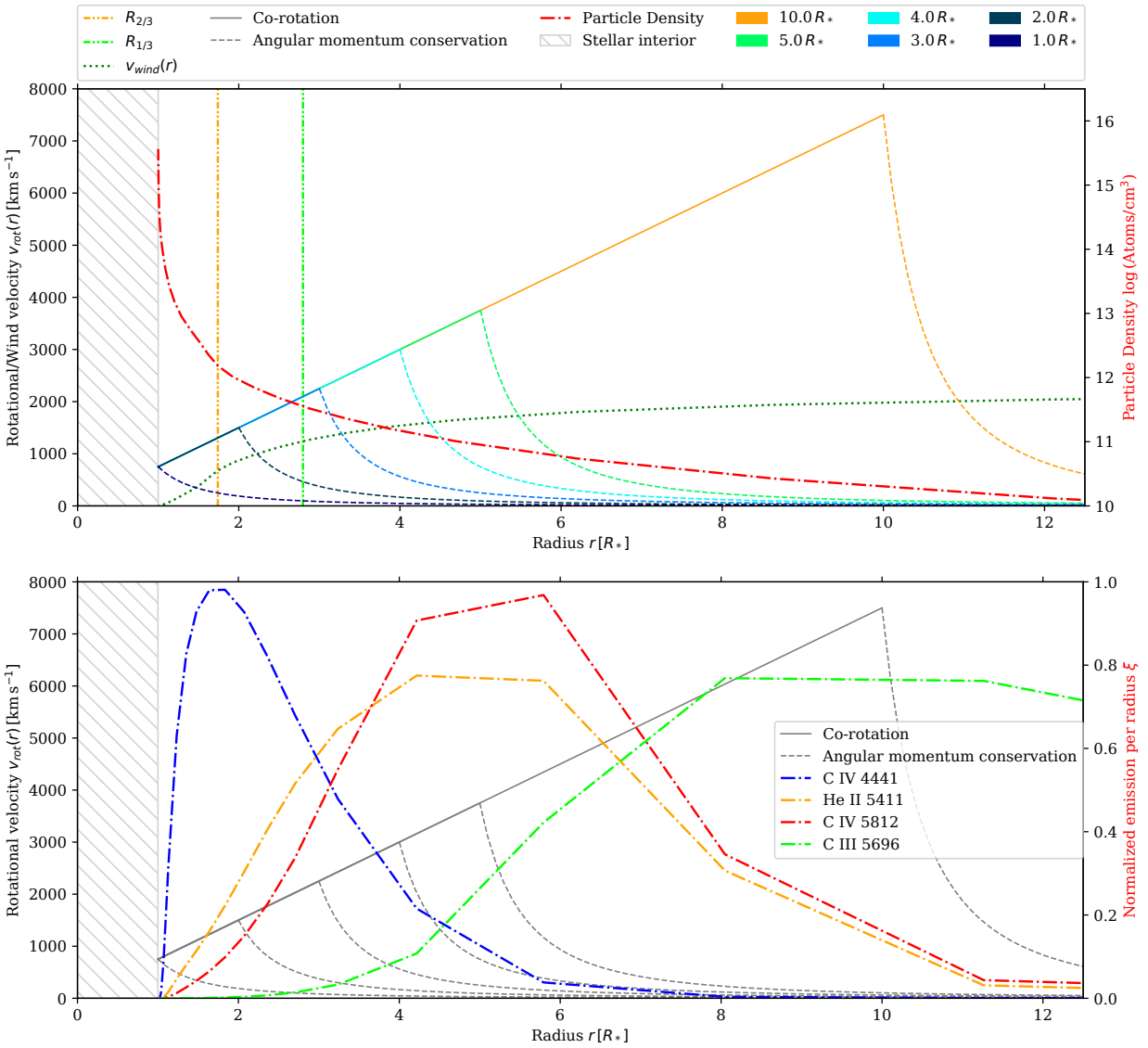

Figure 52: *Adopted rotational field of WR 94.*
Upper panel: *Radial distribution of wind velocity field (green dotted line) and particle density (red dash-dotted line) compared to assumed rotational velocity fields (color coded solid and dashed lines) with their parameter given in Table 13.*
Lower panel: *Normalized emission per radius ξ as defined by Hillier (1987) for four lines:* C IV *λ4441 (blue dash-dotted line),* He II *λ5411 (orange dash-dotted line),* C IV *λ5812 (red dash-dotted line), and* C III *λ5696 (green dash-dotted line).*

The regions where the lines form correspond nicely to our experience that C IV λ4441 is strongly affected, He II λ5411 and C IV λ5812 are mildly affected, and C III λ5696 is not affected by rotation. It is clearly visible that the adopted $R_{\rm corot}$ changes significantly which lines are effected by which rotational velocity as the lines originate at different densities and temperatures and therefore radii in the wind. This can also be seen when we calculate the emergent spectra according to those parameters (see Fig. 53). Again, $3R_* \leqslant R_{\rm corot} \leqslant 4R_*$ reveal the best agreement with the observation, while $R_{\rm corot} \geqslant 5$ are highly inconsistent with the observations.

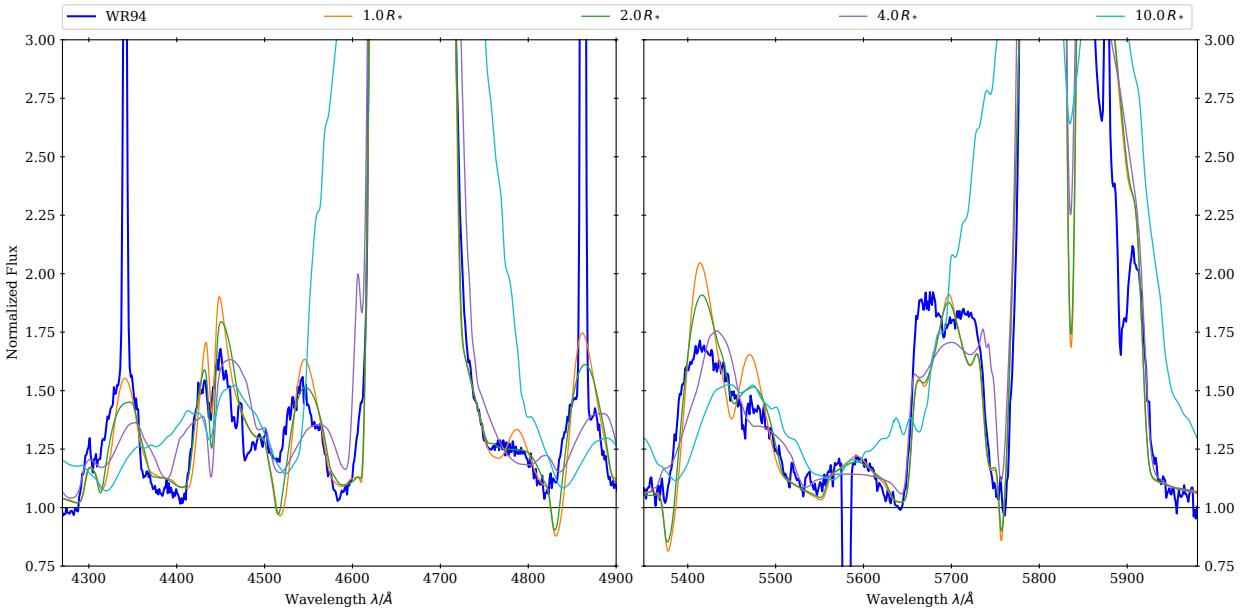

Figure 53: *Same as Fig. 51. This time with R_{corot} as indicated by the color coding while $v_{*,rot} = 750\,km\,s^{-1}$ is kept constant. v_{rot} is calculated according to Eq. (11), see Table 13.*

Note that for $R_{\rm corot} \geqslant 5$ the before mentioned (cf Sect. 7.8.2) *church steeple* line shapes for C III λ5696 show more agreement with the flat top profile observed. But for larger $R_{\rm corot}$, the lines of C III λ5696 and C IV λ5808 begin to merge which is not observed in any spectrum.

Note further that individual lines like O VI $\lambda\lambda$5270−92 are barely affected by rotation at all, independently of the adopted $R_{\rm corot}$. This is also in agreement with the observation.

It is obvious that $R_{\rm corot} \leqslant 3$ are also inconsistent with the observation, as the effect of rotation is not notable at all. There has to be at least a certain co-rotating region of the wind. This leaves the question of how a star can be co-rotating up to this radius. Similar to the solar wind, it is assumed that the wind is co-rotating due to a strong magnetic field of the star (cf. Parker spiral, Parker 1958). Letting aside the question with the regard to the origin of the magnetic field in a massive star whose envelop is radiative, we want to estimate the magnetic field strength B_* required to ensure the derived co-rotation. For this, we follow a simplified model described by ud-Doula & Owocki (2002).

To get a lever on $R_{\rm corot}$ we adopt $R_{\rm corot} \approx r_A$. The *Alphvén* radius r_A describes the radius at which the energy in the magnetic field equals the kinetic energy in the wind

$$\eta(r_A) = 1, \tag{12}$$

with η being the *magnetic confinement parameter*

$$\eta_* = \frac{B^2 R_*^2}{\dot{M} v_\infty} \tag{13}$$

whose radial dependency can be described like

$$\eta(r) = \frac{B^2}{8\pi} \cdot \frac{2}{\rho(r) v_\infty^2} = \eta_* \left[\frac{(r/R_*)^{2-2\sigma}}{(1 - R_*/r)^\beta} \right]. \tag{14}$$

The last step accounts for the description of the velocity field as a β-law, see Eq. (7). Furthermore, σ describes the radial decay rate of the magnetic field which is assumed to be $\sigma = 3$ for a radial magnetic field in a stellar wind which is the better description (e.g., Gayley & Ignace 2009)[21]. From this approximation,

[21] For a dipole field, $\sigma = 2$.

we can obtain a rough estimate for the magnetic field strength B required for found $R_{\rm corot}$ using Eq. (12) and (13) in (14). We obtain with $\beta = 1$ and $\sigma = 3$:

$$B = \sqrt{\frac{\dot{M} v_\infty}{R_*^2} \left(1 - \frac{R_*}{R_{\rm corot}}\right) \left(\frac{R_{\rm corot}}{R_*}\right)^2} = \sqrt{\frac{12 \dot{M} v_\infty}{R_*^2}}, \tag{15}$$

where the last step accounts for $R_{\rm corot} = 4$. Plugging in the parameter for WR 94 yields the required magnetic field for co-rotation to be

$$B = 7.4\,\mathrm{kG} \tag{16}$$

at the stellar surface. For a WR star, we cannot measure the magnetic field at R_*. However, $R_{2/3}$ is a more appropriate comparison for the observed magnetic field. With Eq. (15) and $R_{2/3} = 1.7\,R_*$ for the used model, we find

$$B = 2.7\,\mathrm{kG} \tag{17}$$

which is still at about one order of magnitudes higher a magnetic field compared to what was found to be present in some massive stars (Fossati et al. 2015). Therefore, this results shows a dilemma.

Two explanations for the found rotational velocities are possible, but both have their problems:

1. The WR wind does not co-rotate, or only up to a very small $R_{\rm corot}$. This explanation on the upside does not require an overly strong magnetic field to force the wind to co-rotate. But on the downside the velocities found to be present at the stellar surface are around or even much higher than the break-up velocity.

2. The WR wind co-rotates up to large $R_{\rm corot}$. This explanation on the upside decreases the surface rotational velocity to values below the critical limit. But on the downside it requires enormous magnetic field to force the wind to co-rotate. Furthermore, one also needs to check if the linear increasing rotational velocity and the reduced stellar gravity at larger radii encounter the problem of overcritical rotation again.

However, both models for rotational velocity fields can provided a reasonable fit for the observed line shapes.

It is also interesting to estimate the centrifugal force and acceleration that would come with a surface rotation of $0.75 v_{\rm crit}$. From classical mechanic follows for the centrifugal acceleration $a_{\rm cf} = \frac{v^2}{r}$, which gives at the stellar surface ($r = R_*$)

$$\log(a_{\rm cf}) = 4.18\,\mathrm{cm/s^2} \qquad \log(a_{\rm cf}/g) = -0.24$$

with $\log g = 4.42$ for the present model. Furthermore, we can extract from the model the present acceleration at the inner boundary, i.e. R_*,

$$\begin{aligned} \log((a_{\rm rad} + a_{\rm press})/g) &= 1.18, \\ \log((a_{\rm mech} + g)/g) &= 0.21 \cdot 10^{-3} \approx 0 \end{aligned}$$

where $a_{\rm rad}$ is the radiative pressure and $a_{\rm mech}$ the acceleration of the wind according to the pre-described velocity field.

We can see that at the inner boundary, the centrifugal force alone compensates about 57% of the gravitational force. But the total acceleration is still dominated by the radiative pressure which is mostly due to continuum radiation. How about the radial distribution? The rotational velocity increases linearly outwards and then radiative pressure from the continuum decreases strongly. In Fig. 54, we display the radial distribution of the acceleration caused by the rotation. It is obvious that the impact of rotation is not overwhelming, but it outweighs the radiative acceleration up to the co-rotation radius. Therefore, the effect should not be neglected when calculating hydrodynamic models.

Note that all of the previous discussion based on the assumption that a two component rotational velocity consisting of a co-rotating and an angular momentum conserving part is a valid approximation. Our approximation also leaves out any deformation of the star due to the fast rotation. A more detailed analysis of this problem is beyond the scope of this work but is motivated by the clear signs of strong rotation found here.

It is also possible that the observed line shapes are caused by a different mechanism. With the adopted model for stellar rotation, we can explain the observed line shapes to a reasonable extend. But it is also possible that there is a different mechanism that only mimics the effect of rotation. However, such a process is not know yet.

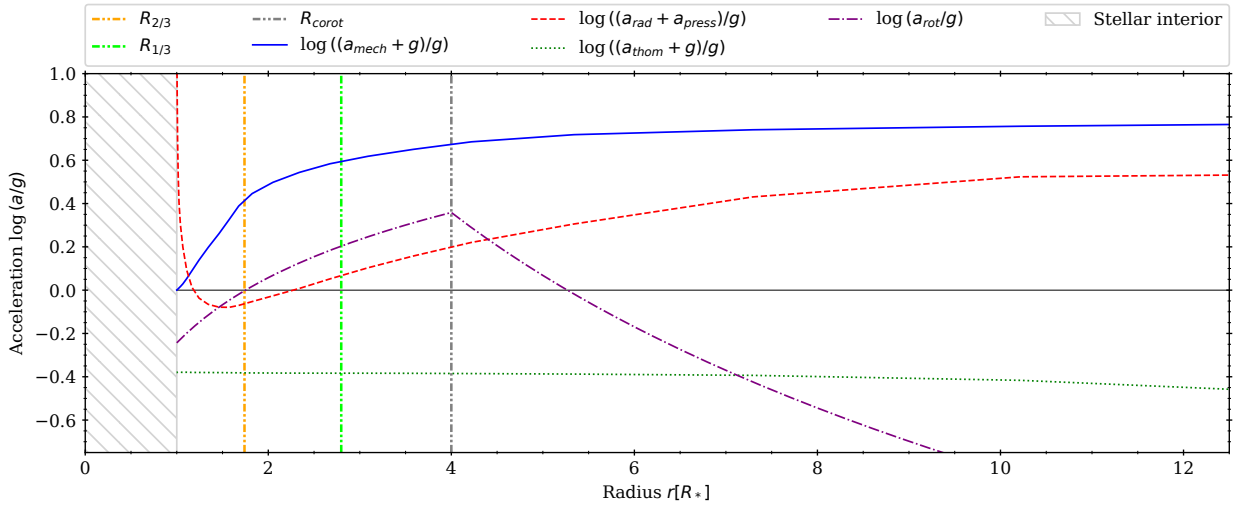

Figure 54: *Radial distribution of the governing forces to determine the wind velocity field. All are normalized to the surface gravity g. a_{mech} denotes the acceleration required for the adopted wind velocity field, a_{rad} shows the acceleration due to the radiative field (continuum+lines), a_{thom} is from the Thomson-effect on free electrons, and a_{rot} is caused by the centrifugal forces of rotational field as described in the text with $R_{corot} \leqslant 4$. Note that the sum of the acceleration terms cannot reproduce a_{mech}.*

9.5 Correlations between individual stellar parameter

One motivation for this work was to investigate how the individual stellar parameter correlate with each other, which can help to understand the evolution of WR stars.

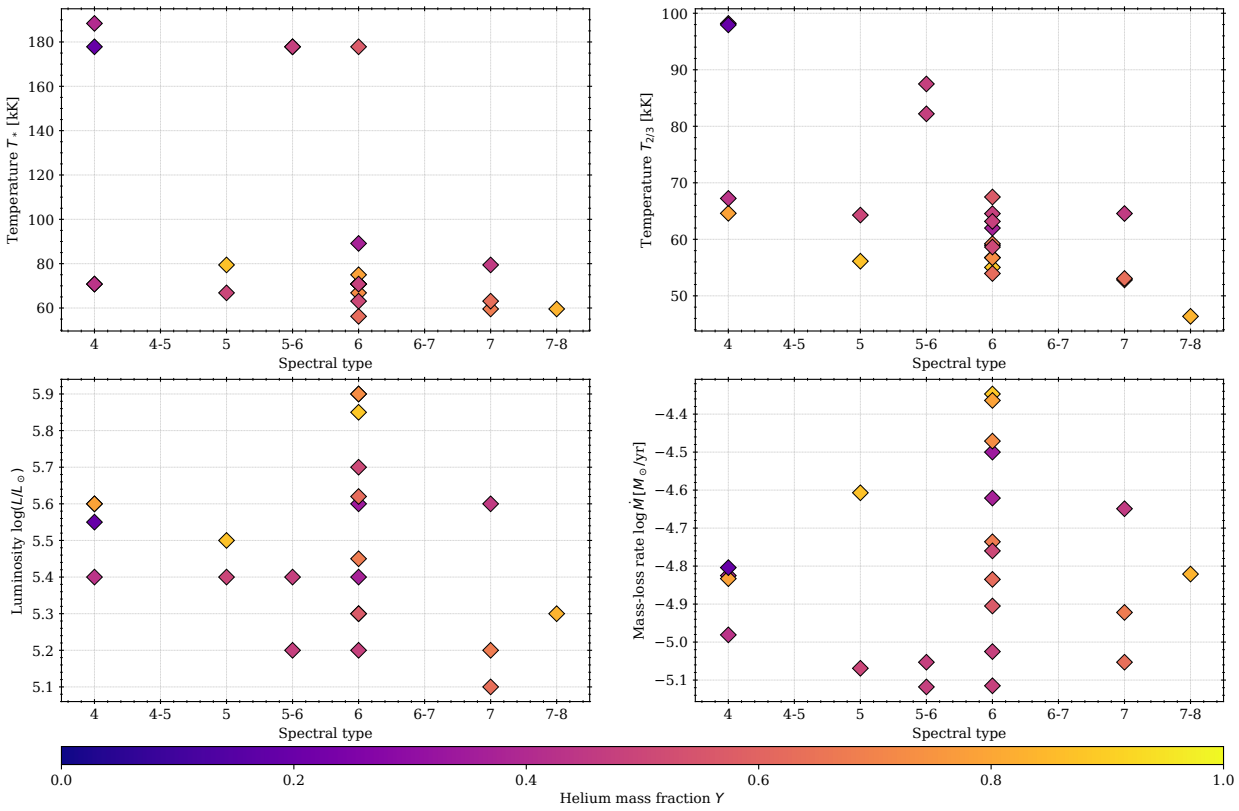

Figure 55: *Comparison of stellar parameters (as indicated) to the reported spectral type of the sample stars. The symbols mark the sample stars and their color coding refers to the observed helium mass fraction.*

First we compare the main stellar parameter temperature ($T_{2/3}$ and T_*), luminosity $\log L$, and mass-loss rate $\log \dot{M}$ to the reported spectral type. Figure 55 supports again what was already described in the Sects. 7.6, 7.7, and 9.2. There is no correlation between the spectral type and the stellar parameter. However, the upper right panel in Fig. 55 suggests that there is a correlation between temperature $T_{2/3}$ and spectral

type where the slope of a possible correlation requires the helium mass fraction as an additional parameter. For stars with a lower helium abundance, the slope is steeper. This would result in a two dimensional classification scheme for WC stars. Unfortunately, our sample is to small for a more detailed look on it. The problem with the classification scheme can also be seen when one compares the lines whose equivalent with are used for classification (see Table. 2). Especially the use of C III λ5696 is problematic. This is line is very sensitive to the strength of the wind (cf Fig. 18) but much less to temperature. A new classification scheme needs to incorporate the diagnostic pair to account for abundance effects. Another possibility is to use the equivalent width of the Bowen blend and C IV λ5808 directly, since those increase with the temperature (see Fig. 56). However, this invokes other problems. The continuum needs to be known and it cannot be used for stars that have a contaminated spectrum.

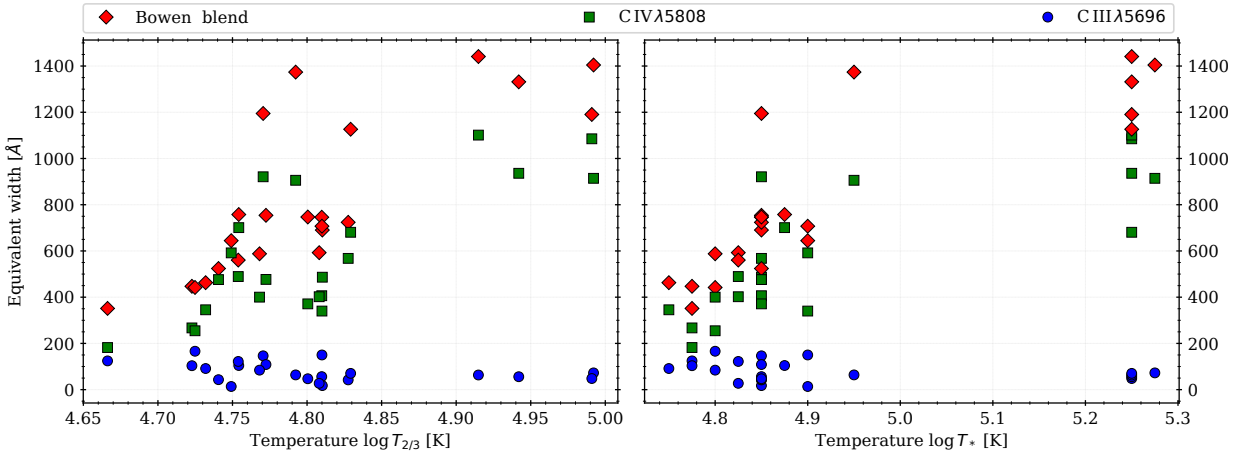

Figure 56: *Equivalent width of* C III λ5696 *(blue circles),* C IV λ5808 *(green squares), and the Bowen blend (red diamonds) measured in the observation compared to the derived temperatures in the analysis.*

But can we find a correlation of the intrinsic stellar parameter with each other? Can we draw any conclusion here? The luminosity was a key feature in our analysis as the present sample does not suffer from uncertain distances and therefore inaccurate luminosity estimations. In Fig. 57, we compare stellar temperatures and the mass-loss rates to the luminosities. For the temperature, we do not observe a clear correlation. If such would have existed, it would have already been visible in the HRDs in Fig 44. For the mass-loss rate, we do expect a correlation with the luminosity as the radiative pressure drives the stellar wind. And in fact, the upper right panel in Fig. 57 shows an increase in mass loss with increasing luminosity. An quantity used to describe the strength of the stellar wind is the modified wind momentum $D_{\rm mom}$, and which is calculated as

$$D_{\rm mom} = \dot{M} v_\infty \sqrt{R_*}. \tag{18}$$

The theory of radiatively driven winds predicts that the photon momentum correlates with momentum of the wind via

$$\log D_{\rm mom} = \log D_0 + x \cdot \log (L/L_\odot) \tag{19}$$

where $\log D_0$ and x vary depending on the spectral type and luminosity class (Kudritzki & Puls 2000). Indeed, we observe also a clear correlation (lower left panel in Fig. 57). We find

$$\log D_0 = 16.3 \qquad \text{and} \qquad x = 1.49. \tag{20}$$

Connected to this quantity is the wind efficiency parameter η, which denotes the ratio between the photon momentum L/c and the wind momentum $\dot{M} v_\infty$:

$$\eta = \frac{\dot{M} v_\infty c}{L} \tag{21}$$

Illustratively said, η indicates how often a photon on average has to be scattered (absorb and re-emitted) in the atmosphere to drive the observed stellar wind. Interestingly, when we plot the calculated η's against the stellar temperature T_* (see lower right panel in Fig. 57), we do find a correlation in double logarithmic plot for all the stars in the group with the low temperatures. Those are the stars for which envelope inflation is proposed to explain the low temperatures. If this correlation corresponds to an actual causation between those two parameters need to be proven by future studies.

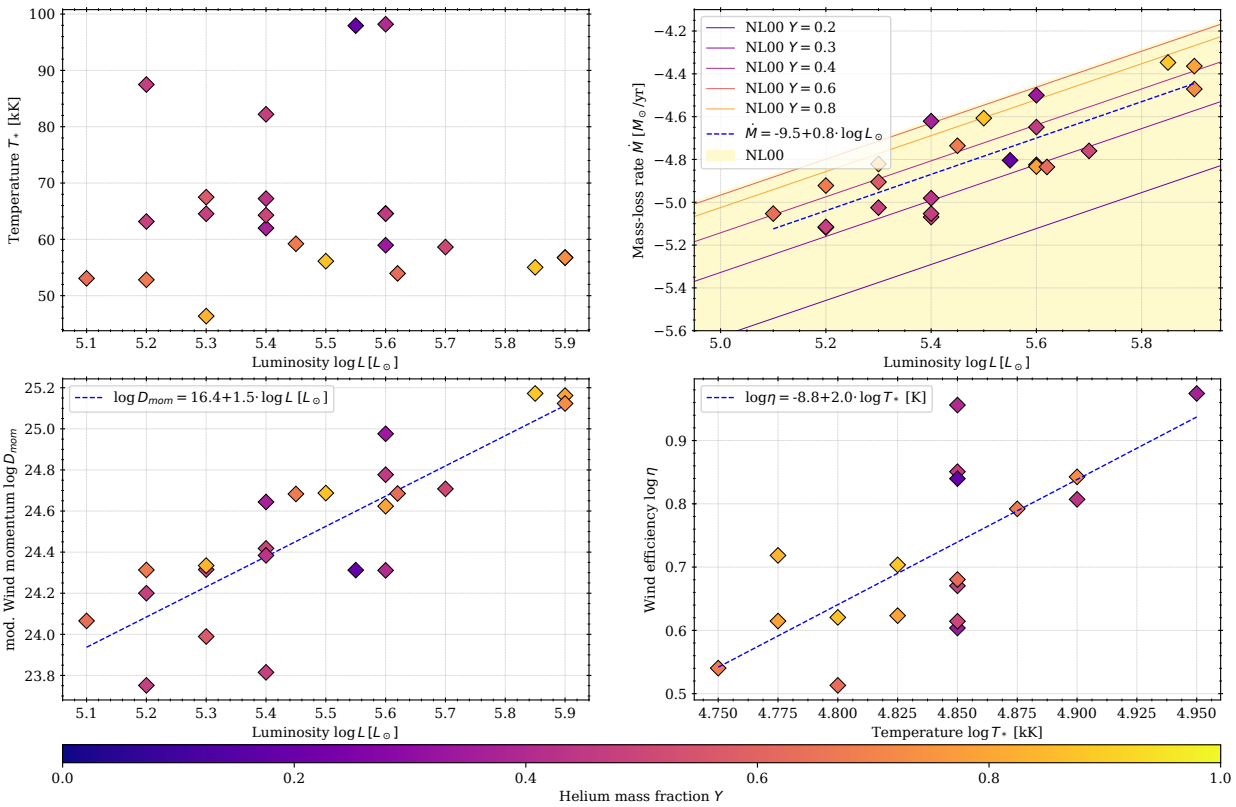

Figure 57: *Comparison of wind parameter as indicated to stellar parameter. The symbols mark the position of the sample stars and their color coding corresponds to the observed helium abundance. The dashed blue lines indicate a least square fit to the data with the equation given in the figure legends. In the upper right panel, the shaded region indicates the range of mass-loss rates that should be occupied by WC stars following Nugis & Lamers (2000) (NL00). The color coded lines display Eq. (22) for different helium abundances. The lower right panel only shows stars belonging to the colder stars in the sample which are assumed to appear colder due to envelop inflation. The correlation is not observed for the hot stars in our sample. Those are therefore not shown here.*

Furthermore, Nugis & Lamers (2000) find for galactic WC stars a relation between the mass-loss rate $\dot{M}$ and the observed luminosity $\log L$:

$$\log \dot{M} = -8.30 + 0.84 \cdot \log L + 2.04 \cdot \log Y + 1.04 \cdot \log Z \tag{22}$$

with the He mass fraction Y and the metal mass fraction Z. For our hydrogen free WC stars follows $Y = 1 - Z$. This means there is a maximum mass-loss rate which is reached by stars with 66% He mass fraction. The region where we therefore should observed WC stars is highlighted in the upper right panel of Fig. 57. We do see that all our sample stars sit below this boundary. Our sample shows a significant scattering. This, in principle can simply a metalicity effect now, as stars of different helium abundance follow a different slope. However, as can also be seen in Fig. 57, the helium abundances determined for our sample stars do not correspond to the prediction by Nugis & Lamers (2000).

Let's see how the stellar wind responds to the stellar parameter. In Fig. 58, we compare the terminal wind velocity v_∞ to stellar parameter. While there seems to be no correlation between v_∞ and $\log L$, it appears to give a correlation with the spectral temperature $T_{2/3}$. Note that this correlation is not observed for T_*. With higher $T_{2/3}$, v_∞ increases. But the distribution of stars does not make a linear relation plausible. Most of the stars gather in the center of the plot, still spanning a range of 700 km s^{-1} in velocity. The stars with the fastest winds are much hotter, and the stars with slower winds show a gap of 500 km s^{-1} to the central bulge. If this clear separation is physical or just an effect of the sample size cannot be inferred with certainty. Still, a correlation appears reasonable. Furthermore, there are two stars comparably hot but with slow winds. A correlation becomes more obvious when we take the luminosity into account. Hotter stars require a lower luminosity to reach the same wind velocities. This indicates the dependency of the wind velocity field on the ionization structure, where high ions drive the wind better. In the upper right panel in Fig. 58, we can observe that there seems to be a clear line in the $Y - v_\infty$ plane beyond that no WC stars can be found. This might be an evolutionary effect, as the winds get faster in the later stages of evolution and the helium abundance decreases over time. Again we see a correlation with the luminosity, which this time is only a proxy for the stellar mass. Due to the way of estimating the stellar mass, those are interchangeable

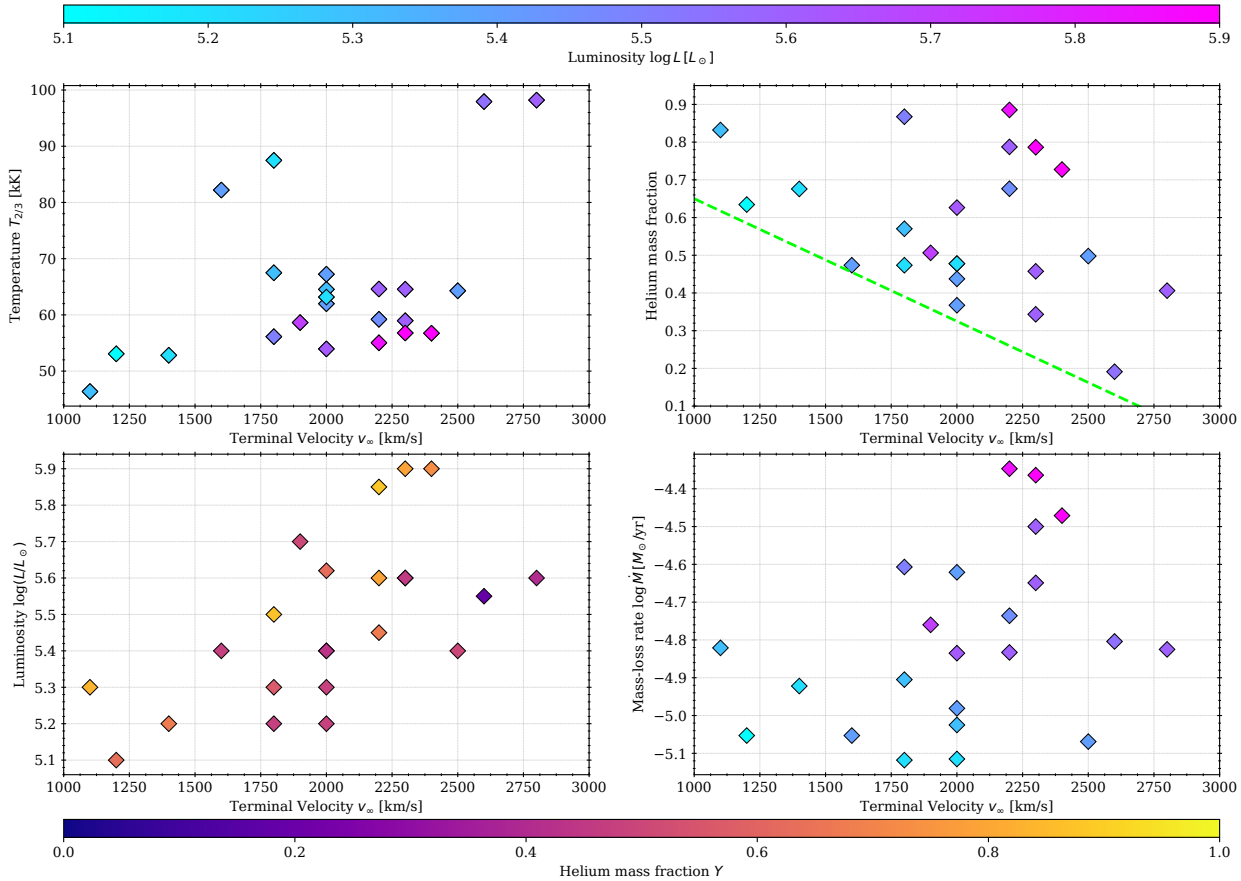

Figure 58: *Comparison of stellar parameters to the terminal wind velocity of the individual stars. The symbols mark the position of the sample stars. The color coding indicates the stellar luminosity for the upper left and right and the lower right panel, while it refers for the lower left panel to the helium mass fraction. The dashed green line in the upper right panel depicts a limit below no WR stars are found.*

here. Stars with higher initial masses enter the WC state (means high helium abundance and less carbon) with higher wind velocities. The line marking the threshold therefore might correspond to the mass limit for entering the WC phase. The lower right panel is in principle a different way of displaying the wind momentum-luminosity relation with the brightest stars in the upper right corner and the faintest in the lower left corner.

What else can be seen in our data? Figure 59 displays additional stellar parameter whose correlation is more or less obvious. In the upper right panel, we see that with increasing temperature, the helium abundance declines. This is just an evolutionary effect as the stars get hotter over time and helium fused to carbon and oxygen. The lower right panel shows that stellar feedback mechanism of ionization and mechanical energy transport are coupled, which is also expected. Hereby, The mechanical luminosity L_{mech} quantifies the kinetical energy transported in the wind, and is calculated as

$$L_{\mathrm{mech}} = E_{\mathrm{mech}}/\mathrm{yr} = \dot{M} \cdot v_{\infty}^{2}.$$

When we account for the helium abundance, the meaningfulness of the spectral types in terms of a correlation with the temperature reappears. We can observe in the upper right panel of Fig. 59 that stars with same spectral type and higher helium abundance are colder than their more enriched counterparts. This can also be seen in the upper left panel of Fig. 55. A similar correlation for the luminosity cannot be observed (cf. upper left panel in Fig. 59).

A surprising result is a correlation between the clumping factor D and the stellar temperature T_{*}. Hotter atmospheres are more clumped. Note that the derivation of the clumping factor leaves some ambiguities with the normalization and the derived correlation should be treated with caution.

As a final note, we want to state again that the sample contains only 23 stars. This fact makes all the found correlations and relations a subject of low number statistics. A more detailed analysis of a larger samples, such as the galactic WC stars, is required for verification.

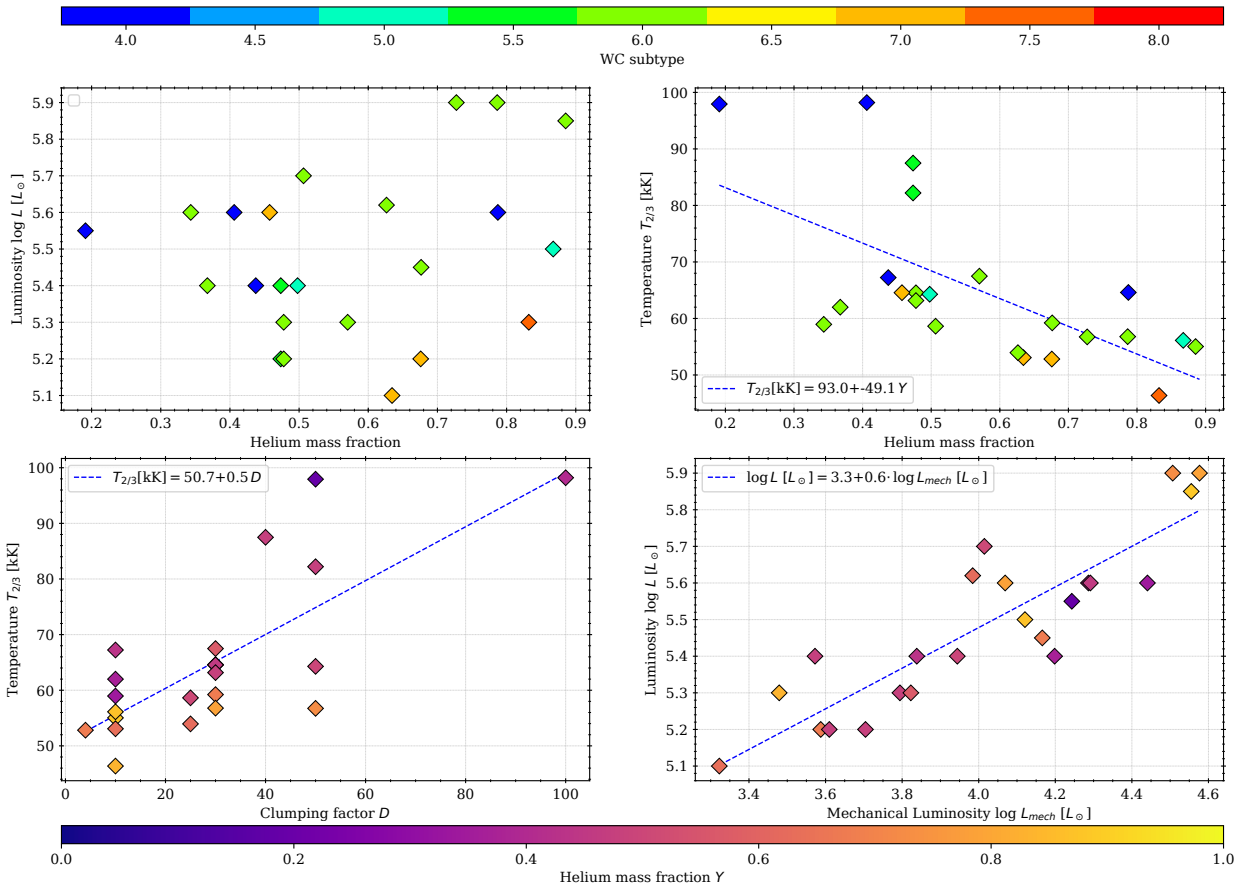

Figure 59: *Comparison of stellar parameter as indicated. The symbols mark the position of the sample stars. The color coding in the upper panels gives the spectral type, the color coding in the lower panel gives the helium mass fraction. The blue dashed lines correspond to a least square fit to the data with the equation given in the figure legends.*

10 Conclusions

»Ourselves, dismayed we stand, concerned in vain, the curtains drawn, all questions remain.«

– Bertold Brecht

This thesis provides the next step in our process to understand Wolf-Rayet stars. We analyzed a sample of WR stars in the Andromeda galaxy, exploiting the fact that the distances to those stars are much less uncertain than those for their Galactic counterparts. The focus was on the WR stars of the carbon sequence. In a first step, the spectra were investigated for spectral contamination by nearby sources. Indications used are the appearance of absorption lines in the spectrum and the dilution of the emission lines. From the original sample of 62 stars, 23 were found to be not significantly contaminated.

This reduced sample was then analyzed utilizing synthetic spectra calculated with the Potsdam Wolf-Rayet model atmosphere code. Starting from a model grid containing 166 models, more than 400 models were calculated to reproduce the observed spectra. The line systematics were analyzed in detail to overcome a spectral degeneracy that is present for stars with thick winds. This degeneracy could be partially overcome by focusing on the prominent emission lines. Eventually, reasonable fits were achieved for all 23 stars and the corresponding models provide us with the stellar parameter of our sample stars.

For each star, temperature, luminosity, the stellar wind parameters, and the abundances could be derived. Furthermore, we found that about half of the sample showed signs of fast rotation in their spectra. We also found 3 WC stars that show nitrogen features. A wide range of carbon abundances was determined throughout the sample. The remaining discrepancies between model and observation could be widely explained with shortcomings of the modeling process (two-component wind) and spectral contamination (by cool stars in the spectral range > 6500Å).

The derived parameter reveal a surprising picture. On the one hand, the clear correlation between the stellar parameters and their spectral type, which was found for Galactic WCs, could not be found here. On the other hand, we see that most stars in the M 31 sample occupy the same parameter regime as it was observed for Galactic WC stars. We can rule out the spectral degeneracy as the reason for this new finding.

We found a separation into two groups of stars when plotting them in an HRD. Most of the sample star have a similar temperature, ranging from 60 kK to 90 kK but a small subset of stars have temperatures around 180 kK. The cool temperatures might be a result of radius inflation in WR stars. This group occupies the same temperature range that was found before for WC stars. The extremely hot stars exhibit temperatures that were only found for WO stars so far.

Throughout the analysis and the discussion of the results, we have seen that the spectral classification system is not appropriate for a description of WC stars. We showed that an inclusion of the helium mass fraction for a two dimensional scheme, is required in the classification system to describe the nature of the classified star better.

Another interesting result was found when adopting a rotating wind. Signs of fast rotation were found for 9 stars. A detailed analysis for one of the sample stars revealed that a co-rotation radius of $4R_*$ reproduces the spectrum best. If this is also true for the other stars, non of the stars would rotate critically at their surface but very fast. Future investigations are encouraged into this. About half of the sample stars show signs of rotation while for galactic WR stars. This was only observed for a few stars.

A comparison to evolutionary models revealed the same discrepancies that were already discovered for galactic stars. It leaves a gap between what evolutionary models predict and spectral analysis find for WC stars. Future analysis based on better data and the here found results are encouraged. This involves a spectral fit of the stars found to have contaminated spectra with OB spectra in a superposition. Furthermore, the identified transition stars should also be investigated as potential binaries. The spectra do not indicate this, but an investigation with a WC+WN analysis might shed more light on these stars.

References

Abbott, D. C. 1977, PhD thesis, Colorado Univ., Boulder.
Abney, W. D. W. 1877, MNRAS, 37, 278
Armandroff, T. E. & Massey, P. 1985, ApJ, 291, 685
Arthur, S. J. 2007, Astrophysics and Space Science Proceedings, 1, 183
Asplund, M., Grevesse, N., Sauval, A. J., & Scott, P. 2009, ARA&A, 47, 481
Azimlu, M., Marciniak, R., & Barmby, P. 2011, AJ, 142, 139
Barniske, A. 2008, PhD thesis, University of Potsdam
Barniske, A., Hamann, W.-R., & Gräfener, G. 2006, in Astronomical Society of the Pacific Conference Series, Vol. 353, Stellar Evolution at Low Metallicity: Mass Loss, Explosions, Cosmology, ed. H. J. G. L. M. Lamers, N. Langer, T. Nugis, & K. Annuk, 243
Beals, C. S. 1940, JRASC, 34, 169
Berkhuijsen, E. M. 1984, A&A, 140, 431
Bertin, E. & Arnouts, S. 1996, A&AS, 117, 393
Bianchi, L., Efremova, B., Hodge, P., & Kang, Y. 2012, AJ, 144, 142
Block, D. L., Bournaud, F., Combes, F., et al. 2006, Nature, 443, 832
Bouvier, J. 2013, in EAS Publications Series, Vol. 62, EAS Publications Series, ed. P. Hennebelle & C. Charbonnel, 143–168
Bowen, I. S. 1928, ApJ, 67
Bransford, M. A., Thilker, D. A., Walterbos, R. A. M., & King, N. L. 1999, AJ, 118, 1635
Brott, I., de Mink, S. E., Cantiello, M., et al. 2011, A&A, 530, A115
Brown, W. R. 2015, ARA&A, 53, 15
Cantiello, M., Langer, N., Brott, I., et al. 2009, A&A, 499, 279
Cappellari, M., Emsellem, E., Krajnović, D., et al. 2011, MNRAS, 413, 813
Cardelli, J. A., Clayton, G. C., & Mathis, J. S. 1989, ApJ, 345, 245
Carignan, C., Chemin, L., Huchtmeier, W. K., & Lockman, F. J. 2006, ApJ, 641, L109
Cassinelli, J. P. 1979, ARA&A, 17, 275
Castor, J., McCray, R., & Weaver, R. 1975a, ApJ, 200, L107
Castor, J. I., Abbott, D. C., & Klein, R. I. 1975b, ApJ, 195, 157
Conn, A. R., Ibata, R. A., Lewis, G. F., et al. 2012, ApJ, 758, 11
Conti, P. S. & De Loore, C. W. H., eds. 1979, IAU Symposium, Vol. 83, Mass loss and evolution of O-type stars; Proceedings of the Symposium, Vancouver Island, British Columbia, Canada, June 5-9, 1978
Copeland, R. 1884, Contributions of Perkins Observatory, 3, 193
Courteau, S. & van den Bergh, S. 1999, AJ, 118, 337
Cowperthwaite, P. S., Berger, E., Villar, V. A., et al. 2017, ApJ, 848, L17
Crowther, P. A., De Marco, O., & Barlow, M. J. 1998, MNRAS, 296, 367
Crowther, P. A., Dessart, L., Hillier, D. J., Abbott, J. B., & Fullerton, A. W. 2002, A&A, 392, 653
Dalcanton, J. J., Williams, B. F., Lang, D., et al. 2012, ApJS, 200, 18
Ekström, S., Georgy, C., Eggenberger, P., et al. 2012, A&A, 537, A146
Eldridge, J. J. & Stanway, E. R. 2009, MNRAS, 400, 1019
Fabricant, D., Fata, R., Roll, J., et al. 2005, PASP, 117, 1411
Fierlinger, K. M., Burkert, A., Ntormousi, E., et al. 2016, MNRAS, 456, 710
Fitzpatrick, E. L. 1999, PASP, 111, 63
Fossati, L., Castro, N., Schöller, M., et al. 2015, A&A, 582, A45
Gayley, K. G. & Ignace, R. 2009, in American Institute of Physics Conference Series, Vol. 1171, American Institute of Physics Conference Series, ed. I. Hubeny, J. M. Stone, K. MacGregor, & K. Werner, 187–198
Gebbie, K. B. & Thomas, R. N., eds. 1968, Wolf-rayet stars
Gil de Paz, A., Boissier, S., Madore, B. F., et al. 2007, ApJS, 173, 185
Gräfener, G. & Hamann, W.-R. 2005, A&A, 432, 633
Grafener, G., Hamann, W.-R., Hillier, D. J., & Koesterke, L. 1998, A&A, 329, 190
Gräfener, G., Koesterke, L., & Hamann, W.-R. 2002, A&A, 387, 244
Gräfener, G., Owocki, S. P., & Vink, J. S. 2012, A&A, 538, A40
Grassitelli, L., Langer, N., Grin, N. J., et al. 2018, A&A, 614, A86
Guhathakurta, P., Choi, P. I., & Reitzel, D. B. 2000, in Bulletin of the American Astronomical Society, Vol. 32, American Astronomical Society Meeting Abstracts, 1451
Hamann, W.-R. 1985, A&A, 148, 364
Hamann, W.-R. 1986, A&A, 160, 347
Hamann, W.-R. 1987, Line Formation in Expanding Atmospheres: Multi-Level Calculations using Approximate Lambda Operators, ed. W. Kalkofen, 35
Hamann, W.-R., Duennebeil, G., Koesterke, L., Wessolowski, U., & Schmutz, W. 1991, A&A, 249, 443
Hamann, W.-R. & Gräfener, G. 2003, A&A, 410, 993
Hamann, W.-R. & Gräfener, G. 2004, A&A, 427, 697
Hamann, W.-R., Gräfener, G., & Koesterke, L. 2003, in IAU Symposium, Vol. 212, A Massive Star Odyssey: From Main Sequence to Supernova, ed. K. van der Hucht, A. Herrero, & C. Esteban, 198
Hamann, W.-R., Gräfener, G., & Liermann, A. 2006, A&A, 457, 1015
Hamann, W.-R. & Koesterke, L. 1998, A&A, 335, 1003
Hamann, W.-R. & Schmutz, W. 1987, A&A, 174, 173
Hamann, W.-R., Wessolowski, U., & Koesterke, L. 1994, A&A, 281, 184
Hillier, D. J. 1987, ApJS, 63, 965
Hillier, D. J. 1988, ApJ, 327, 822
Hillier, D. J. 1989, ApJ, 347, 392
Hillier, D. J. 1990, A&A, 231, 116
Kent, S. M. 1989, AJ, 97, 1614
Khan, R. 2017, VizieR Online Data Catalog, 222
Khokhlov, A., Mueller, E., & Hoeflich, P. 1993, A&A, 270, 223
Koesterke, L. & Hamann, W.-R. 1995, A&A, 299, 503
Koesterke, L., Hamann, W.-R., & Gräfener, G. 2002, A&A, 384, 562
Krumholz, M. R. & Matzner, C. D. 2009, ApJ, 703, 1352
Kudritzki, R.-P. & Puls, J. 2000, ARA&A, 38, 613
Langer, N. 1989, A&A, 210, 93
Loeb, A. & Narayan, R. 2008, MNRAS, 386, 2221
Madau, P. & Dickinson, M. 2014, ARA&A, 52, 415
Maeder, A. 1992, A&A, 264, 105
Maeder, A. 1996, in Liege International Astrophysical Colloquia, Vol. 33, Liege International Astrophysical Colloquia, ed. J. M. Vreux, A. Detal, D. Fraipont-Caro, E. Gosset, & G. Rauw, 39
Maeder, A. 1999, A&A, 347, 185
Magnier, E. A., Prins, S., van Paradijs, J., et al. 1995, Astronomy and Astrophysics Supplement Series, 114, 215
Massey, P. & Johnson, O. 1998, ApJ, 505, 793
Massey, P., Olsen, K. A. G., Hodge, P. W., et al. 2006, AJ, 131, 2478
McConnachie, A. W., Irwin, M. J., Ferguson, A. M. N., et al. 2005, MNRAS, 356, 979
Meyssonnier, N., Lequeux, J., & Azzopardi, M. 1993, Astronomy and Astrophysics Supplement Series, 102, 251
Mihalas, D., Kunasz, P. B., & Hummer, D. G. 1975, ApJ, 202, 465
Mihalas, D., Kunasz, P. B., & Hummer, D. G. 1976, ApJ, 210, 419
Mink, D. J., Wyatt, W. F., Caldwell, N., et al. 2007, in Astronomical Society of the Pacific Conference Series, Vol. 376, Astronomical Data Analysis Software and Systems XVI, ed. R. A. Shaw, F. Hill, & D. J. Bell, 249
Morrison, H., Caldwell, N., Harding, P., et al. 2008, Astro-

physics and Space Science Proceedings, 5, 227
Nandy, K., Thompson, G. I., Jamar, C., Monfils, A., & Wilson, R. 1975, A&A, 44, 195
Neugent, K. F. & Massey, P. 2011, ApJ, 733, 123
Neugent, K. F., Massey, P., & Georgy, C. 2012, ApJ, 759, 11
Nomoto, K., Kobayashi, C., & Tominaga, N. 2013, ARA&A, 51, 457
Nugis, T. & Lamers, H. J. G. L. M. 2000, A&A, 360, 227
Olson, G. L., Auer, L. H., & Buchler, J. R. 1986, J. Quant. Spec. Radiat. Transf., 35, 431
Olson, G. L. & Kunasz, P. B. 1987, J. Quant. Spec. Radiat. Transf., 38, 325
Oskinova, L. M., Hamann, W.-R., & Feldmeier, A. 2007, A&A, 476, 1331
Owocki, S. P., Gayley, K. G., & Shaviv, N. J. 2004, ApJ, 616, 525
Paczyński, B. 1966, Acta Astron., 16, 231
Parker, E. N. 1958, ApJ, 128, 664
Partridge, C., Lahav, O., & Hoffman, Y. 2013, MNRAS, 436, L45
Peters, T., Banerjee, R., Klessen, R. S., et al. 2010, ApJ, 711, 1017
Peterson, D. M., Hummel, C. A., Pauls, T. A., et al. 2006, Nature, 440, 896
Pickering, E. C. 1881, Nature, 23, 604
Portegies Zwart, S. F., McMillan, S. L. W., & Gieles, M. 2010, ARA&A, 48, 431
Porter, J. M. & Rivinius, T. 2003, PASP, 115, 1153
Puls, J. & Herrero, A. 1988, A&A, 204, 219
Ramachandran, V., Hamann, W.-R., Hainich, R., et al. 2018, A&A, 615, A40
Riess, A. G., Fliri, J., & Valls-Gabaud, D. 2012, ApJ, 745, 156
Riess, A. G., Macri, L. M., Hoffmann, S. L., et al. 2016, ApJ, 826, 56
Rivinius, T., Carciofi, A. C., & Martayan, C. 2013, A&A Rev., 21, 69
Rybicki, G. B. 1972, in Line Formation in the Presence of Magnetic Fields, 145
Sander, A., Hamann, W.-R., & Todt, H. 2012, A&A, 540, A144
Sander, A., Shenar, T., Hainich, R., et al. 2015, A&A, 577, A13
Sander, A. A. C., Hamann, W.-R., Todt, H., Hainich, R., & Shenar, T. 2017, A&A, 603, A86
Sanders, N. E., Caldwell, N., McDowell, J., & Harding, P. 2012, ApJ, 758, 133
Scharmer, G. B. 1981, ApJ, 249, 720
Scharmer, G. B. 1984, Accurate solutions to non-LTE problems using approximate lambda operators, ed. W. Kalkofen, 173–210
Schmidt, M. 1957, Bull. Astron. Inst. Netherlands, 14, 17
Schmutz, W., Hamann, W.-R., & Wessolowski, U. 1989, A&A, 210, 236
Seaton, M. J. 1979, MNRAS, 187, 73P
Shaviv, N. J. 2000, ApJ, 532, L137
Shenar, T. 2013, Master's thesis, University of Potsdam
Shenar, T., Hainich, R., Todt, H., et al. 2016, A&A, 591, A22
Shenar, T., Hamann, W.-R., & Todt, H. 2014, A&A, 562, A118
Shenar, T., Oskinova, L., Hamann, W.-R., et al. 2015, ApJ, 809, 135
Skrutskie, M. F., Cutri, R. M., Stiening, R., et al. 2006, AJ, 131, 1163
Smith, L. F. 1968, MNRAS, 138, 109
Spitzer, L. 1978, Physical processes in the interstellar medium
Stetson, P. B. 1987, PASP, 99, 191
Torrejón, J. M., Schulz, N. S., Nowak, M. A., et al. 2015, ApJ, 810, 102
Tremaine, S. 1995, AJ, 110, 628
Tully, R. B., Courtois, H. M., Dolphin, A. E., et al. 2013, AJ, 146, 86
Tully, R. B. & Fisher, J. R. 1988, Catalog of Nearby Galaxies
Tully, R. B., Shaya, E. J., Karachentsev, I. D., et al. 2008, ApJ, 676, 184
ud-Doula, A. & Owocki, S. P. 2002, ApJ, 576, 413
Underhill, A. B. 1973, in IAU Symposium, Vol. 49, Wolf-Rayet and High-Temperature Stars, ed. M. K. V. Bappu & J. Sahade, 237
Unwin, S. C. 1983, MNRAS, 205, 773
van den Bergh, S. 1964, ApJS, 9, 65
van der Hucht, K. A. 2001, New A Rev., 45, 135
von Zeipel, H. 1924, MNRAS, 84, 665
Wagner-Kaiser, R., Sarajedini, A., Dalcanton, J. J., Williams, B. F., & Dolphin, A. 2015, MNRAS, 451, 724
Williams, S. C., Darnley, M. J., Bode, M. F., Keen, A., & Shafter, A. W. 2014, ApJS, 213, 10
Wolf, C. J. E. & Rayet, G. 1867, Academie des Sciences Paris Comptes Rendus, 65, 292
Zanstra, H. 1931, ZAp, 2, 1
Zaritsky, D., Kennicutt, Jr., R. C., & Huchra, J. P. 1994, ApJ, 420, 87